

Forced and Self Oscillations of Hydraulic Systems Induced by Cavitation Vortex Rope of Francis Turbines

THÈSE N° 5117 (2011)

PRÉSENTÉE LE 9 SEPTEMBRE 2011

À LA FACULTÉ SCIENCES ET TECHNIQUES DE L'INGÉNIEUR
LABORATOIRE DE MACHINES HYDRAULIQUES
PROGRAMME DOCTORAL EN ENERGIE

ÉCOLE POLYTECHNIQUE FÉDÉRALE DE LAUSANNE

POUR L'OBTENTION DU GRADE DE DOCTEUR ÈS SCIENCES

PAR

Sébastien ALLIGNÉ

acceptée sur proposition du jury:

Prof. C. Ancey, président du jury
Prof. F. Avellan, directeur de thèse
Dr M. Couston, rapporteur
Prof. F. Gallaire, rapporteur
Prof. Y. Tsujimoto, rapporteur



ÉCOLE POLYTECHNIQUE
FÉDÉRALE DE LAUSANNE

Suisse
2011

*Learn from yesterday,
live for today,
hope for tomorrow.
The important thing is not to stop questioning.*

Albert Einstein

Remerciements

En préambule de ce document, il m'importe d'exprimer ma gratitude à toutes celles et ceux qui ont contribué à la réalisation de cette thèse.

J'exprime mes sincères remerciements à mon directeur de thèse, le Professeur François Avellan, pour m'avoir accordé sa confiance tout au long de ce travail. Malgré mon parcours professionnel atypique qui s'était éloigné du monde de l'hydraulique, il m'a donné l'opportunité de commencer ce travail de doctorat. Je le remercie d'avoir dirigé ma recherche dans les moments clés, de m'avoir toujours pousser à suivre la ligne directrice et d'exiger le meilleur de moi-même. Je le remercie également pour m'avoir donné la chance de présenter ma recherche lors de différents congrès à travers le monde.

Ce travail de recherche n'aurait pas été possible sans l'appui financier de l'agence de la Confédération pour la promotion de l'innovation et de l'entreprise Alstom Hydro. Je remercie spécialement Michel Couston, Jean Louis Deniau, Hélène Marin, et Farid Mazzouji pour leur intérêt et leurs encouragements. Sans oublier Pierre Lerroy en charge de promouvoir SIMSEN au sein d'Alstom avec qui, il me tarde de faire une session de snowkite sur Grenoble.

Mes remerciements vont également aux membres du jury, Professeur Christophe Ancey, Président du jury, Dr. Michel Couston de Alstom Hydro, Professeur François Gallaire de l'EPFL et Professeur Yoshinobu Tsujimoto de l'Université d'Osaka, pour le temps consacré à la lecture de ce manuscrit ainsi que pour toutes les remarques et discussions constructives lors de la défense de thèse privée.

Je souhaite également remercier les différents responsables du Laboratoire, Pierre Maruzewski pour son aide aux lancements et aux post-traitements des calculs MICA, Cécile Münch pour m'avoir résolu nombreux problèmes me permettant de réaliser des simulations numériques de haute qualité, Mohamed Farhat pour m'avoir confié la caméra rapide avec laquelle de jolies visualisations de la torche forte charge ont été faites.

Je souhaite bien sûr remercier l'équipe Hydro-acoustique, en commençant par mon mentor Christophe Nicolet qui a su me transmettre tout son savoir sur le sujet dès mon arrivée mais qui m'a également suivi de près après son départ du Laboratoire. Au delà du monde professionnel, il est bien plus encore. C'est aussi un ami et le parrain de ma fille Anaëlle. L'avenir nous réserve encore de belles aventures. Je remercie également Nicolas Ruchonnet mon homologue windsurfer avec qui nous avons eu de nombreuses discussions scientifiques m'ayant permis de formaliser de nombreux points essentiels à la réalisation de cette thèse. Mais également de nombreuses discussions pour le motiver à rejoindre le groupe des kitesurfers. Un jour peut être... Je souhaite le succès à la relève, Andres Müller l'expérimentateur et Christian Landry le numéricien, qui ont la lourde tâche d'expliquer plus profondément le phénomène d'instabilité forte charge. Finalement rien n'aurait été possible sans l'implémentation des nouveaux modèles dans SIMSEN faite par Philippe

Allenbach. Merci pour son enthousiasme dans le projet. Sans oublier Basile Kawkabani qui a pris le temps de m'éclaircir les idées sur le fonctionnement des machines électriques.

Je remercie le groupe du bureau d'étude mené par Philippe Cerrutti qui a également de nombreuses autres fonctions comme la maintenance du système informatique que j'ai fortement sollicitée. Merci à Philippe Faucherre pour les nombreux dessins techniques qu'il m'a fourni. Merci à Alain Renaud de nous avoir aidé pour le contrôle dimensionnel des aubes de Kaplan. Quant à Vincent, merci pour cette leçon de pilotage au karting.

Merci pour la bonne ambiance dégagée par le groupe des mécaniciens mené par Louis avec qui j'ai apprécié nos discussions autour d'un verre lors des pots de thèse. Au sein de l'équipe, je commencerai par Maxime, qui doit absolument améliorer son revers au ping pong. Puis Victor avec qui l'entente au volley ball fut surprenante. Et enfin Jean Daniel et Mattias, mes bêtes noires que je rêve un jour de battre au bras de fer... Y a du boulot!

Je remercie Isabelle pour son efficacité dans les travaux administratifs. Merci à Shadije, d'avoir élu mon bureau comme étant le plus mal rangé du Laboratoire.

Je remercie également mes collègues et amis doctorants avec qui les "jeudredis" resteront d'excellent moments. Ce fut périlleux de concilier la vie étudiante avec la vie de famille notamment le vendredi matin à la crèche. Cette thèse m'a permis de rencontrer des petits suisses remarquables, je pense en premier à El Paquito et Martino avec qui j'ai pu partager, entre autres, des sessions de kitesurf mémorables dans le sud de la France et au Maroc. Je félicite Steven pour la rose et l'organisation du week end au lac de Joux. Merci à Matthieu et Andres le clan 1005 qui m'a fait découvrir Balélec dans toute sa grandeur. Je ne veux pas oublier les autres personnes avec qui j'ai eu le plaisir de travailler. Je pense à Vlad et Ali qui m'ont initié aux moyens informatiques pour lancer diverses simulations et qui m'ont résolu de nombreux problèmes techniques. Mes remerciements se tournent ensuite vers le groupe experimental. Philippe pour ses anecdotes croustillantes et sa bonne humeur, Marc pour son calme qui m'a toujours impressionné, Amir qui m'a fait découvrir l'hospitalité et la gentillesse de la culture iranienne tout comme son frère Ali, Francesco avec qui les cours d'espagnols improvisés furent d'une efficacité redoutable. Merci au clan germanique, Stephan pour les discussions agitées et Olivier pour son initiation de Forró. Je terminerai par l'équipe SPH, Ebrahim, qui a du supporter mes humeurs du jour parfois expressives juste en face de lui et Christian qui m'a fait connaître les douceurs de la Broye.

Je remercie du fond du coeur ma femme Cécile pour son soutien et son amour dont elle fait preuve chaque jour. Une thèse est avant tout une aventure psychologique qu'elle a su comprendre et partager. Merci à mes enfants, Candice et Anaëlle, pour leur énergie et leur amour qui m'ont fait oublier les petits tracassés quotidiens d'une thèse.

Je souhaite également remercier mon beau-père Jean Pierre pour son enthousiasme dans cette aventure et ses conseils scientifiques avisés dont le recul m'impressionne. Merci à ma belle-mère Hélène qui est venu à notre secours lorsque les enfants étaient malades, ce qui a contribué à l'avancement continu de cette thèse surtout en période hivernale.

Enfin, je finirai par mes parents que je remercie pour l'éducation qu'ils m'ont apportée tout au long de ces années. Cela m'a permis de trouver ma voie à la fois sur le plan personnel et professionnel.



Sébastien Alligné

Résumé

Avec des stratégies de marché énergétique basées sur une tarification instantannée de l'électricité en fonction de la demande ou des prévisions, les exploitants font de plus en plus fonctionner leurs installations hydroélectriques à des points de fonctionnement off-design pour couvrir les variations de production d'électricité. Dans ces conditions, les turbines Francis développent un écoulement tournant cavitant en sortie de roue qui induit des fluctuations de pression se propageant au sein du système hydraulique. Le coeur de ce tourbillon cavitant est communément appelé torche. A la résonance, la superposition de ces ondes de propagation donne naissance à une onde stationnaire conduisant à de larges fluctuations de pression et de puissance machine. Le but de ce travail est de simuler cette résonance qui peut intervenir à la fois à charge partielle ou à forte charge.

L'identification des sources d'excitation induites par la torche cavitante est réalisée à partir de simulations numériques basées sur un modèle incompressible tridimensionnel, appelé modèle hydrodynamique (HD). L'hypothèse d'une propagation d'ondes planes dans les conduites est posée car de très basses fréquences sont concernées lors de ces résonances. Ainsi, la propagation de ces sources est simulée avec un modèle compressible monodimensionnel, appelé modèle hydroacoustique (HA). Le modèle HA couvre tout le système hydraulique y compris la région de la source d'excitation correspondant au diffuseur de la turbine Francis, alors que le modèle HD couvre seulement la région de la source. Dans ce travail, un modèle HA du diffuseur a été développé. Une source de quantité de mouvement, modélisant l'action des forces de l'écoulement sur les parois du diffuseur est considérée. De plus, le volume de cavitation fluctuant est considéré comme une source de masse. Enfin, un amortissement est introduit pour représenter la dissipation d'énergie lors d'un changement de phase entre le liquide et le gaz.

Les investigations menées à charge partielle ont pour but de simuler la résonance à haute charge partielle pour laquelle la fréquence caractéristique des fluctuations de pression est observée entre 2 et 4 fois la fréquence de rotation de la roue. Des mesures de ce phénomène ont été faites dans le cadre du projet FLINDT qui a été choisi comme cas test de validation. Tout d'abord, les paramètres du modèle HA du diffuseur ont été déterminés à partir de simulations instationnaires monophasiques et diphasiques. Une analyse de ces paramètres est réalisée et une comparaison entre les résultats monophasiques et diphasiques est effectuée. Il est montré qu'une modélisation de la cavitation est nécessaire pour retrouver la fréquence de précession de la torche qui dépend de la quantité de gaz au coeur du vortex. Cependant, le volume de vapeur est sous estimé et un facteur de correction sur le nombre de Thoma est nécessaire pour une concordance entre l'expérience et les résultats de simulations. De plus, il a été montré que l'écoulement tridimensionnel dans le coude du diffuseur donne naissance aux sources HA capables d'exciter le système hydraulique. L'intensité des sources est supérieure lorsque des simu-

lations diphasiques sont considérées. Avant de simuler le phénomène de résonance à haute charge partielle, une validation préliminaire de ces paramètres HA est faite en simulant une résonance à charge partielle où la fréquence de précession de la torche, autour de 0.3 fois la fréquence de rotation de la roue, coïncide avec la première fréquence propre du système hydraulique. Lorsque les conditions de résonance ne sont pas remplies, le maximum d'amplitude des fluctuations de pression est atteint dans le cône du diffuseur autour de 1% de la chute. Cependant, quand la résonance apparaît, le maximum des fluctuations de pression peut atteindre 7% de la chute. Une bonne concordance est obtenue avec les ordres de grandeur trouvés dans des mesures disponibles dans la littérature. Suite à cette validation préliminaire, la simulation du phénomène de résonance à haute charge partielle a été traitée. Il a été trouvé que le mécanisme induisant ce phénomène est lié à une fluctuation du volume de cavitation à une fréquence qui peut coïncider avec une fréquence propre du système hydraulique. Cependant cette fluctuation a été trouvée pour un nombre de Thoma beaucoup plus grand que celui expérimental conduisant à un volume de cavitation faible par rapport à l'expérience.

Une installation prototype de 4 turbines Francis de 478 MW située en Colombie Britannique au Canada a été choisie comme étant le cas d'étude pour analyser le phénomène d'instabilité à forte charge. En effet, cette instabilité est apparue à la fois sur prototype et modèle réduit. Ainsi, des mesures ont été faites sur modèle réduit dans le but d'utiliser les données expérimentales pour valider les simulations numériques réalisées avec le modèle HA du diffuseur. La source de masse définie dans ce modèle est décrite par un paramètre décisif qui est le facteur d'application de débit. Largement utilisé lors de précédents travaux pour l'analyse du phénomène, ce paramètre est défini pour représenter l'effet des fluctuations HA du débit aval au volume de cavitation sur la source de masse. Dans ce travail, la même formulation est utilisée et a été combinée avec l'introduction d'un nouveau paramètre: l'amortissement thermodynamique. Tout d'abord, ces paramètres HA ont été déterminés pour les différents points d'opération expérimentaux à partir de simulations stationnaires monophasiques. Puis, en utilisant ces paramètres, une analyse de stabilité aux petites perturbations dans le domaine fréquentiel a été faite pour identifier la stabilité des différents points de fonctionnement. Les fréquences caractéristiques des instabilités mesurées expérimentalement ont été trouvées à l'aide de cette analyse modale. Cependant, cette analyse dans le domaine fréquentiel ne donne aucune information sur l'amplitude des fluctuations de pression induites par l'instabilité. Ainsi des simulations HA dans le domaine temporel ont été réalisées. Il a été montré que l'utilisation de paramètres constants dans le modèle HA du diffuseur conduit à des simulations temporelles divergentes alors que des paramètres non linéaires conduisent à un cycle limite dont les fluctuations ont des amplitudes finies. De plus, la non linéarité de l'amortissement thermodynamique en fonction de la pression, est décisif pour atteindre ce cycle limite. Enfin, une méthodologie a été mise en place pour prédire l'instabilité sur prototype à partir d'investigations sur modèle réduit. Une combinaison de mesures expérimentales, de simulations numériques et de calcul des modes propres de l'installation sur laquelle est montée le modèle réduit, permet la calibration précise des paramètres du modèle HA du diffuseur à l'échelle modèle. Enfin, une transposition de ces paramètres vers le prototype par rapport à des lois de similitudes est appliquée pour l'analyse de stabilité de la centrale.

Mots-clés: Turbine Francis, Torche, Charge partielle, Résonance, Forte charge, Instabilité, Cavitation, Simulation numérique des fluides, Ecoulements transitoires.

Abstract

With economical energy market strategies based on instantaneous pricings of electricity as function of the demand or the predictions, operators harness more hydroelectric facilities to off-design operating points to cover the variations of the electricity production. Under these operating conditions, Francis turbines develop a cavitating swirling flow at the runner outlet which induces pressure fluctuations propagating in the whole hydraulic system. The core of this cavitating vortex is usually called vortex rope. At resonance conditions, the superimposition of the induced traveling waves gives rise to a standing wave leading to undesirable large pressure and output power fluctuations. The aim of this present work is to predict and to simulate this resonance phenomenon which may happen both in part load or full load operating conditions.

The identification of the excitation sources induced by the cavitating vortex rope is performed with numerical simulations based on a three dimensional incompressible model, so called hydrodynamic (HD) model. The assumption of plane wave propagation in the water passages connected to the turbine is set since low surging frequencies are involved. Hence, propagation of these sources is simulated with a one dimensional compressible model, so called hydroacoustic (HA) model. The HA model covers the entire hydraulic system including the source region corresponding to the draft tube of the Francis turbine whereas the HD model covers only the source region. In this present work, a specific HA draft tube model has been developed. A momentum source modeling the forces induced by the flow acting on the draft tube wall is considered. Moreover, the fluctuating cavitation volume is considered as a mass source. Finally, a thermodynamic damping is introduced to model energy dissipation during a phase change between liquid and gas.

Investigations at part load conditions aim to simulate the upper part load resonance phenomenon for which frequency of pressure fluctuations are experienced between 2 and 4 times the runner frequency. Measurements were carried out in the framework of the FLINDT project which is therefore the case study for validation. First of all, HA draft tube model parameters have been derived for the investigated operating point considering both single phase and two phase unsteady simulations with the HD model. An analysis of these parameters is performed and comparison between single phase and two phase simulation results is made. It is shown that the cavitation modeling in the HD model is necessary to find the vortex rope precession frequency which depends on the cavitation amount in the vortex core. However, the volume of vapor is underestimated and a correction factor on the Thoma number is necessary to get a good agreement between experiments and simulation results. Moreover it has been shown that the three dimensional flow in the elbow gives rise to HA sources able to excite the hydraulic system. Intensity of the sources are higher when two phase flow simulations are considered. Before simulating the upper part load resonance phenomenon, a preliminary validation of these

HA parameters is performed by simulating a standard part load resonance where the vortex rope precession frequency, near 0.3 times the runner frequency, matches with the first eigenfrequency of the hydraulic system. In out of resonance conditions, maximum of pressure fluctuations amplitudes are experienced in the draft tube cone with an amplitude being 1% of the turbine head. However, when resonance occurs, maximum amplitude of pressure fluctuations reaches up to 7%. A good agreement is obtained with the order of magnitudes found in measurements available in the literature. After this preliminary validation, simulation of the upper part load resonance phenomenon has been tackled. It has been found that the mechanism inducing this phenomenon is related to an undesirable fluctuation of the cavitation volume which frequency can match with an eigenfrequency of the hydraulic system. However, this fluctuation is captured for a Thoma number much higher than the experimental one leading to a cavitation volume very small compared to the experiments.

A prototype installation of four 478 MW Francis turbines located in the Canada's province British Columbia, has been chosen as the case study to analyze the full load instability phenomenon. Indeed, this instability occurred on prototype and reduced scale model as well. Hence, experimental measurements have been carried out on the reduced scale model aiming to use experimental data to validate the numerical simulations performed with the HA draft tube model. The mass source defined in this model, is described by a decisive parameter which is the mass flow gain factor. Extensively used in previous works for the analysis of this phenomenon, this parameter is defined to represent the effect of the HA fluctuations of the downstream flow rate to the cavitation volume on the mass source. In this present work, the same formulation is used and has been combined with the introduction of a new parameter: the thermodynamic damping. First of all, these HA parameters have been derived for the different investigated experimental operating points from single phase steady simulations. Then, using these computed parameters, a small perturbation stability analysis in the frequency domain has been carried out to identify the stability of the different operating points. The experimental unstable characteristic frequencies have been found out with this modal analysis. However, this analysis in the frequency domain does not give any information about the amplitude of the pressure fluctuations induced by the instability. Hence, time domain HA simulations have been performed. It has been shown that the using of constant HA draft tube model parameters leads to divergent time domain simulations, whereas nonlinear parameters depending on the pressure variable, lead to a limit cycle of finite amplitude fluctuations. Moreover, nonlinearity of the thermodynamic damping is decisive to reach this limit cycle. Finally, a methodology has been set up to predict the instability of the prototype from the investigations on the reduced scale model. A combination of measurements, numerical simulations and computation of the eigenmodes of the reduced scale model installed on test rig, allows the accurate calibration of the HA draft tube model parameters at the model scale. Finally, transposition of these parameters to the prototype according to similitude laws is applied for the stability analysis of the power plant.

Keywords: Francis turbine, Vortex rope, Part load, Resonance, Full load, Instability, Cavitation, Computational fluid dynamics, Fluid transients.

Contents

I	Introduction	1
1	Hydropower	3
2	Francis Turbines	5
2.1	Reaction Type Turbine	5
2.2	Operating Point Parameters	6
2.3	The Thoma Number	7
2.4	The Froude Number	8
3	Vortex Rope in Francis Turbines	9
3.1	Velocity Triangles	9
3.2	Vortex Rope Interaction with Hydraulic Systems	9
4	State of the Art	11
4.1	Part Load Resonance	11
4.2	Upper Part Load Resonance	14
4.3	Full Load Instability	15
5	Objectives and Computing Methodologies	17
6	Document Organization	19
II	Computational Tools and Models	21
7	One Dimensional Hydroacoustic (HA) Model	23
7.1	Francis Turbine Runner Model	23
7.2	Viscoelastic Pipe Model	24
7.3	Draft Tube Model	25
7.3.1	Mass Source	26
7.3.2	Momentum Source	27
7.3.3	Modeling of Hydroacoustic Feedback on Sources	29
7.3.4	Thermodynamic Damping	30
7.3.5	Draft tube model adapted for Part Load Conditions	34
7.3.6	Draft tube model adapted for Full Load Conditions	35
7.3.7	Synthesis	36

8	Three Dimensional Hydrodynamic (HD) Model	39
8.1	Governing Equations	39
8.1.1	Single Phase Flow Simulation (SPS)	39
8.1.2	Two Phase Flow Simulation (TPS)	39
8.2	Reynolds Averaged Navier Stokes Equations	41
8.3	Turbulent Modeling	42
8.4	Space and Time Discretization	43
9	Data Flow	45
9.1	Part Load Operating Conditions	45
9.1.1	One Way Simulation	45
9.1.2	Two Way Simulation	47
9.2	Full Load Operating Conditions	47
10	Small Perturbation Stability Analysis Tool	49
10.1	Set of Differential Equations	49
10.2	Eigenmodes and Stability Assessment	49
10.2.1	Linearization Procedure	49
10.2.2	Eigenmodes Computation	51
10.2.3	Stability Assessment	51
10.3	Lumped and Distributed Draft Tube Models	52
III	Part Load Operating Conditions	55
11	Case Study	57
11.1	FLINDT project	57
11.2	Phenomenon of Interest	57
11.3	Objectives	61
12	Numerical Investigations	63
12.1	The 3D HD model	63
12.1.1	Setup	63
12.1.2	Simulation Results	65
12.2	Identification of HA Draft Tube Model Parameters	68
12.2.1	Momentum Source	68
12.2.2	Mass Source	75
12.2.3	Cavitation Compliance	77
12.2.4	Thermodynamic Damping	80
12.2.5	Influence of the Elbow on the HA Parameters	82
12.3	Validation of HA Draft Tube Model Parameters	84
12.3.1	Hydraulic System Description	84
12.3.2	One Way Simulation of a Part Load Resonance	86
12.3.3	Modeling of Nonlinear Hydroacoustic Feedback	88
12.4	Upper Part Load Resonance Simulation	91
12.4.1	Identification of Cavitation Volume Fluctuation	91
12.4.2	Hydroacoustic One Way Simulation	94

12.5 Two Way Simulation of a Part Load Resonance	98
12.5.1 Hydraulic System Description	98
12.5.2 Data Flow and Time Integration	99
12.5.3 Results	100
IV Full Load Operating Conditions	103
13 Case Study	105
13.1 MICA Hydroelectric Powerplant	105
13.2 Phenomenon of Interest	106
13.3 Objectives	106
14 Experimental Investigations	107
14.1 EPFL Experimental Validation Facilities	107
14.2 Measurements	108
15 Numerical Investigations	113
15.1 The 3D HD model	113
15.1.1 Setup	113
15.1.2 Simulation Results	114
15.2 Identification of HA Draft Tube Model Parameters	115
15.2.1 Mass Flow Gain Factor	115
15.2.2 Cavitation Compliance	116
15.2.3 Thermodynamic Damping	117
15.3 Validation of HA Draft Tube Model Parameters	118
15.4 Full Load Instability Simulation	119
15.4.1 Calibration of the Thermodynamic Damping	120
15.4.2 Nonlinear Time Domain Simulation	122
15.4.3 Energy Balance	124
15.5 Prediction of Prototype Instability	127
15.5.1 Calibration of HA parameters	128
15.5.2 Transposition to the Prototype	129
15.5.3 Prediction	131
V Conclusions and Perspectives	135
16 Conclusions	137
17 Perspectives	141
References	145
Curriculum Vitae	154

Notations

Latin

a	Wave speed	$[\text{m}\cdot\text{s}^{-1}]$
e	Pipe thickness	$[\text{m}]$
f	Frequency	$[\text{Hz}]$
g	Gravitational acceleration	$[\text{m}\cdot\text{s}^{-2}]$
h	Piezometric head	$[\text{m}]$
m	Mass	$[\text{kg}]$
n	Runner rotational frequency	$[\text{Hz}]$
p	Static pressure	$[\text{Pa}]$
p_v	Saturation vapor pressure	$[\text{Pa}]$
s	Complex eigenvalue	$[-]$
t	Time	$[\text{s}]$
w	Angular velocity	$[\text{rad}\cdot\text{s}^{-1}]$
A	Pipe cross section	$[\text{m}^2]$
C	Compliance	$[\text{m}^2]$
C	Absolute flow velocity	$[\text{m}\cdot\text{s}^{-1}]$
C_{xy}	Coherence function between signals x and y	$[-]$
D	Pipe diameter	$[\text{m}]$
E	Specific turbine energy	$[\text{J}\cdot\text{kg}^{-1}]$
E	Young modulus	$[\text{Pa}]$
F	Force	$[\text{N}]$
H	Turbine head	$[\text{m}]$
J_t	Turbine inertia	$[\text{kg}\cdot\text{m}^2]$
L	Hydraulic inductance	$[\text{s}^2\cdot\text{m}^{-2}]$
L	Length	$[\text{m}]$
N	Number of runner revolution per minute	$[\text{min}^{-1}]$
Q	Flow rate	$[\text{m}^3\cdot\text{s}^{-1}]$
R	Hydraulic resistance	$[\text{s}\cdot\text{m}^{-2}]$
R_{ve}	Viscoelastic resistance	$[\text{s}\cdot\text{m}^{-2}]$

R_{th}	Thermodynamic resistance	[s.m ⁻²]
R	Radius	[m]
S	Volume averaged Lighthill source term	[kg.m ⁻³ .s ⁻²]
S_Q	Mass source	[m ³ .s ⁻¹]
S_h	Momentum source	[m]
S_{xy}	Spectral density between signals x and y	[EU ² .Hz ⁻¹]
R	Radius	[m]
T	Torque	[N.m]
U	Peripheral flow velocity	[m.s ⁻¹]
V	Volume	[m ³]
W	Relative flow velocity	[m.s ⁻¹]
Z	Elevation	[m]

Greek

α	Modal damping	[-]
α	Angle between horizontal and pipe axis	[rad]
α_l	Volume fraction of the liquid phase	[rad]
β	Void fraction	[-]
χ	Mass flow gain factor	[s]
δ	Small variation	[m]
η	Turbine efficiency	[-]
λ	Local loss coefficient	[-]
μ	Dynamic viscosity	[Pa.s]
μ'	Second viscosity	[Pa.s]
μ''	Bulk viscosity	[Pa.s]
μ_{equ}	Equivalent viscoelastic damping	[Pa.s]
ν	Specific speed parameter	[-]
ρ	Density	[kg.m ⁻³]
σ	Cavitation Thoma number	[-]
T_{ij}	Lighthill stress tensor component	[kg.m ⁻¹ .s ⁻²]
τ_{ij}	Viscous stress tensor component	[Pa]
Θ	Relaxation time	[Pa]
ξ	Total energy	[J]
ξ_k	Kinetic energy	[J]
ξ_p	Potential energy	[J]
ξ_s	Source energy	[J]

Subscripts

c	Cavitation
em	Electromagnetic
equ	Equivalent
exp	Experimental
l	Liquid phase
l	Linearized
n	Nominal
nuc	Nuclei
ref	Reference
sim	Simulation
$stdv$	Standard deviation
t	Turbine
$\bar{1}$	Runner low pressure section
$\bar{2}$	Elbow diffuser section
1	Runner high pressure section
\bar{I}	Machine low pressure section
I	Machine high pressure section
M	Referred to reduced-scale model
P	Referred to full-scale prototype

Mathematical Symbols

\tilde{y}	Fluctuating part
\bar{y}	Time averaged quantity
\vec{y}	Vector
$\int_V y dV$	Volume integral

Dimensionless Numbers

c_p	Pressure coefficient	$c_p = \frac{\tilde{p}}{\frac{1}{2} \cdot \rho \cdot U_1^2} [-]$
Fr	Froude number	$Fr = \sqrt{\frac{E}{g D_{ref}}} [-]$
N_{ED}	Speed factor	$N_{ED} = \frac{N D_{ref}}{\sqrt{E}} [-]$
ψ	Energy coefficient	$\psi = \frac{2E}{\omega^2 R_1^2} [-]$

Q_{ED}	Flow rate factor	$Q_{ED} = \frac{Q}{D_{ref}^2 \sqrt{E}} [-]$
T_{ED}	Torque factor	$T_{ED} = \frac{T}{\rho D_{ref}^3 E} [-]$
φ	Flow coefficient	$\varphi = \frac{Q}{\pi \omega R_1^3} [-]$

Acronyms

BEP	Best Efficiency Point
CFD	Computational Fluid Dynamics
DT	Draft Tube
EPFL	Ecole Polytechnique Fédérale de Lausanne
EU	Engineering Unit
GVO	Guide Vane Opening
HA	Hydroacoustic
HD	Hydrodynamic
LDV	Laser Doppler Velocimetry
LMH	Laboratoire de Machines Hydrauliques
NPSE	Net Positive Suction Head
OP	Operating Point
PIV	Particle Image Velocimetry
SAS	Scale Adaptative Simulation
SPS	Single Phase Simulation
SST	Shear Stress Transport
TPS	Two Phase Simulation
1D	One dimensional
3D	Three dimensional

Part I

Introduction

Chapter 1

Hydropower

A competitive, reliable and sustainable energy sector is essential for an economy, and this has been put under the spotlight in recent years by a number of issues, including the volatility in oil prices, interruptions to energy supply from non-member countries, blackouts aggravated by inefficient connections between national electricity networks, and the difficulties of market access for suppliers in relation to gas and electricity markets. These issues have pushed energy towards the top of international political agendas. The use of renewable resources such as sunlight, wind, waterfalls, tides, biomass or geothermal heat are seen as a key element in energy policy, reducing the dependence on fuel from nonmember countries, reducing emissions from carbon sources, and decoupling energy costs from oil prices. In 2008, the share of renewable in electricity production was around 18%, with hydraulic currently the leading renewable energy source as shown in Figure 1.1.

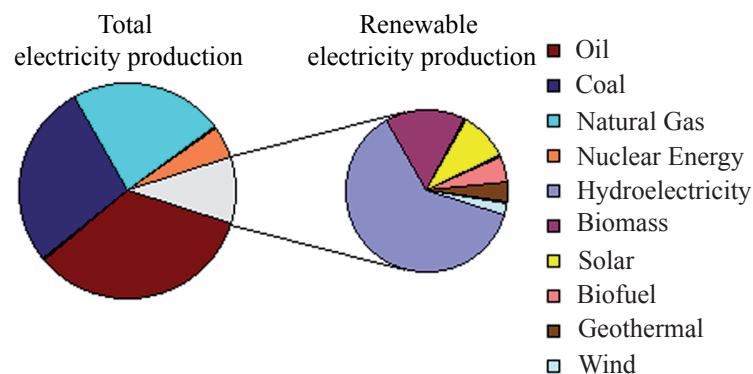


Figure 1.1: World-wide renewable energy sources in 2008 [32]

The hydroelectric world potential is considerable and may reach 36'000 TWh, while the economically exploitable capability is around 14'000 TWh which corresponds roughly to the world electricity production of 16'700 TWh in 2003. However in 2002, the hydroelectric world production was only 2'610 TWh. Therefore, hydroelectricity could substitute predominantly for world electricity production. The regions with the highest potential are Asia, Africa and South America. In reality, several limitations such as environmental

impacts on fauna and flora or social impacts because of population displacements and land transformations, explain why the world energy council tends to limit the hydroelectricity contribution and to increase the contribution of the new renewable energies. Worldwide projection of renewable energy consumption for the period 2006-2030 predict to more than double from 10'793 TWh to 21'733 TWh. The wind power is the renewable energy with the highest rate of development around 30%. For instance, in Europe, the wind energy production is planed to be at the same order to the hydroelectric production in 2030, see Figure 1.2.

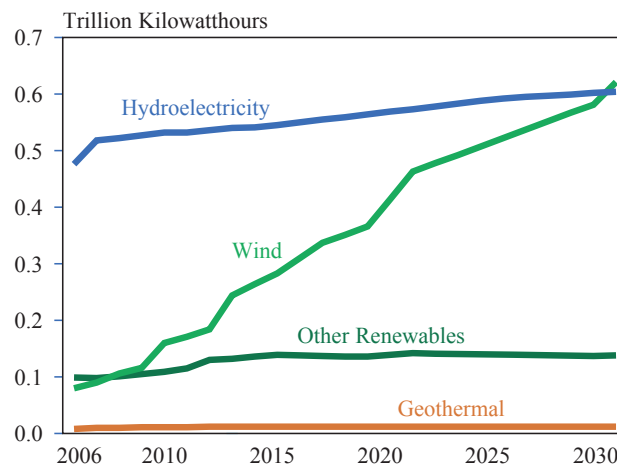


Figure 1.2: Prediction of renewable energy production in Europe [31]

Because of the uncertain nature of their production mode, these new renewable energies are considered as source of disturbances for the power grid. Moreover, the tendency of the European authorities to liberalize the energy electricity market, lead to a change of the economical strategies. Indeed, instantaneous pricing of electricity as function of the demand or the predictions contributes to a deregulation of the power grid due to the gain of economical interest for peak production. Hydropower plants are the only solution to restore the grid stability by allowing hydraulic machines, especially Francis turbines, to change quickly of operating points in a very large range of heads and power in order to cover the variation of the electrical demand. In such off-design operation, dynamic behavior of hydro generators and turbines integrated in the hydraulic system must be controlled to ensure the reliability and the safety of energy production on the power grid. Combined with these hydraulic machines operating in a wide power range, storage pump-turbine power plants are used. During low electrical demand, excess generation capacity coming from either nuclear or coal power plants or new renewable energy sources, is used to pump water into the higher reservoir, whereas during peak hours the power station works in the generating mode to convert hydraulic energy into electricity.

Chapter 2

Francis Turbines

2.1 Reaction Type Turbine

According to the hydrology and the exploitation strategy of a given hydraulic project, nominal flow rate Q_n and head H_n are determined for the site. Depending on the chosen angular runner frequency ω related to the grid frequency, the type of turbine can be selected between Pelton turbines, Francis turbines, Kaplan turbines or Bulb turbines. Figure 2.1, shows the classification of the different water turbines as function of the specific speed parameter ν defined as follows:

$$\nu = \frac{\omega (Q_n/\pi)^{0.5}}{(2gH_n)^{0.75}} \quad (2.1)$$

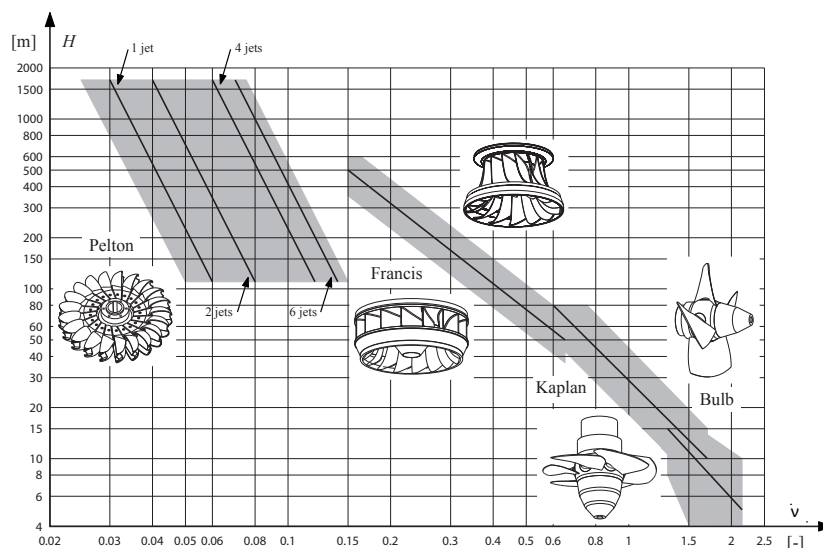


Figure 2.1: Turbine application range

Typically, for high head, medium head and low head, Pelton, Francis and Kaplan or Bulb turbines are respectively chosen. Francis turbines, constituted of five main components, are identified as reaction type turbines, see Figure 2.2. First, an angular momentum is created at the runner inlet by the set spiral case, stay vanes and guide vanes.

The opening angle of the guide vanes control the flow rate through the runner. Then the inlet angular momentum is recovered by the blades of the rotating runner to convert the angular momentum of the flow into mechanical momentum on the shaft. Finally, the draft tube component recovers both a part of the residual kinetic energy at the outlet runner and the potential energy between the runner outlet and the free surface of the downstream reservoir.

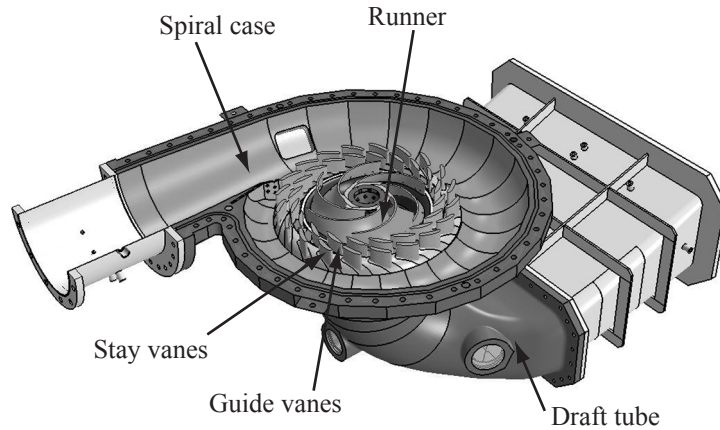


Figure 2.2: Francis Turbine components

2.2 Operating Point Parameters

Figure 2.3 shows the layout of the simplest Francis Turbine powerplant with one power unit connected respectively to an upstream and downstream reservoir by a penstock and a tailrace tunnel. The flow rate Q is constant along all the sections in the system. Considering a uniform pressure p and velocity C in any cross section A_k of the layout, the specific hydraulic energy of a fluid is constituted of the pressure, the potential and the kinetic specific energies:

$$gH_k = \frac{p_k}{\rho} + gZ_k + \frac{C_k^2}{2} \quad (2.2)$$

The specific energy E of the turbine is defined as:

$$E = gH = gH_I - gH_{\bar{I}} \quad (2.3)$$

and can be expressed as function of the difference of water levels and the head losses $gH_{r_{B \div I}}$ and $gH_{r_{\bar{I} \div \bar{B}}}$ in the penstock and the tailrace tunnel:

$$E = g(Z_B - Z_{\bar{B}}) - gH_{r_{B \div I}} - gH_{r_{\bar{I} \div \bar{B}}} \quad (2.4)$$

By convention, the low energy sections are denoted by an overbar. This available hydraulic energy E is then transferred into mechanical energy E_t by the runner. The ratio between these two quantities defines the global efficiency η of the turbine. Usually the operating

point of a turbine of outer runner diameter $2R_1$ rotating at the angular frequency ω is expressed in dimensionless form by the flow coefficient φ

$$\varphi = \frac{Q}{\pi\omega R_1^3} \quad (2.5)$$

and the energy coefficient ψ

$$\psi = \frac{2E}{\omega^2 R_1^2} \quad (2.6)$$

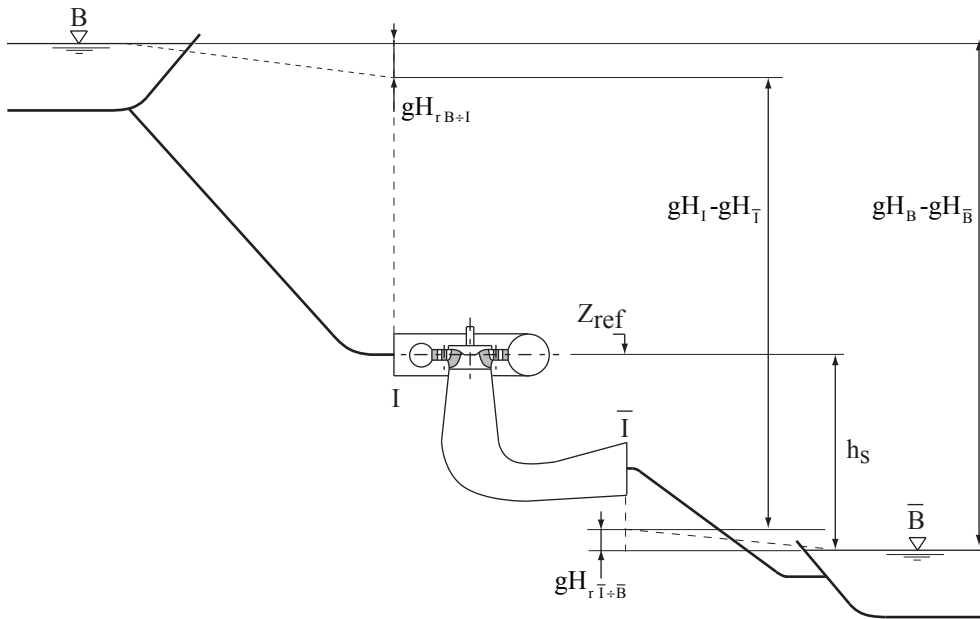


Figure 2.3: Layout of a powerplant and its energy line

2.3 The Thoma Number

The level setting h_s of a turbine, defined between the free surface of the downstream reservoir and a reference level in the machine, is decisive for the inception of cavitation phenomena, see Figure 2.3. To reduce the costs of the civil engineering constructions, the turbine is set up the highest possible above the free surface. However, the higher is the turbine, the more the pressure at the outlet runner decreases and may reach the vapor pressure p_v . The maximum setting level is generally defined to avoid the cavitation development at the runner outlet near the minimum inter-blades section area for a wide range of flow coefficient φ . The absolute pressure level in the turbine is defined by the Net Positive Suction Energy NPSE which corresponds to the difference between the suction cross section energy $gH_{\bar{I}}$ relative to the reference machine level and the specific energy corresponding to the vapor pressure p_v .

$$NPSE = (gH_{\bar{I}} - gZ_{ref}) - \frac{p_v}{\rho} \quad (2.7)$$

Expressing the specific energy of the section \bar{I} as function of the energy of the free surface at the atmospheric pressure p_a it yields to:

$$NPSE = \frac{p_a}{\rho} - gh_s - \frac{p_v}{\rho} + gH_{r_{\bar{I}:\bar{B}}} \quad (2.8)$$

A dimensionless number called the Thoma number σ is defined as:

$$\sigma = \frac{NPSE}{E} \quad (2.9)$$

Hence the higher is the setting level h_s , the lower is the Thoma number.

2.4 The Froude Number

The Froude number affects the distribution of cavitation in the flow since it determines the pressure gradient relatively to the size of the machine. It can be expressed as follows:

$$Fr = \sqrt{\frac{E}{gD_{ref}}} \quad (2.10)$$

Hence, when the Froude similitude is set up between the reduced scale model and the prototype, the cavitation development features the same dimensions with respect to the size of the machine. However, the Froude similitude on the reduced scale model is usually unfeasible since it requires a so low test head that the Reynolds number in the test rig is lower than a limit of validity for transposition laws to the prototype. At the opposite, the test head should be higher than the capability of the test rig. To assess the influence of the Froude difference between reduced scale model and prototype on the elevation Z of the vapor pressure p_v in the machine, the following expression can be used [38]:

$$\frac{Z_{ref} - Z_1}{Z_{ref} - Z_2} = \frac{Fr_1^2}{Fr_2^2} \quad (2.11)$$

The Froude number being usually smaller on prototype than on the reduced scale model, the elevation of the cavitation onset is higher on the prototype inducing lower cavitation development.

Chapter 3

Vortex Rope in Francis Turbines

3.1 Velocity Triangles

Despite the inlet swirl induced by the set spiral case, stay vanes and guide vanes, the flow leaving the runner at the best efficiency point is almost purely axial. However, in off design operating points a swirling flow at the outlet runner remains and gives rise to a vortex rope. The sense of rotation of this swirling flow depends on the flow coefficient φ and is explained by the velocity triangle at the outlet runner, see Figure 3.1.

The absolute flow velocity \vec{C} can be decomposed as the sum of the peripheral velocity \vec{U} and of the relative velocity \vec{W} :

$$\vec{C} = \vec{U} + \vec{W} \quad (3.1)$$

\vec{C}_m is the flow rate velocity in the meridional plane and \vec{C}_u is the peripheral component of the absolute flow velocity. The flow angle α and the blade angle β are defined respectively by the absolute velocity \vec{C} and the relative velocity \vec{W} with the peripheral velocity \vec{U} . Depending on the operating conditions, the flow structure at the outlet runner differs. At the best efficiency point the absolute velocity \vec{C}_1 is axial with no peripheral velocity \vec{C}_{u1} . In part load conditions, for which the flow rate is lower than the one at the best efficiency point, the flow is animated with a positive absolute circumferential velocity \vec{C}_{u1} in the same sense as the runner revolution. In that case the developed vortex rope has an helical shape which frequency precession is usually between 0.2 and 0.4 times the runner revolution frequency n . However, in full load conditions corresponding to high flow rate, the absolute circumferential velocity \vec{C}_{u1} is negative inducing a swirling flow rotating in the opposite direction of the runner. The vortex rope takes an axisymmetric shape. In both cases, cavitation may appear in the vortex core where the vapor amount strongly depends on the Thoma number σ value.

3.2 Vortex Rope Interaction with Hydraulic Systems

The vortex rope is an excitation source for the hydraulic system connected to the Francis turbine. Under given conditions the system response is amplified leading to severe pressure, and output power fluctuations. Three kind of interactions can be observed either on reduced scale model or prototype installation, see Dörfler [26]. The first one is observed at

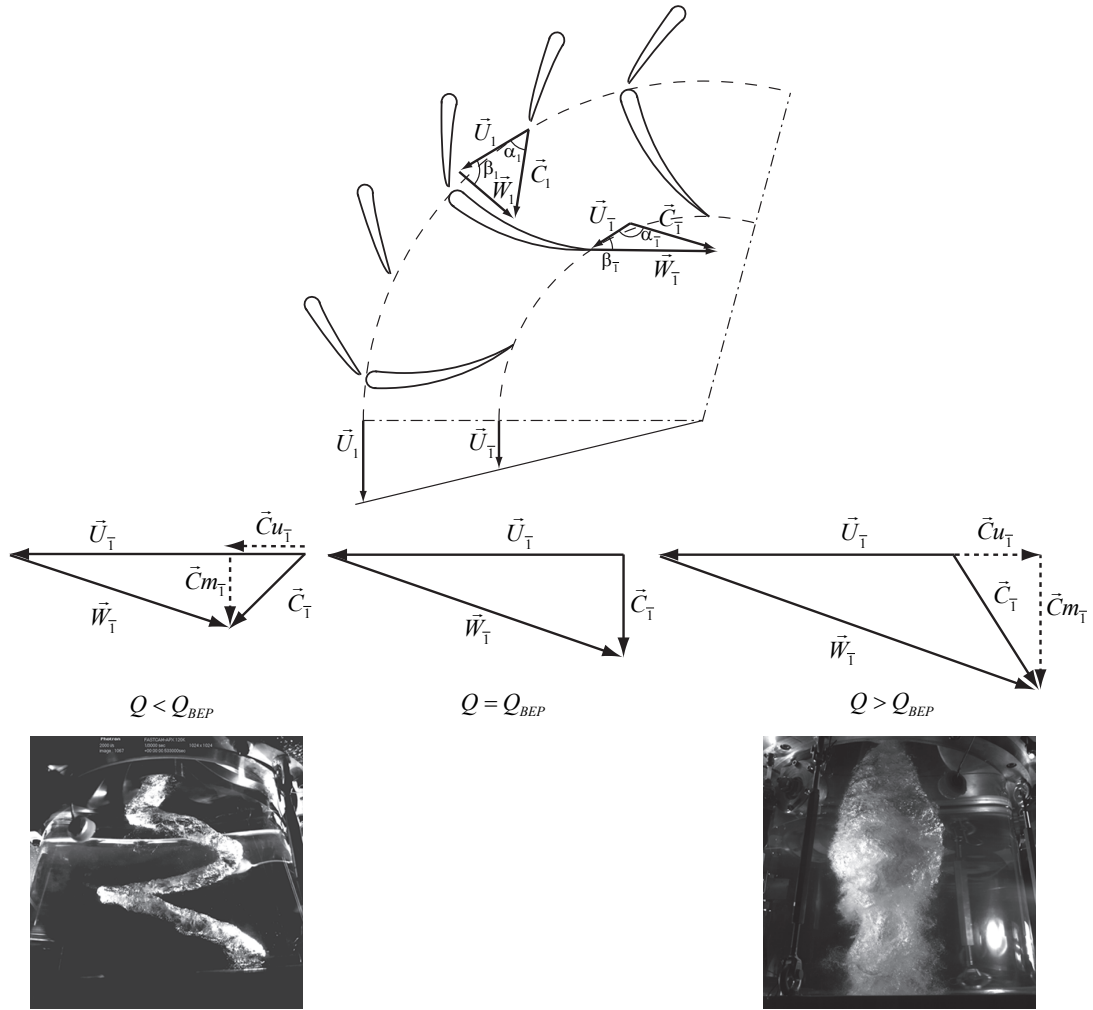


Figure 3.1: Velocity triangles and vortex rope shape

part load conditions for low flow rates. The helical vortex rope acts as an external forcing function on the hydraulic system, which precession frequency near 0.3 times the runner frequency n can match with one of the eigenfrequency of the system. The second one is observed at upper part load conditions for flow rates higher than the previous case but still lower than the best efficiency point. The occurrence of this resonance phenomenon is different to the part load resonance since frequency of pressure and output power fluctuations is much higher between 2 and 4 times the runner frequency n . This resonance appeared for hydraulic machines of high specific speed. The third one is observed at full load conditions for high flow rates. The axisymmetric vortex rope acts as an internal energy source leading to instability phenomenon called self excited surge. When instability occurs the cavitation volume of the vortex rope experiences axial pulsations at one of the eigenfrequency of the hydraulic system.

Chapter 4

State of the Art

4.1 Part Load Resonance

Experimental, numerical and analytical investigations have been carried out for more than fifty years to understand and to predict the part load resonance occurrence. In this section, the state of the art is divided in two parts. The first one deals with studies aiming to analyze the physics of the helical swirling flow which may enter in resonance with the system under given conditions. The second one recounts the studies which aim to predict and to simulate the resonance phenomenon.

The first investigations were focused on the understanding of the development of helical swirling flow in circular tubes with constant diameter. Swirl, defined as the ratio between the axial and the rotation momentums, has been shown to have large-scale effects on flow fields. Increasing the swirl level, an adverse axial pressure gradient induces a recirculation flow acting as a blockage, called vortex breakdown. In 1962, Harvey [45] was the first to visualize experimentally this phenomenon with an air swirling flow in a straight diffusing pipe. Depending on different combinations of Reynolds number and swirl number, different types of vortex breakdown may appear as observed by Sarpkaya [85] and by Faler and Leibovich [35]. Cassidy and Falvey [15] focused on the helical form and set up an experimental apparatus to study its occurrence, and to measure wall pressure fluctuations related to the vortex core precession. Afterwards many experimental investigations on the vortex breakdown phenomenon have been carried out [33, 13]. Moreover many theories and explanations of the vortex breakdown have been brought up by different investigators. Some of them assume that this phenomenon is based on the concept of critical state related to the wave phenomena such as Benjamin [8] or Bossel [9], whereas others believe in an analogy with boundary layer separation flow [44] or in hydrodynamic instability [79]. The helical cavitation vortex rope in Francis turbines is assumed to be a manifestation of vortex breakdown phenomenon. In 2006, Resiga et al. [89] pointed out analytically the unstable nature of the flow in the draft tube. The swirling flow at the runner outlet is modeled by a combination of three elementary vortices which parameters are identified by experimental measurements. Then, this model is combined with the Benjamin's theory [8] and stability is analyzed by computing eigenvalues of the linearized model for different flow coefficients φ . It is found out that the flow coefficient corresponding to the critical state is directly related to the sudden drop of draft tube pressure recovery coefficient. Moreover, for lower flow coefficients the flow is found to be subcritical and therefore can

sustain axisymmetric standing waves such as the ones observed when resonance occurs with the system. Recently Kuibin et al. [58] derived a mathematical model which can recover averaged axial and circumferential velocity profiles, as well as the vortex rope geometry, precessing frequency, and the level of pressure fluctuation at the wall. They stated that this model would be useful in the early stages of runner design, with computational effort several orders of magnitude less than the full three-dimensional unsteady flow numerical simulations. To understand and analyze the flow pattern in the draft tube of Francis turbines, many experimental investigations have been carried out. Nishi et al. [70, 71, 72] measured wall pressure fluctuations in an elbow draft tube at different flow regimes depending on both the strength of the inlet swirl generated by stationary guide vanes and the cavitation number defining the mean pressure level in the test rig. He focused on the regime where a stalled region in the center of the draft tube line was surrounded by a rotating helical vortex core. Influence of the cavitation number on the amplitude of pressure pulsations and on the vortex precession frequency was pointed out. Later in the framework of the FLINDT (Flow Investigation in a Draft Tube) project, advanced flow measurements such as LDA, LDV or PIV have been used for the understanding of the flow pattern. Ciocan et al. [20] measured velocity profiles at the draft tube inlet by LDA, and afterwards Iliescu et al. [48] extended the velocity field measurements to the whole draft tube cone using PIV system. The synchronization of the PIV measurements with vortex rope visualization allowed to quantify both the periodic velocity components and the rope shape in the cone. The influence of the cavitation number on the cavitation volume and its centerline has been investigated. Arpe [3, 2] performed extensive unsteady wall pressure measurements of the rotating vortex rope for different operating points in thirteen cross sections of the draft tube with 104 piezoresistive absolute pressure sensors. On the other hand, numerical CFD simulations of the helical vortex rope contributed as well to the understanding of the complex three dimensional hydrodynamic flow and were compared to experimental data. However, all these numerical simulations were performed for operating points out of resonance conditions with the hydraulic system. Ruprecht et al. [84, 14] was the precursor in numerical simulation of single phase helical swirling flows in Francis turbines. They stated that models for Reynolds Average Navier Stokes (RANS) simulations introduce damping effect and do not allow to predict with accuracy the length of the vortex structure. Hence, Very Large Eddy Simulation (VLES) has been performed. Frequency of pressure fluctuations is well predicted but amplitudes are underestimated. Such hybrid method mixing RANS simulation and Large Eddy Simulation has been used as well by Paik et al. [73] with a Detached Eddy Simulation (DES). Due to high computational costs, these hybrid methods have been widely replaced by RANS simulations by many authors [83, 87, 66, 86, 88, 92, 96]. Despite of a lower computational cost, prediction of the vortex rope precession is globally in accordance with experimental measurements. In the framework of the FLINDT project, Ciocan et al. [21] validated a standard $k-\epsilon$ numerical simulation with experimental data. Vortex rope frequency is over predicted but pressure amplitude is excellent. Moreover, PIV and LDV measurements of the velocity field allowed to compare the vortex core position.

The second part of this state of the art is devoted to studies aiming to predict and simulate a part load resonance. The method of transfer matrices was extensively used for the resonance risk evaluation of a system. Eigenfrequencies and eigenmodes shapes of the pressurized piping systems able to enter in resonance with the excitation induced by the

vortex rope, can be derived with this method, see Zielke et al. [95]. The most famous transfer matrix of the draft tube component is based on a key parameter introduced in 1970 by Ghahremani [40, 41] who analyzed the so called POGO instability experienced by many liquid propellant rockets, which results from a closed loop interaction between the first longitudinal structural mode of vibration, strongly influenced by the cavitation in the pump, and the fluid dynamics of the propulsion system. This key parameter is called cavitation compliance C_c defined as the rate of change of the cavitation volume with respect to change of pressure. Brennen and Acosta in 1973 [11] presented theoretical calculations of this parameter for a planar cascade flow and showed influence of blade angle, blade thickness and cavitation number. In 1982, Dörfler [25] was one of the first to measure the cavitation compliance for the Francis turbine vortex rope as function of the Thoma number. Based on this cavitation compliance parameter, he developed a transfer matrix model [24, 25] to predict pressure and torque fluctuations in the whole hydraulic system. Later in 1998, it has been shown by Couston and Philibert [22, 76] that this modeling is restricted to low frequency phenomena. Therefore these authors proposed a new transfer matrix based on the analytical expression of the vortex rope diameter and length derived from experimental observations. However, contrary to the lumped model defined by the cavitation compliance parameter, this model has two parameters to set up: the wave speed assumed as a constant along the draft tube and the rope length. Arpe et al. [4] extended this distributed approach by defining a wave speed depending on the curvilinear abscissa in the draft tube. Another approach, to define the transfer matrix of the turbine is to measure each term of the matrix from experiments on reduced scale model using an external excitation and the hydroacoustic intensimetry technique, see Jacob [49]. More than the turbine transfer matrix, the excitation source induced by the precessing vortex rope must be modeled. Dörfler [25] identified this source experimentally. He pointed out that measured pressure fluctuations in the cone are constituted of two components: a rotating part due to the passage of the vortex core near the wall and a synchronous part representing this excitation source. The rotating part is more important than the synchronous component out of resonance conditions. Therefore, pressure signals of sensors located in the same cross section are out of phase. However, when resonance occurs, synchronous component is predominant and all sensors are in phase. Dörfler assumed that this synchronous part is a component resulting of the excitation source and the hydraulic circuit response. Moreover he assumed that this excitation source is identical in cavitating regime or not. Based on these assumptions, he set up a procedure on scale model to derive experimentally this synchronous part as the excitation transmitted to the hydraulic circuit. Angelico et al. [1] confirmed that using three pressure transducers located in a cross section of the draft tube makes it possible to determine both the rotating part and the synchronous part of the pressure fluctuations. Another experimental approach, based on the hydroacoustic intensimetry technique allowed to compute the excitation source from the acoustic power emitted by the turbine, see Jacob [50]. The previous studies were aiming to derive experimentally the excitation induced by the vortex rope precession. On the other hand, analytical models of the excitation source have been derived such as Fanelli [36] who modeled the swirling flow as the superposition of two potential flow motions. However quantitative data to set up the model are missing. Finally, recent flow numerical simulations [84, 83, 87, 96] of the helical vortex rope computed the synchronous component of the pressure fluctuations. Only Ruprecht et al. [84]

injected this excitation in a 1D hydroacoustic powerplant model, but resonance was not simulated since compressibility of the vortex rope was not modeled.

4.2 Upper Part Load Resonance

Experimental, theoretical and numerical investigations were carried out for more than fifteen years to understand the upper part load resonance phenomenon. Dörfler was one of the first to try to explain experimentally this pressure surge [27]. Despite of extensive measurements of pressure fluctuations, he suggested a qualitative explanation of inertial waves traveling along the surface of the rotating cavitation volume with high propagation speed. Arpe [2] investigated experimentally this kind of resonance as well, in the framework of the FLINDT project. The pressure fluctuation measurements make apparent in the whole draft tube a characteristic frequency value at 2.5 times the runner frequency n . Moreover, a modulation of this frequency with the vortex rope precession frequency is pointed out. By the analysis of the phase shift of the high frequency component $2.5n$, Arpe et al. [4] confirmed Dörfler's explanation. Indeed, they interpreted the phase shift as the time propagation of a pressure wave, which excitation source is located in the elbow. Based on this experimental data, Nicolet et al. [68] explained the excitation source as periodic impacts of the vortex rope on the inner elbow part of the draft tube wall. They modeled this excitation with a momentum source combining sinusoidal pressure fluctuations with periodic dirac impulses both at the precession frequency. The amplitude spectrum of such excitation features energy at the vortex rope precession harmonics. Then, they performed a time domain simulation of the hydraulic system response to this excitation with the SIMSEN software. Finally, resonance was simulated due to a matching between the eigenfrequency of the system at $2.5n$ and one of the harmonics of the excitation source. As a result, a standing wave at $2.5n$ is experienced in the whole hydraulic system which is conflicting with the assumption of a traveling wave set by Arpe et al. [4]. The modeling of the excitation source, based on the shock assumption on the inner elbow part of the draft tube wall, is not shared by Koutnik et al. [54] for two reasons. The first one is that the high frequency component is not obviously a multiple of the vortex rope precession frequency. The second one is that the helical vortex rope may be relatively short and does not reach the draft tube elbow. Based on high speed camera visualizations, these authors believe in another theory being a rotation of the cavitation vortex core on its own axis featuring an elliptical cross section. The frequency of this self rotation is identified at the half of the pressure surge frequency. Habán et al. [43] showed that this elliptical cross section is an eigenmode shape of the cavitation swirling flow. Indeed, they performed a stability analysis of a swirling flow in an infinite cylindrical domain described by the set of equations including the Euler equations, the continuity equation and the Laplace equation dealing with the effect of surface tension on the vortex rope boundary. By computing the eigenvalues and the eigenmodes of this set of equations, they showed the existence of this elliptical shape rotating at a given frequency on its own axis. Then, Pochyly et al. [77] applied this methodology to the FLINDT case study where the draft tube domain is simplified by a divergent straight pipe which longitudinal profile of cross sections corresponds to the real elbow draft tube geometry. They confirmed the same results as Habán et al. [43].

4.3 Full Load Instability

In 1988, Jacob et al. [51] performed the first experimental investigations on the full load instability phenomenon. They analyzed pressure fluctuations on the reduced scale model of a prototype which featured this instability. Unfortunately the surge instability on test rig was much less significant. However they pointed out that pressure fluctuations frequency correspond to one of the eigenfrequency of the hydraulic system which they computed from a model based on the cavitation compliance parameter determined by experimental measurements. The same methodology was used to explain high load pressure fluctuations occurring in a two 140MW Francis turbine power plant in 1992 [52]. Later, modeling of the full load vortex rope was based on an additional parameter called mass flow gain factor being the rate of change of the cavitation volume with respect to change of the flow rate considered upstream to the cavitation volume. Initially this parameter was introduced with the combination of the cavitation compliance by Brennen and Acosta in 1976 [12] and 1978 [10] to analyse the POGO instability experienced by pumps in liquid propellant rockets. However, Koutnik and Pulpitel [57] applied to Francis Turbines this modeling approach but considering the definition of the mass flow gain factor according to the downstream flow rate to the cavitation volume. Using the transfer matrix method, they derived a stability diagram to explain a full load surge occurring on a four 39MW Francis turbine power plant. A similar approach based on cavitation parameters mapping was also successfully applied to explain inducer instabilities by Tsujimoto et al. in 1993 [90] and propeller instabilities by Duttweiler and Brennen in 2002 [30] and by Watanabe and Brennen in 2003 [93]. Chen et al. [18] derived a more complicated continuity equation from the consideration of the velocity triangle at the runner outlet which takes into account both upstream and downstream flow rates of the cavity. With an analytical model they analyzed the influence of the swirl intensity related to the upstream flow rate and the diffusor factor related to the downstream one, on the system stability. More recently, deriving the cavitation compliance and the mass flow gain factor parameters from steady single phase CFD simulations of the complete machine, Fleming et al [37] predicted instability of a prototype installation based on eigenvalues and eigenmodes analysis. However, no validation was available. These stability analysis based on constant cavitation compliance and mass flow gain factor parameters allow to predict frequencies and mode shapes. However, this method does not give any information about the amplitude of the oscillations. In 2006, Koutnik et al. [56] performed a time domain simulation of a full load instability occurring in a four 400MW Francis Pumped-Storage plant. In order to obtain finite fluctuations called "limit cycle", nonlinearity on the cavitation compliance as function of the Thoma number is introduced. Moreover, the system has been pushed to the limit of the instability by setting a mass flow gain factor parameter very low compared to the one derived from the stability analysis. Therefore, during the transient, the system enters in unstable conditions and nonlinearity of the cavitation compliance switches between stable and unstable conditions allowing to reach the limit cycle. It has been shown by authors that limit cycle is reachable only if nonlinearity of cavitation compliance is taken into account. As it can be observed, the definition of this mass flow gain factor remains woolly and depends on the author considered. Dörfler [28] was the first author to tackle openly this definition problem by evaluating the 1D models proposed in the literature in 2009. He showed that the choice between the upstream or the downstream flow rate is decisive to predict the stability limit of the system. In 2010

[29], he proposed a new model by using a weight function between the upstream and the downstream flow rates. Moreover, he introduced a new parameter which is a time delay of the effect of the upstream flow rate on the cavitation volume variation. Using unsteady two phase flow CFD simulations, they identified the set of their new model parameters by analyzing the response of the cavitating draft tube flow to a time dependent inlet flow rate boundary condition. This time delay effect has been already introduced by Tsujimoto et al. [91] for the analysis of rotating cavitation in the inducers of turbopumps. They found out that the consideration of this parameter allows to determine accurately the amplitude of the rotating modes. Finally, after having developed a general model taking into account both upstream and downstream flow rates [18], Chen et al carried out experimental investigations and CFD numerical simulations to highlight the influence of the downstream flow rate or the diffuser effect. They set up a facility able to generate cavitation volume pulsations induced by a bluff body [16] and a swirling flow [17] in a conical diffuser. They compared pressure fluctuations with a straight pipe and concluded that the diffuser or the downstream flow rate can be the cause of the measured high amplitude and low frequency oscillation occurring at low cavitation number.

Chapter 5

Objectives and Computing Methodologies

The aim of this research project is to predict and to simulate resonance or instability of a Francis Turbine connected to a hydraulic system. Part load and full load surges will be investigated. In both cases, the prediction of pressure fluctuations frequencies and amplitudes in the whole hydraulic system from three dimensional numerical flow simulations of the cavitating vortex rope is the main purpose. The low surging frequencies, corresponding to high wave length, allow to assume plane wave propagation in the pipes of the hydraulic system. Therefore, simulation of the hydroacoustic source propagation is performed with a one dimensional compressible model, called hydroacoustic (HA) model. Regarding the identification of the hydroacoustic source induced by the cavitating vortex rope, a three dimensional incompressible flow model, called hydrodynamic (HD) model, is adequate since low Mach numbers are involved. The HA model covers the entire hydraulic system including the source region corresponding to the draft tube of the Francis turbine whereas the HD model covers only the source region. Consequently two different solutions are obtained for the source region. According to Ribner's developments [81], the exact solution is a combination of both results where pressure and velocity fluctuations may be split into two components: an acoustic part due to propagation waves and a turbulent part due to the incompressible fluid motion. In the aeroacoustic field, the prediction of the flow-induced noise generated by turbulent flows is based on the fundamental assumption that the acoustic source is not dependent on the acoustic field: the unsteady flow generates sound but the sound waves do not affect the flow in any significant manner. However, in this present study, the hydroacoustic source is assumed to be dependent on the acoustic field. Indeed, the cavitation volume in the vortex core, being a decisive parameter in the identification of the hydroacoustic source, is strongly dependent on the hydroacoustic pressure and flow rate fluctuations.

To take into account this hydroacoustic feedback on the source two computing methodologies are proposed [82], see Figure 5.1:

- the hydroacoustic feedback is modeled in the HA model. In that case the time dependent sources due to the incompressible fluid motion identified in the HD model are computed in a first step. Then, the sources are injected in the HA model and the HA feedback model parameters are updated from the HD simulation results. Afterwards this computing methodology is called a "one way simulation".
- the hydroacoustic feedback is imposed to the HD model. HD and HA time domain simulations are performed simultaneously. At each time step, boundary conditions of the HD simulation are driven by the HA simulation results. Hence, computation of the sources in the HD model takes into account the HA feedback of the hydraulic system. Afterwards this computing methodology is called a "two way simulation".

This feedback effect can amplify or damp the pressure fluctuations in the system [5]. The main objective is to assess if one way simulations are sufficient to simulate resonance phenomena occurring in part load and full load operating conditions. In the framework of this research project, unsteady and steady flow numerical simulations with the HD model, have been performed respectively for part load and full load operating conditions. Hence, two way simulation was carried out only for part load conditions. In that case, simulation results derived from these two computing methodologies will be analyzed to identify in which conditions a two way simulation is necessary compared to a feedback modeling to predict accurately pressure fluctuations frequencies and amplitudes in the whole hydraulic system excited by a vortex rope of a Francis turbine draft tube.

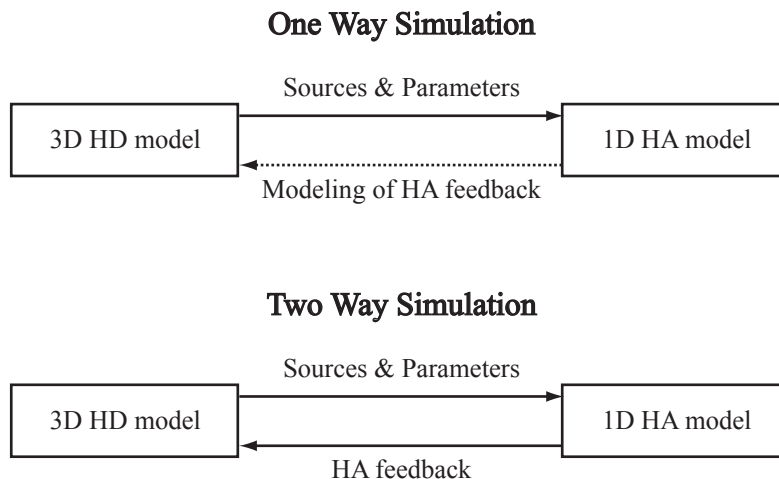


Figure 5.1: Consideration of the hydro-acoustic feedback on the HA sources in one way and two way simulations

Chapter 6

Document Organization

This thesis document is organized in four parts. Part I is the introduction of the present work including general informations about the situation of the hydraulic energy in the world with respect to the new renewable energies. Through this overview of the worldwide energy landscape, the motivation of this present work is described. Moreover, a presentation of the Francis Turbine hydraulic machines is available for novice readers and is followed by the fundamental aspect of the vortex rope generation induced by the velocity profile leaving the runner. Then, a literature review of the previous studies related to the resonance phenomena induced by the cavitating vortex rope is presented. Finally, the objectives and the computing methodologies are described.

In Part II, the computational tools and the models are presented. First in Chapter 7, the one dimensional HA draft tube model developed specifically for this research project is described in details. It is shown that this model is based on the HA model of a standard viscoelastic pipe which is modified to describe the dynamic behavior of the cavitating vortex rope precession by adding mass and momentum HA sources. On the other hand, the three dimensional HD model used to derive the HA sources is presented briefly in Chapter 8. Then, a description of the data flow between the one dimensional HA model and the three dimensional HD model is given for both one way and two way simulations. Finally, in Chapter 10, the new SIMSEN module allowing to perform small perturbation stability analysis of the hydraulic systems is presented. This tool has been developed in the framework of this research project to compute quickly the eigenmodes of a hydraulic installation which is useful for the prediction of resonance phenomena.

In Part III, part load operating conditions are investigated. The case study for which measurements are available for validation corresponds to an upper part load resonance phenomenon. In Chapter 11, a synthesis of the main measurements results from Arpe [2] are presented. Then, numerical investigations to simulate this resonance phenomenon are given in Chapter 12. In this chapter, first of all, the numerical setup of the HD model and the identification of the HA sources for the HA draft tube model are presented. Then, a preliminary validation of these HA parameters derived from the HD model is performed by simulating a standard part load resonance where the vortex rope precession frequency matches with the first eigenmode of the installation. Amplitudes of pressure fluctuations are compared to the literature. Once preliminary validation of the HA parameters is performed, simulation of the upper part load resonance is tackled and compared to Arpe's measurements [2]. Finally, a two way simulation is investigated to assess the influence on the computation of the HA parameters compared to a one way simulation.

In Part IV, full load operating conditions are investigated. The hydroelectric powerplant experiencing full load instability phenomenon is presented as the case study of this research project in Chapter 13. Experimental investigations on the reduced scale model have been performed and reported in Chapter 14. Finally, in Chapter 15, numerical investigations to predict and simulate the full load instability are presented. In this chapter, the numerical setup of the HD model and the identification of the HA draft tube model parameters are described. Moreover, prediction of the instability with the help of a small perturbation stability analysis is performed and confirmed by time domain simulation of the full load instability with nonlinear HA parameters. Finally, prediction of the prototype instability from the investigations on the reduced scale model is presented.

In Part V, the conclusions regarding the identification of the HA parameters from the HD model and the prediction of resonance phenomena are drawn. Then, perspectives to improve the accuracy of the prediction are presented

Part II

Computational Tools and Models

Chapter 7

One Dimensional Hydroacoustic (HA) Model

The one dimensional hydroacoustic model of the hydraulic system is setup with the SIM-SEN software. Initially, this software was developed by the EPFL for the transient and steady-state simulation of electrical power systems and adjustable speed drives having an arbitrary topology. Then, the capability of the software was extended to hydraulic components in order to be able to simulate the transient behavior of a complete hydro-electric power plant. The most common hydraulic components have been implemented such as pump-turbine, penstock, surge tank, gallery, valve, reservoir, etc. In order to get a common set of differential equations for both electrical and hydraulic parts, hydraulic models are based on the electrical analogy. In this Section, the hydraulic models of interest for this research project are presented. However, the reader can get an exhaustive description of the remaining hydraulic models in reference [67]. First, the Francis turbine runner model and the standard viscoelastic pipe model will be presented briefly. Then, an exhaustive presentation of the draft tube model developed in the framework of this project is given.

7.1 Francis Turbine Runner Model

Francis turbine can be considered as a quasisteady head H_t converting hydraulic energy into mechanical work, an inductance L_t related to the inertia effects of the water and a resistance R_t which models the head losses through the guide vanes closure. This resistance is effective only for small flow rate, below 5 % of the nominal value. The resulting differential equation is:

$$L_t \frac{dQ_i}{dt} + R_t Q_i = -H_t + h_I - h_{\bar{1}} \quad (7.1)$$

where h_I and $h_{\bar{1}}$ are respectively piezometric heads at the spiral case inlet and the outlet of the runner. Moreover, momentum equation applied to the rotational inertias is taken into account and leads to:

$$J_t \cdot \frac{d\omega}{dt} = T_t - T_{em} \quad (7.2)$$

where J_t , ω , T_t , T_{em} are respectively turbine inertia, rotational speed, mechanical torque and electromagnetic torque. Combined with Equation (7.1) the set of ordinary differential equations can be rewritten under the following matrix form:

$$\begin{bmatrix} L_t & 0 \\ 0 & J_t \end{bmatrix} \cdot \frac{d}{dt} \cdot \begin{pmatrix} Q_i \\ \omega \end{pmatrix} + \begin{bmatrix} R_t & 0 \\ 0 & 0 \end{bmatrix} \cdot \begin{pmatrix} Q_i \\ \omega \end{pmatrix} = \begin{pmatrix} -H_t + h_I - h_{\bar{1}} \\ T_t - T_{em} \end{pmatrix} \quad (7.3)$$

The pressure source $H_t(Q_i, \omega, y)$ and the mechanical torque $T_t(Q_i, \omega, y)$ are driven by the turbine characteristics which are nonlinear functions of the flow rate, the rotational speed and the guide vane opening.

7.2 Viscoelastic Pipe Model

By assuming uniform pressure and velocity distributions in the cross section and neglecting the convective terms, the one dimensional momentum and continuity balances for an elementary pipe filled with water of length dx , cross section A and wave speed a , yield to the well known Allievi hyperbolic equations, see [67], [94]. Using the finite difference method with a 1st order centered scheme discretization in space and a scheme of Lax for the flow rate variable, this approach leads to a set of nonlinear ordinary differential equations which can be represented as a T-shaped equivalent electrical scheme as shown in Figure 7.1. The RLC parameters of this equivalent scheme are given by:

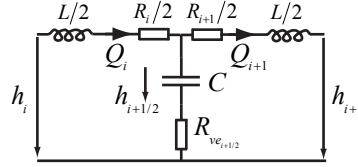


Figure 7.1: Equivalent electrical scheme of the viscoelastic pipe model of length dx

$$R_i = \frac{\lambda |Q_i| dx}{2gDA^2}; L = \frac{dx}{gA}; C = \frac{gAdx}{a^2} \quad (7.4)$$

where λ is the local loss coefficient. The hydraulic resistance R , the hydraulic inductance L and the hydraulic capacitance C correspond respectively to energy losses, inertia and storage effects due to wall deflection and fluid compressibility. Moreover, in order to predict accurately pressure fluctuation amplitudes and system stability, it is necessary to take into account the viscoelastic behavior due to an energy dissipation during the wall deflection. This additional dissipation leads to a resistance in series with the capacitance. This viscoelastic resistance is accounting for both fluid and pipe material viscoelasticity and can be expressed as:

$$R_{ve} = \frac{\mu_{equ}}{A \cdot \rho \cdot g \cdot dx} \quad (7.5)$$

with μ_{equ} the equivalent viscoelastic damping of both the fluid and the wall. The resulting set of nonlinear ordinary differential equations relative to the equivalent electrical circuit

is set up using Kirchoff laws and can be written under matrix form:

$$\begin{bmatrix} C & 0 & 0 \\ 0 & L/2 & 0 \\ 0 & 0 & L/2 \end{bmatrix} \cdot \frac{d}{dt} \cdot \begin{pmatrix} h_{i+1/2} \\ Q_i \\ Q_{i+1} \end{pmatrix} + \begin{bmatrix} 0 & -1 & 1 \\ 1 & R_i/2 + R_{ve} & -R_{ve} \\ -1 & -R_{ve} & R_{i+1}/2 + R_{ve} \end{bmatrix} \cdot \begin{pmatrix} h_{i+1/2} \\ Q_i \\ Q_{i+1} \end{pmatrix} = \begin{pmatrix} 0 \\ h_i \\ -h_{i+1} \end{pmatrix} \quad (7.6)$$

To model a viscoelastic pipe of length l made of n elementary pipes of length dx , the corresponding equivalent electrical scheme is presented in Figure 7.2 where n elementary equivalent electrical schemes are concatenated. Each mesh of the equivalent electrical scheme corresponds to the momentum conservation law applied to a pipe control volume of length dx whereas each node equation corresponds to the mass conservation law.

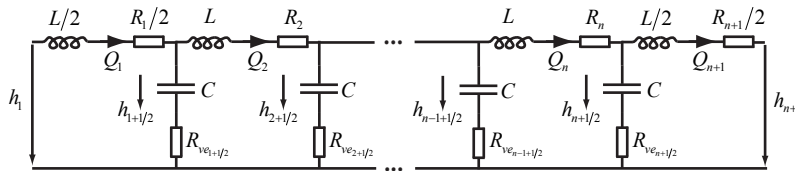


Figure 7.2: Equivalent electrical scheme of the viscoelastic pipe model of length l

7.3 Draft Tube Model

To model the draft tube component, the two diffuser channels separated by the pier are considered separately from the cone and the elbow parts where it is assumed that cavitation onset is located. For simplicity, the "draft tube" term will be used afterwards to name both the cone and the elbow parts. Therefore, the two diffuser channels are represented by a standard viscoelastic pipe model as described in Section 7.2 with an equivalent cross section. In the viscoelastic pipe model, the pressure force and the viscous force acting on the wall are modeled respectively with a Taylor development and the Darcy-Weisbach formulation [94]. However, this one dimensional modeling is inadequate to describe the dynamic behavior of the cavitating vortex rope precession. Hence, fundamental modifications of the viscoelastic pipe model are necessary to derive the draft tube model such as integration of mass and momentum sources but also thermodynamic damping modeling the energy dissipation during the phase change between the cavitation and the surrounding liquid. To derive the formulations of these mass sources and momentum sources, continuity and momentum balances are performed. The definition of the control volumes is based on the spatial discretization used for the standard viscoelastic pipe model. In Figure 7.3, a schematic representation of the control volumes is shown for a straight divergent pipe. Obviously, this control volume definition can be applied to the elbow draft tube as well. Continuity and momentum control volumes are overlapped to respect the spatial discretization of the state variables of the viscoelastic pipe model. The inlet and outlet of the momentum control volumes correspond to two followed pressure

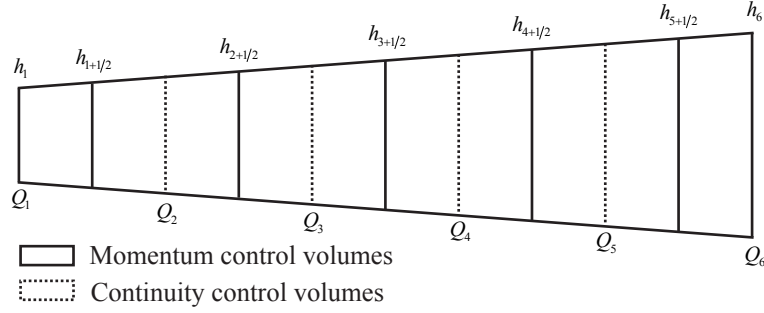


Figure 7.3: Overlapping of momentum and continuity control volumes used to derive HA draft tube model parameters

nodes in the electrical scheme given in Figure 7.2, whereas inlet and outlet of continuity control volumes correspond to two followed flow rate nodes.

7.3.1 Mass Source

The cavitation volume fluctuation of the vortex rope is considered as an hydroacoustic mass source for the entire hydraulic system. To define this mass source, the continuity balance is performed on a control volume V of length dx including a fluctuating cavitation volume V_c , see Figure 7.4. The control volume V is defined as the sum of the cavitation

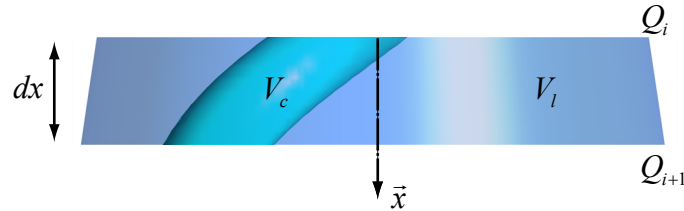


Figure 7.4: Control volume for mass balance

volume V_c and the liquid phase volume V_l :

$$V = V_c + V_l \quad (7.7)$$

Considering ρ as the density of the liquid phase, its mass is defined as:

$$m_l = \rho V_l \quad (7.8)$$

The time variation of this mass is:

$$\frac{dm_l}{dt} = V_l \frac{d\rho}{dt} + \rho \frac{dV_l}{dt} \quad (7.9)$$

Using Equation 7.7 and defining the time variation of the liquid mass as the difference between the inflow mass and the outflow mass, Equation 7.9 becomes:

$$\rho Q_i - \rho Q_{i+1} = V_l \frac{d\rho}{dt} + \rho \frac{dV}{dt} - \rho \frac{dV_c}{dt} \quad (7.10)$$

Introducing the cavitation volume fraction β , Equation 7.10 can be rewritten as:

$$\rho Q_i - \rho Q_{i+1} = (1 - \beta) V \frac{d\rho}{dt} + \rho \frac{dV}{dt} - \rho \frac{dV_c}{dt} \quad (7.11)$$

The liquid phase is assumed to follow a barotropic law which yields to the following relation between the density variation and the pressure p :

$$\frac{1}{\rho} \frac{d\rho}{dt} = \frac{1}{E_l} \frac{dp}{dt} \quad (7.12)$$

with E_l the liquid phase bulk modulus.

Moreover, in the source region where cavitation is taken into account, elastic pipe is considered. Energy dissipation due to the viscoelastic behavior of the pipe wall is negligible compared to the energy dissipation during the phase change between the cavitation and the surrounding liquid. This dissipation will be considered in Section 7.3.4. The elastic behavior, sets a relation between the cross section variation and the pressure variation:

$$\frac{1}{A} \frac{dA}{dt} = \frac{D}{eE_c} \frac{dp}{dt} \quad (7.13)$$

with e and E_c respectively the thickness and the Young modulus of the pipe wall.

Combining Equations 7.12 and 7.13 in Equation 7.11 and using the same spatial discretization of the state variables as the viscoelastic pipe model, it yields to:

$$Q_i - Q_{i+1} = (1 - \beta) \frac{A dx}{\rho a_0^2} \frac{dp_{i+1/2}}{dt} - \frac{dV_c}{dt} \quad (7.14)$$

with a_0 the wave speed in the pipe without cavitation onset defined as:

$$a_0^2 = \frac{1}{\rho \left(\frac{1}{E_l} + \frac{D}{eE_{wall}} \right)} \quad (7.15)$$

Using the piezometric head h as state variable and the compliance definition C_0 from Equation 7.4, it yields to:

$$Q_i - Q_{i+1} = (1 - \beta) C_0 \frac{dh_{i+1/2}}{dt} - \frac{dV_c}{dt} \quad (7.16)$$

Therefore, the mass source S_Q of the one dimensional HA draft tube model induced by the fluctuating cavitation volume is defined as:

$$S_{Q_{i+1/2}} = - \frac{dV_c}{dt} \quad (7.17)$$

7.3.2 Momentum Source

From literature, it is well known that a momentum source, induced by the vortex rope precession, may lead to resonance phenomena with the hydraulic system. This momentum source is usually called the synchronous component. Dörfler [25] identified this source

experimentally and pointed out that measured pressure fluctuations in the cone are constituted of two components: a rotating part due to the passage of the vortex core near the wall and a synchronous part. Moreover, he stated that this source is independent of the cavitation amount in the vortex core. Therefore, he identified experimentally the source in a cavitation free regime. The aim of this section is to define this momentum source for the one dimensional HA model using momentum balance on a control volume V of length dx in free cavitation regime, see Figure 7.5. The axial momentum conservation

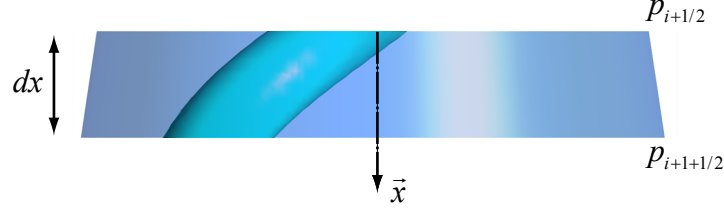


Figure 7.5: Control volume for momentum balance

law projected on the curvilinear abscissa \vec{x} can be written as:

$$(pA)_{i+1/2} - (pA)_{i+1+1/2} + \vec{F} \cdot \vec{x} - \rho g A \sin(\alpha) dx = \rho V \frac{dC}{dt} \quad (7.18)$$

with C the fluid velocity projected on the curvilinear abscissa and \vec{F} the total force applied by the vortex rope precession on the wall Σ including both pressure and viscous forces. The k^{th} component of this force can be expressed as follows:

$$F_k = - \int_{\Sigma} p n_k dS + \int_{\Sigma} \tau_{kj} n_j dS \quad (7.19)$$

Moreover, α defines the angle between horizontal and pipe axis to take into account the weight of the fluid. Developing the pressure force on the outlet surface $i + 1 + 1/2$ by a first order Taylor development yields to:

$$(pA)_{i+1/2} - \left[(pA)_{i+1+1/2} + \frac{\partial}{\partial x} \left((pA)_{i+1+1/2} \right) dx \right] + F_x - \rho g A \sin(\alpha) dx = \rho V \frac{dC}{dt} \quad (7.20)$$

For each momentum control volume an elementary curvilinear abscissa vector \vec{x} is defined and the force projection F_x can be expressed as follows:

$$F_x = \sum_{k=1}^3 F_k x_k \quad (7.21)$$

Considering a small control volume of length dx , it is assumed a constant cross section and Equation 7.20 can be rewritten as:

$$-A dx \frac{\partial p}{\partial x} + F_x - \rho g A \sin(\alpha) dx = \rho V \frac{dC}{dt} \quad (7.22)$$

Using the flow rate Q and the piezometric head h as state variables it yields to:

$$\frac{1}{gA} \frac{dQ}{dt} + \frac{\partial h}{\partial x} + \frac{F_x}{\rho g V} = 0 \quad (7.23)$$

The resulting spatial discretized momentum equation using the inductance definition from Equation 7.4 is:

$$L \frac{dQ_{i+1}}{dt} + h_{i+1+1/2} - h_{i+1/2} + \frac{F_x dx}{\rho g V} = 0 \quad (7.24)$$

Therefore, the momentum source S_h of the one dimensional HA draft tube model induced by the vortex rope precession is defined by:

$$S_{h_{i+1}} = \frac{F_x dx}{\rho g V} \quad (7.25)$$

7.3.3 Modeling of Hydroacoustic Feedback on Sources

In the aeroacoustic field, the prediction of the flow-induced noise generated by turbulent flows is based on the fundamental assumption that the acoustic sources are not dependent on the acoustic field: the unsteady flow generates sound but the sound waves do not affect the flow in any significant manner. However, in the case of the interaction between the hydraulic circuit and the cavitating vortex rope dynamic flow, a dependency of the mass source with the hydroacoustic field is assumed and modeled in the one dimensional HA draft tube model. Indeed, the hydroacoustic field can influence drastically the cavitation volume of the vortex rope. Regarding the feedback on the momentum source, it is considered as negligible for the modeling approach since the source region is considered as compact with respect to the hydraulic system inducing uniform HA pressure in the source region. Pressure and flow rate fluctuations in the draft tube domain may be split into two components: a hydroacoustic part (HA) due to the propagation waves in the hydraulic system and a hydrodynamic part (HD) due to the incompressible fluid motion. Therefore, the fluctuations of the cavitation volume can be decomposed as follows:

$$\frac{dV_c}{dt} = \left. \frac{dV_c}{dt} \right|_{HD} + \left. \frac{dV_c}{dt} \right|_{HA} \quad (7.26)$$

The cavitation volume fluctuations due to the hydroacoustic field considered in a control volume is modeled as a function of the pressure, the upstream and downstream flow rates:

$$V_c|_{HA} = f(h_{i+1/2}, Q_i, Q_{i+1}) \quad (7.27)$$

A first order Taylor development allows to express the cavitation volume fluctuation as function of the hydroacoustic state variable fluctuations.

$$\left. \frac{dV_c}{dt} \right|_{HA} = \frac{\partial V_c}{\partial h_{i+1/2}} \frac{dh_{i+1/2}}{dt} + \frac{\partial V_c}{\partial Q_i} \frac{dQ_i}{dt} + \frac{\partial V_c}{\partial Q_{i+1}} \frac{dQ_{i+1}}{dt} \quad (7.28)$$

Combining Equations 7.26 and 7.28 in the discretized continuity equation 7.16:

$$Q_i - Q_{i+1} = ((1 - \beta) C_0 + C_c) \frac{dh_{i+1/2}}{dt} + \chi_i \frac{dQ_i}{dt} + \chi_{i+1} \frac{dQ_{i+1}}{dt} - \left. \frac{dV_c}{dt} \right|_{HD} \quad (7.29)$$

with C_c , χ_i , χ_{i+1} respectively the cavitation compliance parameter, the upstream and downstream mass flow gain factor parameters defined by:

$$C_c = -\frac{\partial V_c}{\partial h_{i+1/2}} \quad \chi_i = -\frac{\partial V_c}{\partial Q_i} \quad \chi_{i+1} = -\frac{\partial V_c}{\partial Q_{i+1}} \quad (7.30)$$

If these parameters are considered as constants, the feedback of the hydroacoustic field on the mass source is linearly proportional to the state variables. Such constant parameters can be used to analyze the dynamic behavior of the system in quasi steady operating conditions with small deviations. This linear feedback can modify the system eigenfrequencies and stabilize or make unstable the system. However for large fluctuations of state variables, the constant linear relation is no longer valid. Therefore these parameters must be considered as nonlinear and dependent on state variables.

7.3.4 Thermodynamic Damping

Regarding the standard viscoelastic pipe model, the resistance in series with the capacitance accounts for both fluid and pipe material viscoelasticity to model energy dissipation. In the case of the draft tube modeling, the energy dissipation due to the cavitation volume compliance must be taken into account as well. By considering the set constituted of the wall material, the liquid fluid and the cavitation volume, the rheological model based on the Kelvin-Voigt model is given in Figure 7.6 with its corresponding equivalent electrical scheme. The equivalent electrical scheme shows that wall, liquid and cavitation volume

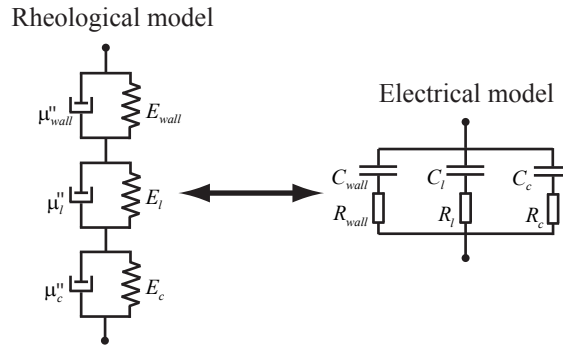


Figure 7.6: Rheological model and equivalent electrical scheme

are subjected to the same pressure since a 1D approach is used. However, it is assumed that most of the energy dissipation is due to the cavitation compliance C_c rather than the wall deflection C_{wall} or the compressibility of the liquid C_l . Indeed, the cavitation compliance is much higher than the wall and liquid compliances. Hence, when a pressure variation occurs, or voltage variation, almost all the current goes through the cavitation resistance R_c to dissipate the energy. This modeling approach is exhaustive and would require to distinguish separately the three contributions. Therefore, the dissipation due to the wall deflection is neglected and an homogeneous approach of the fluid including liquid and cavitation is considered [75]. The so-called bulk viscosity μ'' is used to model this dissipation which is considered to represent internal processes breaking a thermodynamic equilibrium between the cavitation volume and the surrounding liquid. Such modeling

approach has been used and validated with a water hammer simulation in cavitating pipe flows by Pezzinga in 2003 [75]. This parameter appears in the Navier-Stokes equation considered for compressible fluid:

$$\rho \frac{d\vec{C}}{dt} = -\vec{\nabla} p + \vec{\nabla} \cdot \tau + \vec{f} \quad (7.31)$$

Using the cylindrical coordinates and projecting along the pipe axis \vec{x} of the draft tube component it yields to:

$$\rho \frac{dC}{dt} = -\frac{\partial p}{\partial x} + \frac{1}{r} \frac{\partial}{\partial r} (r\tau_{rx}) + \frac{\partial}{\partial x} (\tau_{xx}) + f_x \quad (7.32)$$

with τ_{rx} and τ_{xx} respectively the tangential and normal viscous stresses to the pipe cross section defined by:

$$\tau_{rx} = \mu \left(\frac{\partial C}{\partial r} \right) \quad \tau_{xx} = (2\mu + \mu') \frac{\partial C}{\partial x} \quad (7.33)$$

μ and μ' are two viscosity coefficients similar to the Lamé parameters in linear elasticity with μ' the so-called second viscosity which is assumed to contribute only to the normal stress τ_{xx} . The homogeneous bulk viscosity μ'' is introduced and defined as:

$$\mu'' = \mu' + \frac{2}{3}\mu \quad (7.34)$$

The bulk viscosity is a volume viscosity associated to the variation of the fluid particle volume usually encountered in viscoelastic medium where the molecular structure is modified at a characteristic time scale Θ . For any isovolume evolution or incompressible evolution, this volume viscosity disappears. In a case of a cavitating flow where molecular structure depends strongly on the state variables of the system this parameter must be taken into account to model the energy dissipation. Equation 7.32 is integrated over a control volume V of length dx with constant cross section A :

$$\int_V \rho \frac{dC}{dt} dV = - \int_V \frac{\partial p}{\partial x} dV + \int_V \frac{1}{r} \frac{\partial}{\partial r} (r\tau_{rx}) dV + \int_V \frac{\partial}{\partial x} (\tau_{xx}) dV + \int_V f_x dV \quad (7.35)$$

The aim of this Eulerian formulation is to identify how the bulk viscosity is modeled in the equivalent electrical scheme of the HA draft tube model. Afterwards, each volume integral is developed considering an elementary volume defined by $dV = r dr d\theta dx$. The pressure term corresponding to the pressure forces can be developed as:

$$\begin{aligned} \int_V \frac{\partial p}{\partial x} dV &= \pi R^2 \int_{i+1/2}^{i+1+1/2} \frac{\partial p}{\partial x} dx \\ &= A (p_{i+1+1/2} - p_{i+1/2}) \end{aligned} \quad (7.36)$$

Regarding the tangential stress component, the volume integral can be expressed in terms of the Darcy-Weisbach friction factor $\tau_0 = \rho \frac{\lambda C^2}{8}$:

$$\begin{aligned} \int_V \frac{1}{r} \frac{\partial}{\partial r} (r\tau_{rx}) dV &= 2\pi dx \int_0^R \frac{\partial}{\partial r} (r\tau_{rx}) dr \\ &= -2\pi R dx \tau_0 \end{aligned} \quad (7.37)$$

Assuming in the normal stress component only the contribution of the bulk viscosity μ'' [75], the volume integral becomes:

$$\begin{aligned}
\int_V \frac{\partial}{\partial x} (\tau_{xx}) dV &= \int_V \frac{\partial}{\partial x} \left[\left(\frac{4}{3} \mu + \mu'' \right) \frac{\partial C}{\partial x} \right] dV \\
&= \pi R^2 \int_{i+1/2}^{i+1+1/2} \frac{\partial}{\partial x} \left[\left(\frac{4}{3} \mu + \mu'' \right) \frac{\partial C}{\partial x} \right] dx \\
&= A \left[\left(\frac{4}{3} \mu + \mu'' \right) \frac{\partial C}{\partial x} \right]_{i+1/2}^{i+1+1/2} \\
&\approx A \left[\mu'' \frac{\partial C}{\partial x} \right]_{i+1/2}^{i+1+1/2}
\end{aligned} \tag{7.38}$$

Considering the angle α between the horizontal and the draft tube control volume axis \vec{x} , the volume force induced by the fluid's weight is developed as:

$$\begin{aligned}
\int_V f_x dV &= - \int_V \rho g \sin(\alpha) dV \\
&= -\rho g A dx \sin(\alpha)
\end{aligned} \tag{7.39}$$

The piezometric head h and the flow rate Q are the state variables of the model and the spatial discretization used for the viscoelastic pipe model is employed:

$$\begin{aligned}
\frac{dx}{gA} \frac{dQ_{i+1}}{dt} &= - (h_{i+1+1/2} - h_{i+1/2}) - \frac{\lambda dx}{2gDA^2} Q_{i+1}^2 \\
&\quad + \frac{\mu''_{i+1+1/2}}{A\rho g dx} (Q_{i+2} - Q_{i+1}) - \frac{\mu''_{i+1/2}}{A\rho g dx} (Q_{i+1} - Q_i)
\end{aligned} \tag{7.40}$$

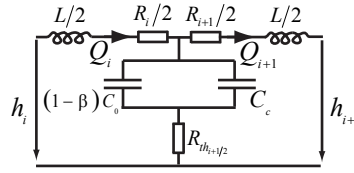
Using the *RLC* electrical formulation defined by Equation 7.4, Equation 7.40 can be rewritten as:

$$\begin{aligned}
L \frac{dQ_{i+1}}{dt} &+ h_{i+1+1/2} - h_{i+1/2} + R_{i+1} Q_{i+1} \\
&+ R_{th_{i+1+1/2}} (Q_{i+1} - Q_{i+2}) - R_{th_{i+1/2}} (Q_i - Q_{i+1}) = 0
\end{aligned} \tag{7.41}$$

with R_{th} the thermodynamic resistance modeling the dissipation due to the bulk viscosity μ'' defined as:

$$R_{th_{i+1/2}} = \frac{\mu''_{i+1/2}}{A\rho g dx} \tag{7.42}$$

The corresponding electrical scheme of the draft tube model corresponding to a pipe length of length dx which satisfies Equation 7.41 is given in Figure 7.7. Many authors tried to set up a mathematical model to quantify this bulk viscosity for cavitating pipe flows. The theory of Mandelshtam and Leontovich reported by Landau and Lifshitz [61] was reconsidered by Bartolini and Siccardi [7] for the formulation of an additional dissipation

Figure 7.7: Equivalent electrical scheme of a draft tube pipe of length dx

term in unsteady cavitating flows. This theory takes into consideration local relaxation processes leading to a bulk viscosity expressed as:

$$\mu'' = \Theta_\beta ((1 - \beta) \rho + \beta \rho_c) (a_0^2 - a^2) \quad (7.43)$$

where Θ_β , a_0 and a are respectively a relaxation time constant relative to the rate of change of cavitation volume fraction β , the wave speed in cavitating free regime and the wave speed for the mixture of liquid and gas. However, Pezzinga [74] used this model and obtained results worse than with a simple constant bulk viscosity in the comparison with experimental results. Later Ewing [34] derived an analytical bulk viscosity considering small variations of temperature T of gas bubbles due to heat exchange between gas and surrounding liquid. The final expression of the bulk viscosity is:

$$\mu'' = \Theta_T a^4 \frac{k-1}{k} \frac{((1-\beta)\rho + \beta\rho_c)^2 \beta\rho_c RT}{p^2} \quad (7.44)$$

In Equation 7.44, Θ_T is a relaxation time for the rate of change of temperature and k the ratio between specific heats at constant pressure and constant volume. It has been showed that this thermodynamic approach does not always explain the energy dissipations observed in cavitating water hammer flows. Pezzinga used the same approach as Ewing to model the relaxation phenomena of gas release leading to the following expression [75]:

$$\mu'' = \Theta_\beta a^4 \frac{((1-\beta)\rho + \beta\rho_c)^2 \beta\rho_c RT}{p^2} \quad (7.45)$$

Combining the gas release relaxation and the temperature relaxation expressed respectively by Equations 7.45 and 7.44 it yields to the following bulk viscosity:

$$\begin{aligned} \mu'' &= \left(\Theta_\beta + \frac{k-1}{k} \Theta_T \right) \frac{((1-\beta)\rho + \beta\rho_c)^2 \beta\rho_c RT a^4}{p^2} \\ &= \Theta \frac{((1-\beta)\rho + \beta\rho_c)^2 \beta\rho_c RT a^4}{p^2} \end{aligned} \quad (7.46)$$

where Θ is an equivalent relaxation time for both phenomena. Pezzinga [75] validated this model showing that pressure dependent wave speed and bulk viscosity allow to reproduce results of experimental measurements of water hammer transients with cavitation. This analytical formulation has been derived by considering homogeneous bubbly cavitation in pipe cross section. Obviously, the case of a cavitating vortex rope either at part load or at full load conditions is far from this assumption. However, this parameter being unknown, this formulation is used as a first approach to get an order of magnitude of this parameter.

7.3.5 Draft tube model adapted for Part Load Conditions

In the framework of the FLINDT project, an upper part load resonance was observed on the EPFL PF3 test rig of the Laboratory for Hydraulic Machines. The resonance frequency appeared between 2 and 4 times the runner frequency n which does not correspond to the helical vortex rope precession around $0.3n$. This frequency corresponds to a high order eigenmode of the installation [68]. As it will be explained later in Section 10.3, a distributed draft tube model featuring several pressure nodes is necessary to capture the shape of the eigenmode. On the other hand, before simulating this upper part load resonance, a preliminary validation test case is set up. It corresponds to a typical part load resonance where the vortex rope precession frequency matches with the first eigenmode of the installation. In that case, a lumped model featuring one pressure node is sufficient to perform the resonance simulation, see Section 10.3. The lumped and distributed draft tube models are given in Figure 7.8. For a reading convenience of the figure, the volume fraction of the liquid phase is defined as $\alpha_l = 1 - \beta$.

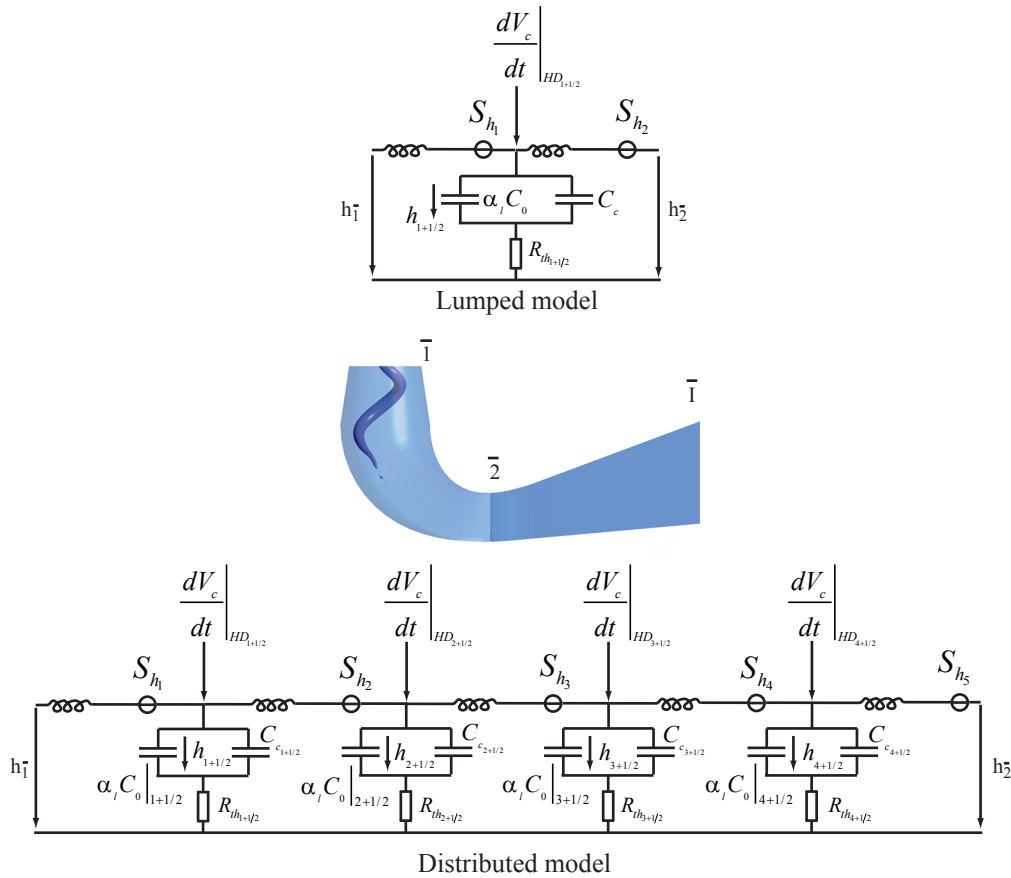


Figure 7.8: Equivalent electrical schemes of the part load draft tube models

These models include both momentum and mass sources described in Sections 7.3.2 and 7.3.1. To set up the part load draft tube model, the following parameters must be determined:

- the equivalent capacitance $C_{equ} = (1 - \beta) C_0 + C_c$ defining an equivalent wave speed according to the definition of the capacitance, see Equation 7.4,
- the momentum sources S_{hi} which represent the force induced by the cavitating vortex rope precession,
- the time variation of the cavitation volume $\left. \frac{dV_c}{dt} \right|_{HD}$ due to the HD incompressible fluid motion,
- the thermodynamic damping μ'' defining the resistance in series with the capacitance which models energy dissipation during the phase change between liquid and gas.

7.3.6 Draft tube model adapted for Full Load Conditions

The BC Hydro’s Mica hydroelectric power plant located in Canada’s province of British Columbia, experiences a full load instability phenomenon when unit operates at power output in excess of 460 MW. In order to analyze this phenomenon, the reduced scale model of the Mica prototype turbine has been installed on the EPFL PF2 test rig of the Laboratory for Hydraulic Machines. Despite of the difference of the hydraulic circuit layout connected to the Francis turbine, the instability was reproduced on the test rig. In both configurations, the measured pressure fluctuations corresponded to the first eigenmode of the installation. As it will be explained later in Section 10.3, a lumped model featuring one pressure node, has been chosen as shown in Figure 7.9. For a reading convenience of the figure, the volume fraction of the liquid phase is defined as $\alpha_l = 1 - \beta$. At full load operating conditions, the Francis turbine features an axi-symmetric rope leaving the runner. Hence no precession is observed like in the helical vortex rope case. It is assumed that the momentum HA source is negligible compared to the mass source induced by the cavitating axi-symmetric rope. Moreover, the HA feedback on the mass source is limited to the downstream flow rate to the cavitation volume. Indeed due to the very low wave speed in the cone, very large downstream flow rate fluctuations are experienced compared to the upstream one. This fundamental assumption meet the conclusions drawn by Chen

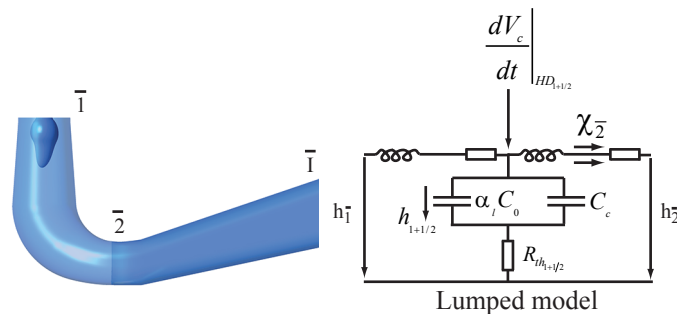


Figure 7.9: Equivalent electrical schemes of the full load draft tube model

et al [16, 17] who assume that the full load instability would be due to the destabilization of the swirling flow because of the diffuser. Therefore, the continuity Equation 7.29 is simplified as follows:

$$Q_{\bar{1}} - Q_{\bar{2}} = ((1 - \beta) C_0 + C_c) \frac{dh_{1+1/2}}{dt} + \chi_{\bar{2}} \frac{dQ_{\bar{2}}}{dt} - \left. \frac{dV_c}{dt} \right|_{HD} \quad (7.47)$$

To set up the full load draft tube model, the following parameters must be determined:

- the equivalent capacitance $C_{equ} = (1 - \beta) C_0 + C_c$ defining an equivalent wave speed according to the definition of the capacitance, see Equation 7.4,
- the mass flow gain factor $\chi_{\bar{2}}$ which represents the HA feedback of the downstream flow rate on the mass source,
- the time variation of the cavitation volume $\left. \frac{dV_c}{dt} \right|_{HD}$ due to the HD incompressible fluid motion,
- the thermodynamic damping μ'' defining the resistance in series with the capacitance which models energy dissipation during the phase change between liquid and gas.

7.3.7 Synthesis

Regarding the investigated phenomenon, the draft tube model involves different parameters which are summarized in Table 7.1:

- a distributed model is only used for the simulation of the upper part load resonance since the high order resonating eigenmode features a lower wavelength than the length of the draft tube component, see Section 10.3.
- the mass source induced by the cavitation volume fluctuations due to the HD incompressible fluid motion should be taken into account for every cases even for full load instability simulations. However, in the framework of this research project, steady simulations with the HD model are performed to identify the full load draft tube model parameters. Hence, this unsteady quantity was not evaluated from the simulations, see Section 9.
- the HA flow rate feedback on the mass source is neglected for part load operating conditions and only the effect of the downstream flow rate $Q_{\bar{2}}$ is taken into account for the full load operating conditions.
- the HA pressure feedback on the mass source, represented by the cavitation compliance C_c , is considered for all the cases, allowing to predict the modification of the eigenmodes shapes and the corresponding frequencies of the hydraulic system.
- the momentum source is used to model the excitation induced by the helical vortex rope occurring at part load operating conditions. In the case of the axi-symmetric vortex rope only the mass source is taken into account.
- the thermodynamic damping μ'' , modeling the energy dissipation during the phase change between liquid and gas, is considered for all the simulation cases.

Table 7.1: Synthesis of the HA draft tube model parameters used according to the simulated phenomenon

		Part load resonance	Upper part load resonance	Full load instability
Spatial discretization		Lumped	Distributed	Lumped
HD Mass source	$\frac{dV_c}{dt} \Big _{HD}$	Included	Included	Included
Upstream mass flow gain factor	χ_1	Not included	Not included	Not included
Downstream mass flow gain factor	χ_2	Not included	Not included	Included
Cavitation compliance	C_c	Included	Included	Included
Momentum source	S_h	Included	Included	Not included
Thermodynamic damping	μ''	Included	Included	Included

Chapter 8

Three Dimensional Hydrodynamic (HD) Model

8.1 Governing Equations

8.1.1 Single Phase Flow Simulation (SPS)

The motion of flow is governed by the conservation laws of momentum and mass. In this present study, the fluid is assumed to be incompressible for single phase simulations. The resulting differential form of the incompressible Navier Stokes equations are nonlinear in space and time:

$$\frac{\partial C_i}{\partial x_i} = 0 \quad (8.1)$$

$$\rho \frac{\partial C_i}{\partial t} + \rho C_j \frac{\partial C_i}{\partial x_j} = -\frac{\partial p}{\partial x_i} + \frac{\partial \tau_{ij}}{\partial x_j} + \rho f_i \quad (8.2)$$

The continuity equation 8.1 corresponds to the mass conservation law and the momentum equation 8.2, expresses the first principle of mechanics stating that the particular derivative of the flow velocity depends on the sum of pressure forces, viscous forces and body forces such as gravity. The fluid is considered as Newtonian and the shear stress is determined by the dynamic viscosity μ and the strain rate tensor D_{ij} :

$$\tau_{ij} = 2\mu D_{ij} \quad \text{with} \quad D_{ij} = \frac{1}{2} \left(\frac{\partial C_i}{\partial x_j} + \frac{\partial C_j}{\partial x_i} \right) \quad (8.3)$$

Leading to the incompressible momentum equation for Newtonian fluids:

$$\rho \frac{\partial C_i}{\partial t} + \rho C_j \frac{\partial C_i}{\partial x_j} = -\frac{\partial p}{\partial x_i} + \mu \frac{\partial^2 C_i}{\partial x_j \partial x_j} + \rho f_i \quad (8.4)$$

8.1.2 Two Phase Flow Simulation (TPS)

The basic concept of the mixture model or the so-called homogeneous model is used for this present study. This model treats the inside and outside of the cavitation as one

continuum. Therefore it is based on a cavity flow field as a compressible viscous fluid with variable density being a function of the vapor volume fraction β :

$$\rho_m = \beta\rho_c + (1 - \beta)\rho \quad (8.5)$$

Subscripts c and l refer respectively to the cavitation and liquid phase. A common flow field is shared by the two phases leading to the following assumptions:

$$\vec{C}_m = \vec{C}_l = \vec{C}_c \quad (8.6)$$

$$p_m = p_l = p_c \quad (8.7)$$

The cavitation volume fraction β is an additional variable of the system which is computed by solving an additional transport equation coupled to the mass and momentum conservation equations of the mixture:

$$\frac{\partial \rho_m}{\partial t} + \frac{\partial (\rho_m C_{m_i})}{\partial x_i} = 0 \quad (8.8)$$

$$\frac{\partial (\rho_m C_{m_i})}{\partial t} + \frac{\partial (\rho C_{m_i} C_{m_j})}{\partial x_j} = -\frac{\partial p_m}{\partial x_i} + \frac{\partial \tau_{ij}}{\partial x_j} + \rho_m f_i \quad (8.9)$$

$$\frac{\partial \beta}{\partial t} + \frac{\partial \beta C_{m_i}}{\partial x_i} = \frac{1}{\rho_c} S_{cl} \quad (8.10)$$

The shear stress tensor is expressed with the Newton Stokes model:

$$\tau_{ij} = 2\mu_m D_{ij} - \frac{2}{3}\mu_m \frac{\partial C_{m_k}}{\partial x_k} \delta_{ij} \quad D_{ij} = \frac{1}{2} \left(\frac{\partial C_{m_i}}{\partial x_j} + \frac{\partial C_{m_j}}{\partial x_i} \right) \quad (8.11)$$

Leading to the compressible momentum equation:

$$\frac{\partial (\rho_m C_{m_i})}{\partial t} + \frac{\partial (\rho C_{m_i} C_{m_j})}{\partial x_j} = -\frac{\partial p_m}{\partial x_i} + \mu_m \left(\frac{\partial^2 C_{m_i}}{\partial x_j \partial x_j} + \frac{1}{3} \frac{\partial}{\partial x_i} \left(\frac{\partial C_{m_k}}{\partial x_k} \right) \right) + \rho_m f_i \quad (8.12)$$

By convenience the subscript m for the mixture is omitted when equations are considered for a two phase flow simulation. In the transport equation 8.10 of the cavitation volume fraction, the right hand term is the mass flow rate per unit volume for the vapor phase considering the condensation and the vaporization processes:

$$S_{cl} = S_{cl}^{vap} + S_{cl}^{cond} \quad (8.13)$$

These source terms are modeled with the Rayleigh-Plesset equation relating the dynamic of a bubble radius to the pressure variable and taking into account that vaporization is initiated at nucleation sites.

$$S_{cl}^{vap} = C^{vap} \frac{3\rho_c \alpha_{nuc} (1 - \beta)}{R_0} \left[\frac{2}{3} \max \left(\frac{p_v - p}{\rho}, 0 \right) \right]^{1/2} \quad (8.14)$$

$$S_{cl}^{cond} = -C^{cond} \frac{3\rho_c \beta}{R_0} \left[\frac{2}{3} \max \left(\frac{p - p_v}{\rho}, 0 \right) \right]^{1/2} \quad (8.15)$$

Empirical constants for vaporization C^{vap} and condensation C^{cond} processes are used to take into account the different time scales. In the present study, constants by default are used: $C^{vap} = 50$ and $C^{cond} = 0.01$. Moreover, the nuclei volume fraction is set to $\alpha_{nuc} = 5 \cdot 10^{-4}$, and the nucleation sites radius R_0 is set to $10^{-6}m$.

8.2 Reynolds Averaged Navier Stokes Equations

With the Reynolds-averaged approach, all of the unsteadiness is averaged out i.e. all unsteadiness is regarded as part of turbulence. On averaging, the non-linearity of the Navier Stokes equations gives rise to terms that must be modeled. If the flow is unsteady, time averaging cannot be used and is replaced by ensemble averaging which splits any turbulent quantity f into a mean value \bar{f} and a fluctuating value f' as:

$$f = \bar{f} + f' \quad (8.16)$$

where \bar{f} is the ensemble average i.e. the average over a large set of independent flow realizations:

$$\bar{f} = \lim_{N \rightarrow \infty} \frac{1}{N} \sum_{i=1}^N f_i \quad (8.17)$$

However, the use of ensemble averages for compressible flows, like for homogeneous two phase flow simulations, induces extra terms leading to improper conservation laws. To avoid the too complex form of mean flow equations obtained using simply ensemble averaging, mass weighted averaging is preferred. For compressible flow simulations, the ensemble averaging is conserved for the density and the pressure. Any other quantity f is split into a mass weighted average \tilde{f} and a fluctuation now denoted f'' defined as:

$$f = \tilde{f} + f'' \quad \tilde{f} = \frac{\rho f}{\bar{\rho}} \quad (8.18)$$

Therefore the averaged continuity and momentum equations can, for incompressible single phase flows, be written in tensor notation:

$$\frac{\partial \bar{C}_i}{\partial x_i} = 0 \quad (8.19)$$

$$\rho \frac{\partial \bar{C}_i}{\partial t} + \rho \bar{C}_j \frac{\partial \bar{C}_i}{\partial x_j} = -\frac{\partial \bar{p}}{\partial x_i} + \mu \frac{\partial^2 \bar{C}_i}{\partial x_j \partial x_j} - \rho \frac{\partial \overline{C'_i C'_j}}{\partial x_j} + \rho f_i \quad (8.20)$$

However, considering a compressible two phase flow simulation, the following set of differential equations is solved:

$$\frac{\partial \bar{\rho}}{\partial t} + \frac{\partial \bar{\rho} \tilde{C}_i}{\partial x_i} = 0 \quad (8.21)$$

$$\frac{\partial \bar{\rho} \tilde{C}_i}{\partial t} + \frac{\partial \bar{\rho} \tilde{C}_i \tilde{C}_j}{\partial x_j} = -\frac{\partial \bar{p}}{\partial x_i} + \bar{\mu} \left(\frac{\partial^2 \tilde{C}_i}{\partial x_j \partial x_j} + \frac{1}{3} \frac{\partial}{\partial x_i} \left(\frac{\partial \tilde{C}_k}{\partial x_k} \right) \right) - \frac{\partial \bar{\rho} \overline{C''_i C''_j}}{\partial x_j} + \bar{\rho} f_i \quad (8.22)$$

$$\frac{\partial \bar{\beta}}{\partial t} + \frac{\partial \bar{\beta} \tilde{C}_i}{\partial x_i} = \frac{1}{\rho_c} \bar{S}_{cl} \quad (8.23)$$

8.3 Turbulent Modeling

Due to the averaging of the equations, the unknown terms $\overline{\rho C_i'' C_j''}$ called Reynolds stresses appear. The essence of turbulence modeling is to close the equation system by defining laws to predict the Reynolds stresses. In this present study, eddy viscosity turbulence models are used. These models are based on the Boussinesq's hypothesis, assuming the same dependence of the Reynolds stresses on the traceless strain rate tensor as for the viscous stresses of a Newtonian fluid:

$$-\overline{\rho C_i'' C_j''} = \mu_t \left(\frac{\partial \tilde{C}_i}{\partial x_j} + \frac{\partial \tilde{C}_j}{\partial x_i} \right) - \frac{2}{3} \overline{\rho} \delta_{ij} k \quad (8.24)$$

The proportionality coefficient μ_t is called eddy viscosity and the second term, involving the specific kinetic turbulence energy k , is introduced for ensuring the correct trace of the Reynolds stress tensor. Analogous to the eddy viscosity hypothesis is the eddy diffusivity hypothesis, which states that the Reynolds fluxes of a scalar Φ are linearly related to the mean scalar gradient:

$$-\overline{\rho C_i'' \phi} = \Gamma_t \frac{\partial \phi}{\partial x_i} \quad (8.25)$$

where Γ_t is the eddy diffusivity which has to be prescribed. By convenience, the average symbols are omitted afterwards. Subject to these hypotheses, the Reynolds averaged momentum equation for compressible flow becomes:

$$\frac{\partial (\rho C_i)}{\partial t} + \frac{\partial}{\partial x_j} (\rho C_i C_j) = -\frac{\partial p'}{\partial x_i} + (\mu + \mu_t) \frac{\partial^2 C_i}{\partial x_j \partial x_j} + \frac{\mu}{3} \frac{\partial}{\partial x_i} \left(\frac{\partial C_k}{\partial x_k} \right) \quad (8.26)$$

with p' the modified pressure defined by:

$$p' = p + \frac{2}{3} \rho k + \mu_t \frac{\partial C_k}{\partial x_k} \quad (8.27)$$

The kinetic turbulence energy and the dissipation due to the eddy viscosity are two unknowns of the set of equations. To close the set of equations, both unknowns are solved using separate transport equations. According to the chosen turbulence model, transport equations differ. In this present study two turbulence models have been used: the SAS-SST model and the SST model respectively for single phase incompressible simulations and for two phase compressible simulations. The $k - \omega$ based SST model accounts for the transport of the turbulent shear stress and gives highly accurate predictions of the onset and the amount of flow separation under adverse pressure gradients. The $k - \omega$ model fails to properly predict the onset and amount of flow separation from smooth surfaces. The main reason of this deficiency is that it does not account for the transport of the turbulent shear stress which induces an over prediction of the eddy viscosity. Therefore the SST model proposes to introduce a limiter to the formulation of the eddy-viscosity with the help of a blending function. Moreover, a second blending function allows to weight the dissipation terms of the $k - \epsilon$ model in the free shear flow and the $k - \omega$ model close to the solid walls. Regarding the SAS-SST model, derived by Menter and Egorov [65], the particularity is to include a term with a second derivative of the velocity field in

the dissipation transport equation. This term allows to the model to operate in a scale-adaptive simulation (SAS) mode. The characteristic length scale of diffusion is adjusted dynamically and is proportional to the size of the resolved eddies. Standard turbulence models, on the other hand, always provide a length-scale proportional to the thickness of the shear layer. They do not adjust to the local flow topology and are therefore overly diffusive. This model allows to preserve the SST model in the RANS regime, particularly in boundary layers, and to activate the SAS capability in URANS regions. Similar to the DES formulation, the SAS model also benefits from a switch in the numerical treatment between the steady and the unsteady regions.

8.4 Space and Time Discretization

The spatial domain is discretized with a structured mesh. Governing equations including the additional transport equations for the turbulence modeling are integrated over control volumes built around the mesh nodes. The first step in the numerical solution of these exact volume integral differential equations is to create a coupled system of linearized algebraic equations by converting each volume integral term into a discrete form. ANSYS CFX stores the variables at the same set of grid points and uses the same control volumes for all variables, such a grid is called co-located. However it is recognized that standard co-located methods may lead to a decoupled pressure field to the velocity. Therefore, an alternative discretization for the mass flows is used to avoid the decoupling by applying a momentum-like equation to each integration point of the control volume. Finally, the solution fields are stored at the mesh nodes. However, various volume integral terms in the equations require solutions or solution gradients to be approximated at the integration points. Finite element shape functions are consequently used to evaluate the solution and its variation within mesh elements. Various methods can be applied to express the advection fluxes as a function of nodal variable values since the essential tradeoff between robustness and accuracy lies herein. In our present study, the second order "High Resolution Scheme" is used. Regarding the time discretization, a second order backward euler scheme is used. This scheme is robust, implicit, conservative in time, and does not create a timestep limitation. Time and space discretizations lead to a linear set of equations to solve. ANSYS CFX uses a Multigrid (MG) accelerated Incomplete Lower Upper (ILU) factorization technique for solving the discrete system of linearized equations.

Chapter 9

Data Flow

To identify the excitation source of the cavitating vortex rope, the 3D hydrodynamic (HD) model is used. For part load investigations, unsteady simulations of the draft tube flow are performed in single phase and two phase configurations whereas for full load investigations only steady single phase simulations are carried out. Therefore, the procedure to exchange data with the 1D hydroacoustic (HA) model between the two cases differ and are presented in this Section.

9.1 Part Load Operating Conditions

The cavitation volume of the vortex rope is a decisive parameter for the simulation of a part load resonance. This volume is strongly dependent on the HA pressure and flow rates fluctuations. To take into account this HA feedback on the cavitation volume two computing methodologies are proposed. The first computing methodology called "one way simulation" is based on the modeling of the HA feedback in the HA model. The time dependent sources due to the incompressible fluid motion identified in the HD model are computed in a first step. Then, the sources are introduced in the HA model and the HA feedback model parameters are updated from the HD simulation results. The second computing methodology called "two way simulation" consists in imposing the HA feedback to the HD model. HD and HA time domain simulations are performed simultaneously. At each time step, boundary conditions of the HD simulation are driven by the HA simulation results. Hence, computation of the HA sources in the HD model takes into account the HA feedback of the hydraulic system.

9.1.1 One Way Simulation

Each mesh and node equation of the equivalent electrical scheme of the draft tube model given in Figure 9.1 corresponds respectively to the momentum and continuity balances applied to a control volume. Therefore to derive the draft tube model parameters, the HD model has been discretized into control volumes corresponding to the HA model discretization. As a first step the unsteady simulation of the draft tube flow with the HD model is performed. Cavitation volume and total force including pressure and viscous effects projected on the curvilinear abscissa \vec{x} are computed in each control volumes and stored for each time step. From these two quantities the time evolution of the four draft

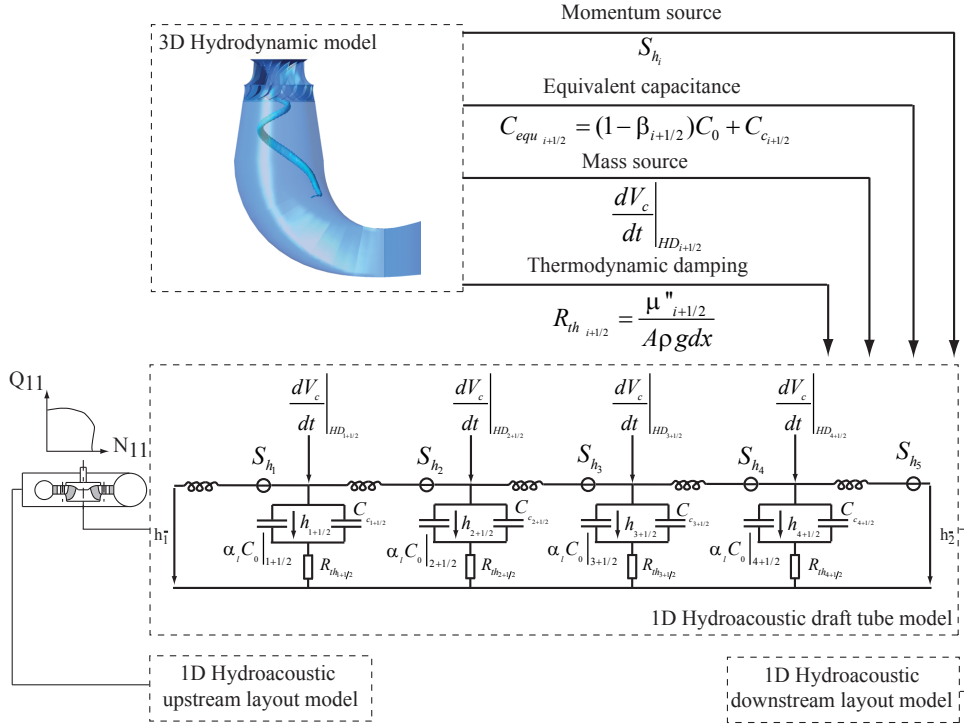


Figure 9.1: Data flow during a one way simulation for part load resonance simulation

tube HA model parameters, given in Figure 9.1, can be determined as a post-processing step and introduced in the HA model of the hydraulic system. The momentum sources S_{h_i} are computed from the total forces according to Equation 7.25. For a reading convenience of the figure, the volume fraction of the liquid phase is defined as $\alpha_l = 1 - \beta$. On the other hand the cavitation volume fractions allows to compute the three remaining parameters:

- the time derivative of the cavitation volume which is evaluated using a finite difference centered scheme,
- the equivalent capacitance $C_{equ} = (1 - \beta) C_0 + C_c$ is a function of the cavitation volume fraction β and the cavitation compliance C_c being function of β as well. Two methodologies can be used to define the dependence of the cavitation compliance with the cavitation volume fraction β : the "derivative method" and the "analytical method", see Section 12.2.3. The "derivative method" consists in defining the dependence as a pre-processing step whereas the "analytical method" is based on an analytical model, which input data is the cavitation volume fraction, allowing to compute the wave speed parameter during the simulation. Then the equivalent capacitance is deduced from Equation 7.4,
- the thermodynamic damping is function of the cavitation volume fraction, the wave speed and the pressure according to Equation 7.46. This pressure can be split into two components: a HA part due to the propagation waves and a HD part due to the incompressible fluid motion. However, since a one way simulation is carried out, the HA part of the pressure field is not taken into account. Hence a reference pressure of the HD model is considered and set to the constant outlet pressure of

the HD computational domain. Regarding the wave speed, it is computed from the equivalent capacitance according to Equation 7.4.

Figure 9.1 shows the exchanged data between the HD and the HA models which is illustrated by a distributed model with several pressure nodes. However, it has been noticed in Section 7.3.5 that a lumped model has been used as well especially for part load resonance simulation at the first system eigenfrequency. For that case the procedure is exactly the same.

9.1.2 Two Way Simulation

The "two way simulation" consists in imposing the HA feedback to the HD model by setting unsteady boundary conditions driven by the HA simulation results. Hence, computation of the HA sources in the HD model takes into account the hydraulic feedback of the hydraulic system. For the investigated test case, the Francis turbine is directly connected to a downstream reservoir corresponding to a constant outlet pressure. However, the inlet boundary condition is updated at each time step according to the HA simulation result. The momentum source is computed from the force induced by the fluid motion acting on the wall, whereas the mass source is computed from the time derivative of the cavitation volume. In a "One way simulation", the HA feedback was modeled by linear approximation leading to the introduction of the cavitation compliance C_c , see Section 7.3.3. In the case of the "two way simulation", this modeling is not necessary anymore since it is assumed that this feedback is already included in the HD model thanks to the unsteady boundary conditions. Hence the cavitation compliance is not taken into account in the HA draft tube model. The data flow between the HA and the HD models during a "two way simulation" is shown in Figure 9.2.

9.2 Full Load Operating Conditions

To derive the full load draft tube model parameters, steady simulations of the draft tube flow with the HD model are performed. The flow topology due the axi-symmetric shape of the vortex rope allows to perform this kind of computation. Therefore, the procedure to perform a time domain simulation of the full load instability, is different to the part load investigations. First, the mass source corresponding to the cavitation volume fluctuation due to the HD fluid motion can't be evaluated and is therefore neglected. Moreover, the mass flow gain factor parameter χ_2 is computed as a pre-processing step in the same way as Flemming et al. [37] which is considered as a constant. More than this parameter, nonlinear variation laws of the equivalent capacitance C_{equ} and the thermodynamic damping μ'' are derived by assuming a dependency to the pressure state variable, see Figure 9.3. For a reading convenience of the figure, the volume fraction of the liquid phase is defined as $\alpha_l = 1 - \beta$. Two way simulation is not considered since steady simulations are performed.

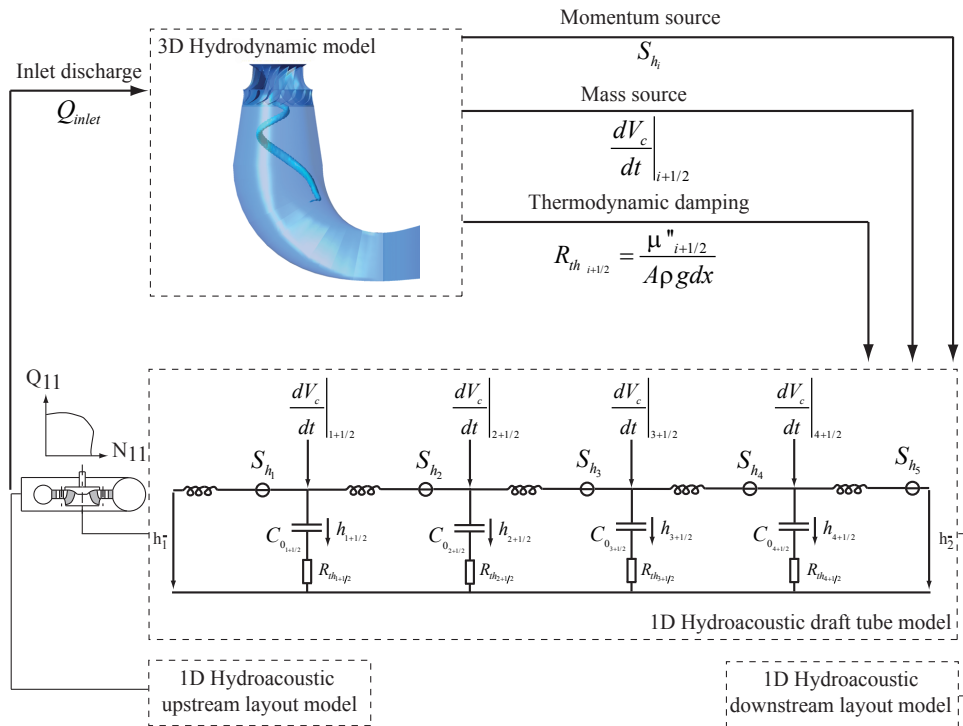


Figure 9.2: Data flow during a two way simulation for part load resonance simulation

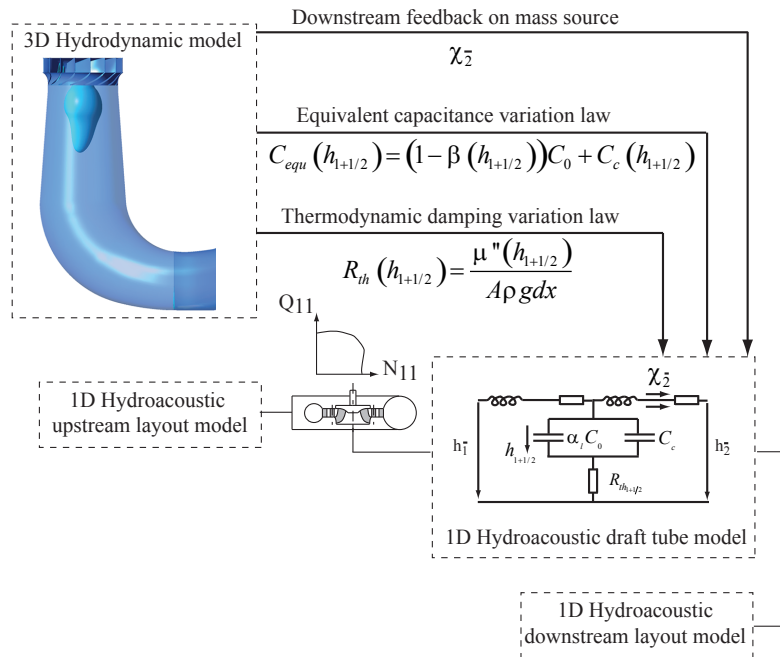


Figure 9.3: Data flow during a one way simulation for full load instability simulation

Chapter 10

Small Perturbation Stability Analysis Tool

10.1 Set of Differential Equations

The dynamic behavior of a system modeled with the SIMSEN software, is given by a set of n first order nonlinear ordinary differential equations of the following form:

$$[A] \cdot \frac{d\vec{X}}{dt} + [B(\vec{X})] \cdot \vec{X} = \vec{V}(\vec{X}) \quad (10.1)$$

where $[A]$ and $[B(\vec{X})]$ are the state global matrices of dimension $[n \times n]$, \vec{X} and $\vec{V}(\vec{X})$ are respectively the state vector and the boundary conditions vector with n components. This set of equations features nonlinearity since the matrix $[B(\vec{X})]$ and the boundary conditions vector $\vec{V}(\vec{X})$ are function of the state vector. The integration method to solve Equation 10.1 is the explicit 4th order Runge Kutta method. The nonlinear matrices and vectors are retrieved from the previous time step. This explicit method is generally used to solve none stiff problems with acceptable accuracy and minimal costs. However, when problems become increasingly stiff, characterized by a rapid change in one or more components of the solution, stability rather than accuracy becomes the dominant consideration, and implicit methods are the appropriate choice.

10.2 Eigenmodes and Stability Assessment

10.2.1 Linearization Procedure

Stability analysis of a hydroelectric system subjected to small perturbations is based on linearization of the nonlinear set of differential equations 10.1 around a solution point, see [59]. Then, stability is deduced from the eigenvalues of the linearized set of differential equations. Assuming $\vec{f} = [B(\vec{X})] \cdot \vec{X} - \vec{V}(\vec{X})$ a vector of n nonlinear functions, Equation 10.1 becomes:

$$[A] \cdot \frac{d\vec{X}}{dt} + \vec{f}(\vec{X}) = \vec{0} \quad (10.2)$$

Considering a small perturbation from the solution point \vec{X}_0 defined as:

$$\vec{X} = \vec{X}_0 + \delta\vec{X} \quad (10.3)$$

This new state vector must satisfy Equation 10.1:

$$[A] \cdot \left(\frac{d \cdot \vec{X}_0}{dt} + \frac{d \cdot \delta\vec{X}}{dt} \right) + \vec{f}(\vec{X}_0 + \delta\vec{X}) = \vec{0} \quad (10.4)$$

Using a first order Taylor development series, for $i = [1, n]$ it yields to:

$$A_{ij} \cdot \frac{d \cdot \delta X_{0j}}{dt} + f_i(\vec{X}_0) + A_{ij} \cdot \frac{d \cdot \delta X_j}{dt} + \sum_{j=1}^n \left(\left. \frac{\partial f_i}{\partial X_j} \right|_0 \cdot \delta X_j \right) = 0 \quad (10.5)$$

Since the equilibrium state vector satisfies Equation 10.1, we obtain the linearized system under matrix form as follow:

$$[A] \cdot \frac{d \cdot \delta\vec{X}}{dt} + [B_l] \cdot \delta\vec{X} = \vec{0} \quad (10.6)$$

where $B_{lij} = \left. \frac{\partial f_i}{\partial X_j} \right|_0$ is the linearized state global matrix. Regarding the viscoelastic pipe model, nonlinearity of the set of equations 7.6 is due to the resistances R_i which are proportional to the flow rate Q_i . By developing the product between the matrix $[B]$ and the state vector \vec{X} , the nonlinearity is due to the square exponent of the flow rate. Applying the linearization procedure developed above, it yields to:

$$\delta \left(R_i' \cdot Q_i^2 \right) = 2 \cdot R_i' \cdot Q_i|_0 \cdot \delta Q_i \quad (10.7)$$

where $Q_i|_0$ is the flow rate at the solution point and R_i' the reduced resistance defined by:

$$R_i' = \frac{\lambda \cdot dx}{2gDA^2} \quad (10.8)$$

Hence, the linearized state global matrix for the viscoelastic pipe model is:

$$[B_l]_{\text{ViscoPipe}} = \begin{bmatrix} 0 & -1 & 1 \\ 1 & R_i' \cdot Q_i|_0 + R_{ve} & -R_{ve} \\ -1 & -R_{ve} & R_{i+1}' \cdot Q_{i+1}|_0 + R_{ve} \end{bmatrix} \quad (10.9)$$

As for the Francis turbine runner model, the nonlinearity is due to the pressure source $H_t(Q_i, \omega, y)$ and the mechanical torque $T_t(Q_i, \omega, y)$ which are nonlinear functions of the flow rate, the rotational speed and the guide vane opening. In the same way as the viscoelastic pipe model, the resistance term of the Francis Turbine model induces a nonlinearity proportional to the square exponent of the flow rate. Therefore the linearization of this term is identical. On the other part, the linearization of the pressure source and the mechanical torque is given by:

$$\delta H_t = \left. \frac{\partial H_t}{\partial Q_i} \right|_0 \cdot \delta Q_i + \left. \frac{\partial H_t}{\partial \omega} \right|_0 \cdot \delta \omega + \left. \frac{\partial H_t}{\partial y} \right|_0 \cdot \delta y \quad (10.10)$$

$$\delta T_t = \left. \frac{\partial T_t}{\partial Q_i} \right|_0 \cdot \delta Q_i + \left. \frac{\partial T_t}{\partial \omega} \right|_0 \cdot \delta \omega + \left. \frac{\partial T_t}{\partial y} \right|_0 \cdot \delta y \quad (10.11)$$

where partial derivative terms are the gradients of the characteristic curves at the solution point. Hence, the linearized state global matrix is:

$$[B_l]_{\text{Runner}} = \begin{bmatrix} 2R'_t \cdot Q_i|_0 + \left. \frac{\partial H_t}{\partial Q_i} \right|_0 & \left. \frac{\partial H_t}{\partial \omega} \right|_0 \\ \left. \frac{\partial T_t}{\partial Q_i} \right|_0 & \left. \frac{\partial T_t}{\partial \omega} \right|_0 \end{bmatrix} \quad (10.12)$$

The gradients relative to the guide vane opening are not included in the linearized matrix system since the guide vane opening are not considered as a state variable in the set of Equations 7.3. However, if the Francis turbine is regulated by a speed controller for instance, then the guide vane opening becomes a state variable of the system and these gradients must be included in the linearized set of equations.

10.2.2 Eigenmodes Computation

Eigenmodes of the HA model are computed from the eigenvalues and eigenvectors of the linearized set of differential equations 10.6. By taking the Laplace transform with the Laplace operator $s = \alpha + j\varpi$ it yields to the state equations in the frequency domain:

$$(s \cdot [I] + [A]^{-1} \cdot [B_l]) \cdot \delta \vec{X}(s) = \delta \vec{X}(0) \quad (10.13)$$

To ensure a non trivial solution, the determinant of the global matrix $[M] = -[A]^{-1}[B_l]$ must be equal to zero:

$$\det(s \cdot [I] - [M]) = 0 \quad (10.14)$$

n roots are found and can be gathered in a vector \vec{s} where components $s_i = \alpha_i + j\varpi_i$ are system's eigenvalues. They can be either real or complex numbers. Since the global matrix $[M]$ is real in our present study, complex eigenvalues always occur in conjugate pairs $\{s_i, \bar{s}_i\}$. A real eigenvalue is a non oscillatory eigenmode whereas a complex eigenvalue is an oscillatory one. Dampings and angular frequencies of the HA model's eigenmodes are respectively given by the real part and the imaginary part of the eigenvalues. Moreover, for each eigenvalue s_i , an associated eigenvector is defined as:

$$[M] \cdot \vec{\Phi}_i = s_i \cdot \vec{\Phi}_i \quad (10.15)$$

Each eigenvector $\vec{\Phi}_i$ gives the eigenmode spatial shape corresponding to the state variables fluctuations in the whole HA model.

10.2.3 Stability Assessment

The stability assessment of the HA model is based on the response of the free oscillating system defined by the sum of all the eigenmodes contributions. Assuming l real eigenmodes the free oscillating response can be written as:

$$\delta \vec{X} = \sum_{i=1}^l \left(c_i \cdot \vec{\Phi}_i \cdot e^{s_i t} \right) + \sum_{i=l+1}^{(n-l)/2} \left(c_i \cdot \vec{\Phi}_i \cdot e^{s_i t} + \bar{c}_i \cdot \bar{\vec{\Phi}}_i \cdot e^{\bar{s}_i t} \right) \quad (10.16)$$

Therefore, if at least one of the eigenvalue has a positive real part, the system is unstable.

10.3 Lumped and Distributed Draft Tube Models

In this Section the effect of the spatial discretization of the draft tube model on the system eigenmodes computation is discussed. Indeed, the number of pressure nodes is decisive to capture the shape of the eigenmode which would be excited by the cavitating vortex rope. The onset of cavitation decreases dramatically the wave speed in the draft tube which defines the capacitance of the pressure nodes according to Equation 7.4. It has been shown in Section 7.3.3 that an equivalent capacitance C_{equ} must be considered when cavitation occurs:

$$C_{equ} = (1 - \beta) C_0 + C_c = \frac{gAdx}{a^2} \quad (10.17)$$

The decrease of the wave speed drives the eigenfrequencies of the hydraulic system. To illustrate this statement, the simplest hydraulic system including an upstream reservoir, a penstock feeding a Francis turbine operating at part load conditions with a cavitating helical vortex rope is considered. In Figure 10.1, the eigenfrequencies of the system are computed as function of the wave speed in the draft tube and comparison is made between lumped and distributed models.

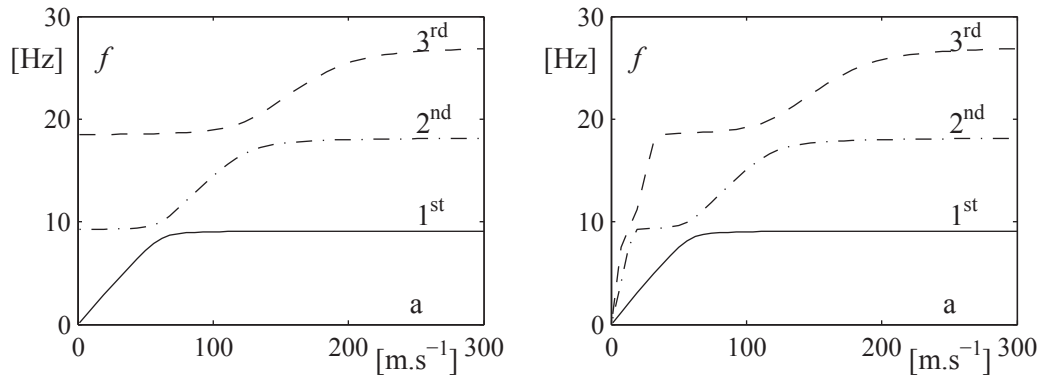


Figure 10.1: Eigenfrequencies as function of the wave speed in the lumped (left) and the distributed (right) draft tube models

For the distributed model a constant wave speed is considered for each pressure node. A major difference is observed between the lumped and the distributed models. In both cases, the eigenfrequency of each eigenmode decreases from a critical wave speed value. With the lumped model the eigenfrequency decreases once and saturates to a minimum value. However, with the distributed model, the eigenfrequencies are able to decrease twice and to reach very low values since no saturation is observed. Each decreasing phase corresponds to a deformation of the eigenmodes shapes, see Figure 10.2. The shape modification of the first and the second eigenmodes are plotted for three wave speed values. The x axis corresponds to the location in the one dimensional hydroacoustic system and the y axis is the pressure fluctuation amplitudes. The draft tube component (DT) where the wave speed is changed is located between $x/L = 0.965$ and $x/L = 1$. Regarding the first eigenmode, the decrease of the wave speed moves the maximum pressure fluctuation in the draft tube. The same behavior is observed between the lumped and the distributed

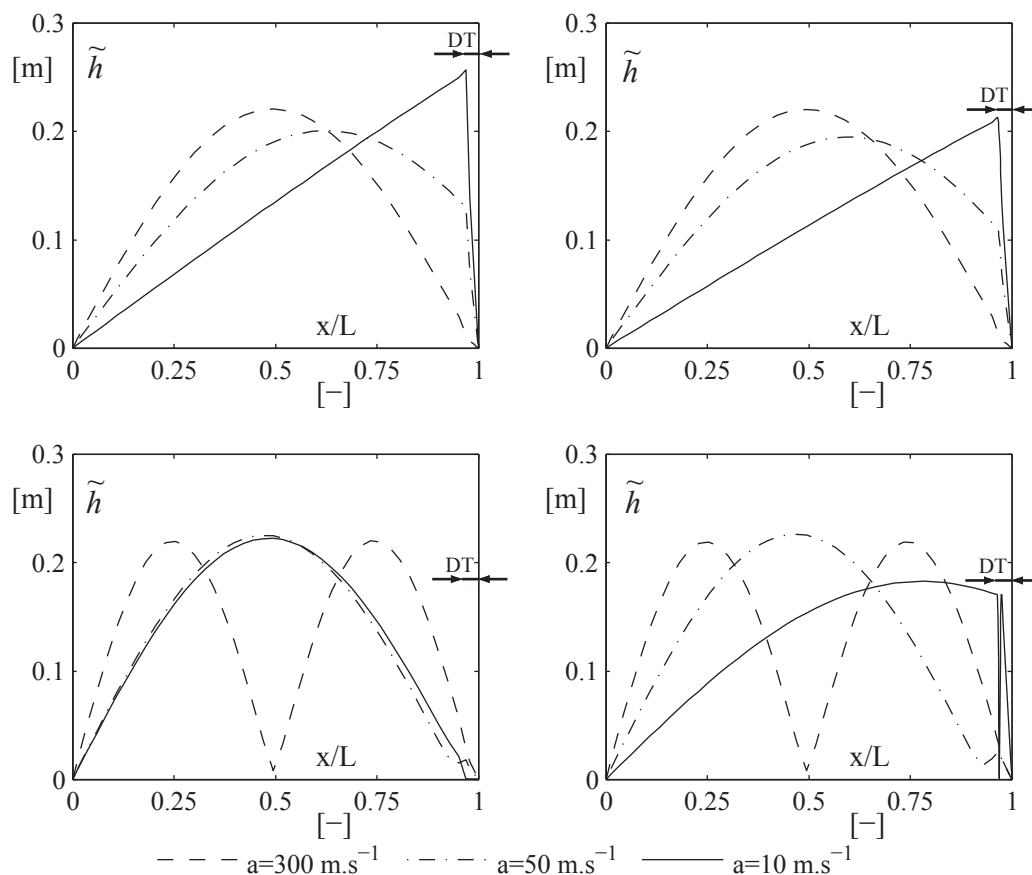


Figure 10.2: First (top) and second (bottom) eigenmode shape as function of the wave speed considering lumped (left) and distributed (right) draft tube models

model. However differences appear for the second eigenmode which features one pressure node between the two reservoirs. By decreasing the wave speed, the pressure node moves toward the draft tube location. This first deformation corresponds to the first decreasing phase of the eigenfrequency in Figure 10.1. The second decreasing phase of the eigenfrequency which is not observed with the lumped model corresponds to the displacement of the pressure node inside the draft tube as shown in Figure 10.3. Therefore, the choice between a lumped or a distributed model depends on the eigenmode which can be excited by the cavitating vortex rope. When high order eigenmodes are involved like for upper part load resonance, a distributed model must be chosen. However, when resonance or instability occurs with the first eigenmode, a lumped model is sufficient.

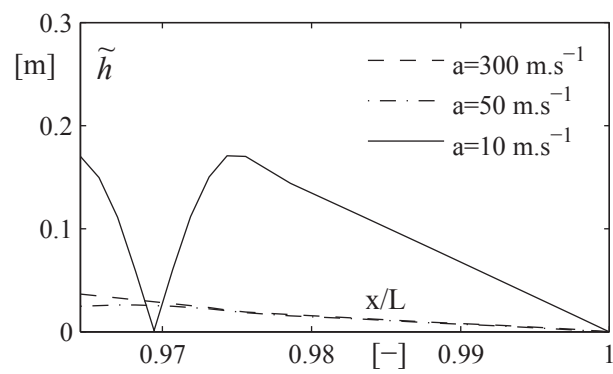


Figure 10.3: Second eigenmode shape in the distributed draft tube model as function of the wave speed

Part III

Part Load Operating Conditions

Chapter 11

Case Study

11.1 FLINDT project

In the framework of the FLINDT project [6], experimental and numerical investigations were carried out to achieve a better understanding of the flow pattern in a Francis draft tube. The selected Francis turbine runner features a high specific speed equal to $\nu = 0.56$ and corresponds to the scale model of a hydropower plant built in 1926 owned by ALCAN. The runner has 17 blades with an outlet diameter of 0.4 m. The original draft tube geometry is of Moody type and has been replaced for this research project by an elbow draft tube with one pier. This scale model was installed on the EPFL PF3 test rig. Among the several contributions, extensive wall pressure fluctuation measurements have been performed for different operating points under various Thoma number by Arpe [2]. In order to capture the helical vortex core precession phenomenon in the draft tube, 104 piezoresistive absolute pressure sensors installed in the draft tube wall are acquired with a HP-VXI acquisition system using a sampling frequency equal to sixteen times the runner frequency. The pressure field evolution, as function of the Thoma number is obtained in the whole draft tube. This experimental database allowed afterwards to validate unsteady CFD numerical simulations investigated at operating points out of resonance conditions with the hydraulic system, see Ciocan et al. [21] and Zobeiri [96].

11.2 Phenomenon of Interest

The phenomenon of interest is the upper part load resonance which was observed and measured by Arpe [2] at a low flow rate turbine operating point given in Table 11.1. Spectral analysis of the pressure fluctuations measured in the cone are presented as function of the Thoma number in Figure 11.1. For high Thoma number, the measured pressure

Table 11.1: Operating point conditions

φ/φ_{BEP}	ψ/ψ_{BEP}	N	GVO
[—]	[—]	[rpm]	[°]
0.703	1.06	750	16

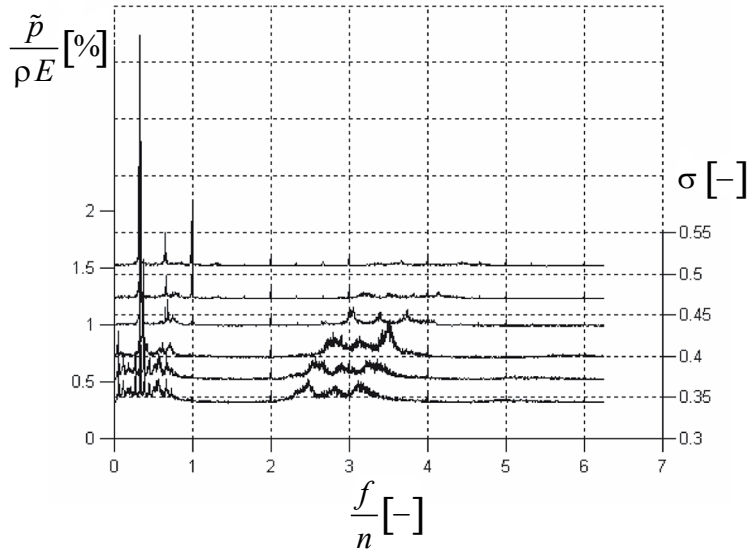


Figure 11.1: Influence of σ on pressure fluctuations in the draft tube cone [2]

fluctuations feature the helical precession frequency at 0.315 times the runner frequency n , called afterwards f_{rope} . Under these cavitation conditions, the excitation induced by the helical vortex rope does not lead to resonance phenomena. Unsteady CFD numerical simulations have been performed at these free cavitation conditions to find out this precession frequency, see Ciocan et al. [21] and Zobeiri [96]. However, by decreasing the Thoma number, pressure fluctuations between $2n$ and $4n$ appear and are modulated by the vortex rope precession. Therefore, three characteristic frequencies can be observed in this frequency range. Measurements of this phenomenon have been focused on the Thoma number value of $\sigma = 0.38$ where the modulated frequency is equal to $2.5n$ leading to pressure fluctuation amplitudes at $2.5n \pm f_{rope}$. During measurements, strong noise and vibration of the draft tube were reported. This phenomenon is called upper part load resonance, but can be encountered in literature without modulation as well [27]. The aim of this chapter is to be able to simulate this phenomenon combining a HD model of the vortex rope with a HA model of the hydraulic system including the draft tube region. Figure 11.2 shows the influence of the Thoma number on the two characteristic frequencies included in pressure fluctuations. The vortex precession frequency increases slightly by decreasing the Thoma number whereas the higher frequency decreases. Due to the dependence of the characteristic frequencies with the Thoma number, the occurrence of the resonance is very sensitive to the cavitation volume in the draft tube. For the specific cavitation conditions corresponding to a Thoma number value of $\sigma = 0.38$, where resonance occurred, amplitude spectra following four paths along the draft tube are presented in Figure 11.3. It can be noticed that pressure fluctuations related to the vortex rope precession and its harmonics are only located in the area of the draft tube cone and elbow, while pressure fluctuations at $2.5n$ are measured in the entire draft tube and in the turbine intake as well. These observations suggest that the precession frequency component is due to the local three dimensional flow in the draft tube whereas the component at $2.5n$ corresponds to a one dimensional hydroacoustic eigenmode of the hydraulic system responding to the vortex rope excitation. This assumption is confirmed by two comple-

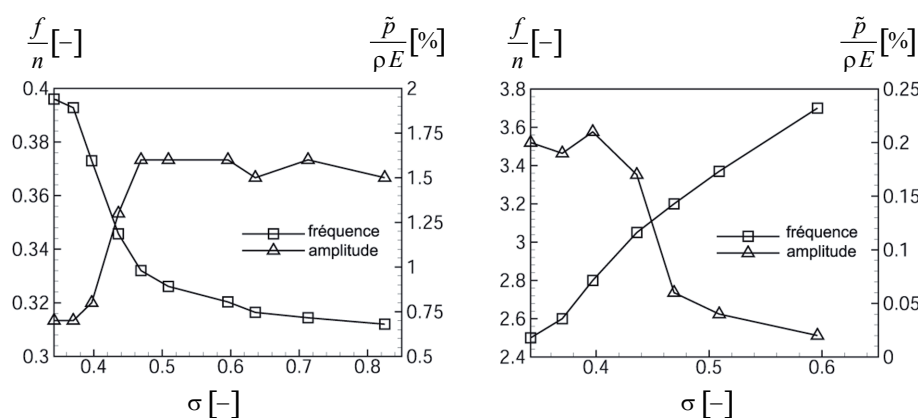


Figure 11.2: Influence of σ on the frequency and amplitude of pressure fluctuations for the vortex rope precession (left) and the higher frequency (right) [2]

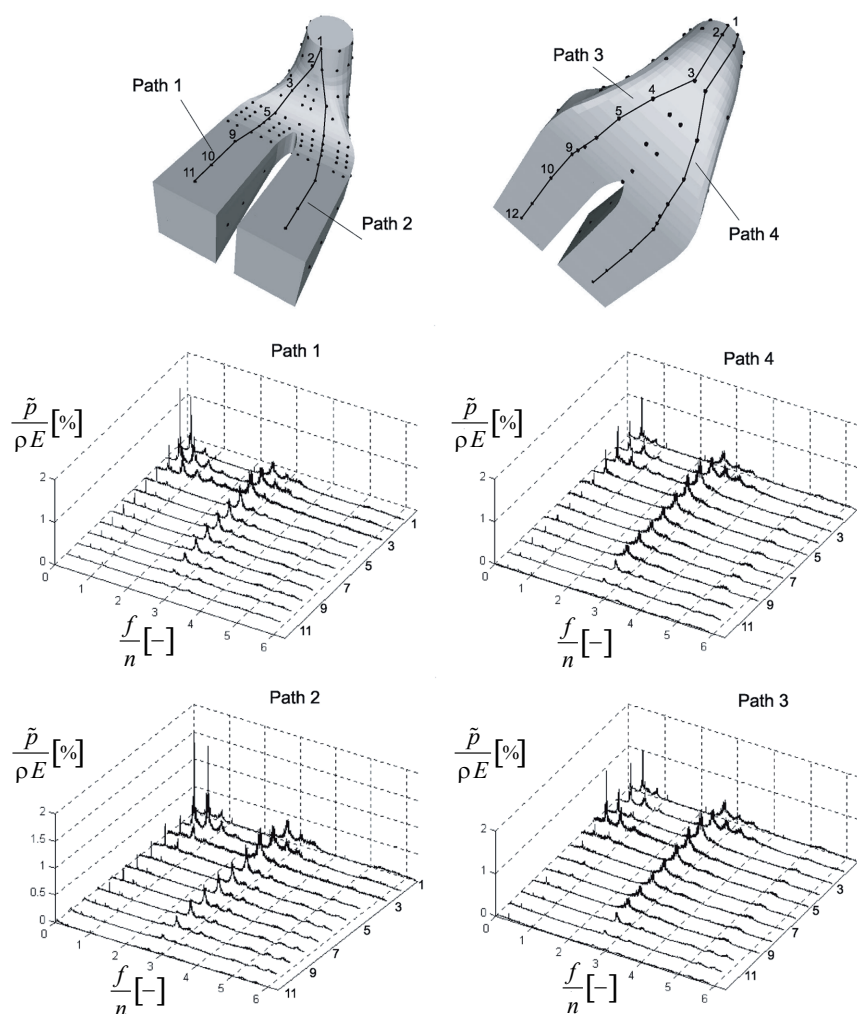


Figure 11.3: Amplitude spectra of pressure fluctuations along four paths for $\sigma = 0.38$ [2]

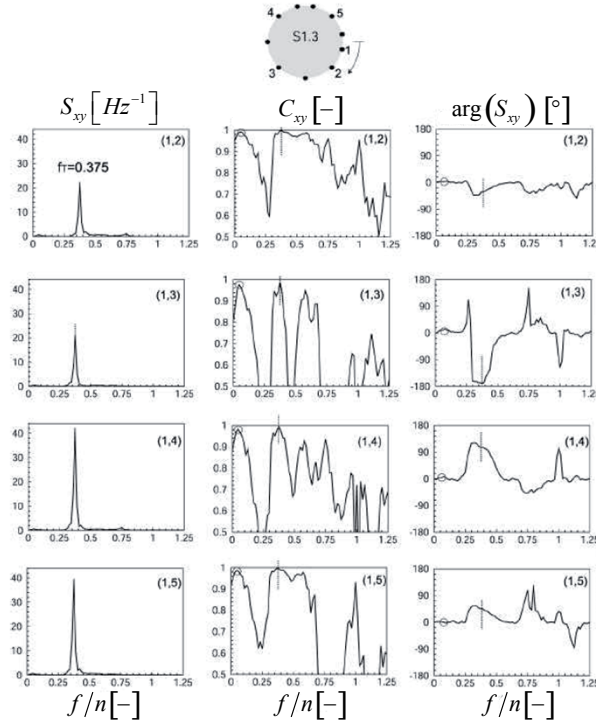


Figure 11.4: Phase shift analysis of pressure fluctuations in the cone at the vortex rope precession frequency [2]

mentary analysis. First, analysis of pressure fluctuations at the turbine intake where the precession frequency disappeared but not the higher frequency. Secondly, analysis of the phase shift computation of every pressure signals in the draft tube. In Figure 11.4, the phase shift at the precession frequency are computed for pressure sensors located in the same cone cross section. Pressure pulsations are phase shifted each other corresponding to the geometric angle location in the cone. This yields to the conclusion that the precession frequency component is due to the passage of the cavitating vortex core near the pressure sensor. The same analysis has been performed for the higher frequency component at $2.5n$ and results are presented in an unfolded draft tube representation in Figure 11.5. In the cone, no phase shift is experienced between pressure signals located in the same cross section. However, a phase shift of 150° is computed between the inlet and the outlet cone.

At this stage of the analysis, two assumptions about the nature of these high frequency synchronous pulsations can be made. The first one is that the longitudinal phase shift value of 150° corresponds to the time propagation of a 1D traveling wave in the draft tube [4]. The second one is that this phase shift is due to a 1D standing wave corresponding to an eigenmode of the hydraulic system featuring a pressure node in the cone [68]. In the both cases, the one dimensional property is lost in the elbow due to the curvature.

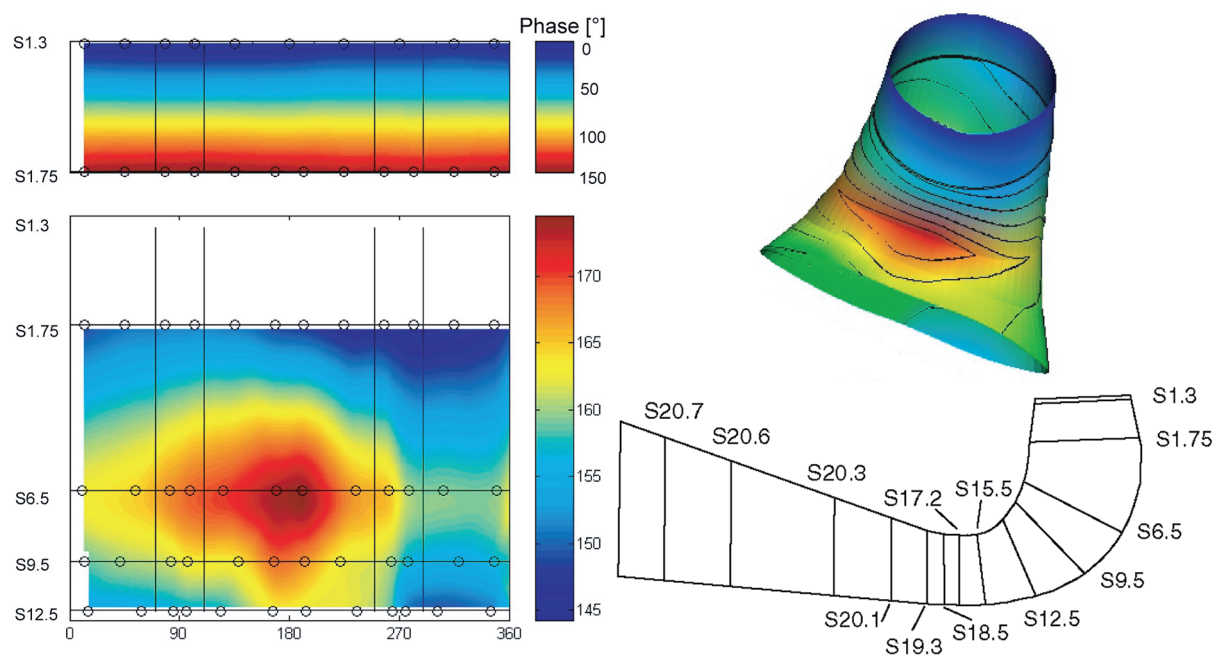


Figure 11.5: Phase shift analysis of pressure fluctuations in the draft tube at the high frequency component value of $2.5n$ [2]

11.3 Objectives

The objective is to predict and simulate this upper part load resonance by using both HD model of the vortex rope and HA model of the whole hydraulic system. The main task, described in Section 12.2, is to identify the HA draft tube model parameters from unsteady numerical simulations with the HD model. Through this section, the use of a cavitation model in the unsteady simulations to derive the HA parameters is discussed and the influence of the elbow on the HA parameters is highlighted. Then, a preliminary validation of the computed parameters will be achieved by comparing a one way simulation of a standard part load resonance with some experimental results reported in the literature. In Section 12.4, identification of the mechanism inducing upper part load resonance is described and then simulation of the upper part load resonance is performed. Finally, the effect of a two way simulation is compared to a one way simulation.

Chapter 12

Numerical Investigations

12.1 The 3D HD model

12.1.1 Setup

For the present application, ANSYS-CFX 12.0 version is used for the computation of the unsteady flow in the FLINDT reduced scale model draft tube. Unsteady Reynolds Average Navier-Stokes equations described in Chapter 8 are used. For single phase simulations (SPS), the set of equations is closed with the Scale Adaptative Simulation Shear Stress Transport (SAS-SST) which is a first order two equations turbulence model developed by Menter [64], whereas for two phase simulations (TPS), two turbulence models are compared: the SAS-SST model and the Shear Stress Transport (SST) model. As described in Section 7.3, the HA draft tube model is based on continuity and momentum balances performed respectively on continuity and momentum control volumes. Therefore, to derive the HA parameters, spatial discretization of the draft tube pipe in control volumes is required. In Figure 12.1, the principle of discretization is shown by comparing the CFD domain and the equivalent electrical scheme of the HA model. The continuity and the momentum balances correspond respectively in the electrical scheme to the node and the mesh equations. Hence, the proposed procedure to derive the HA parameters of the electrical scheme is to overlap continuity and momentum control volumes in the CFD domain. As a result, ten momentum and nine continuity control volumes are defined to describe the whole length of the draft tube including the two diffuser channels. The computational domain is constituted of the runner and the draft tube which is the best compromise between solution accuracy and computer resources, see Figure 12.2. The transient runner-draft tube simulation allows to predict the interaction of the flow between the upstream runner and the elbow draft tube [21], [96]. A General Grid Interface (GGI) is used between the two components, which interface position is updated for every time step. The computational domain is discretized with a structured mesh of 2.5 million nodes which 1 million for the draft tube component, carried out with ANSYS ICEM 12.0. The definition of the continuity and momentum control volumes is performed during the mesh generation. The resulting mesh and the corresponding momentum control volumes are shown in Figure 12.2. Taking into account this spatial discretization, the "High resolution" advection scheme is used to solve the set of equations. Regarding the time discretization a time step corresponding to 4° runner revolution is used with the "Second order backward euler" transient scheme. The number of coefficient loops

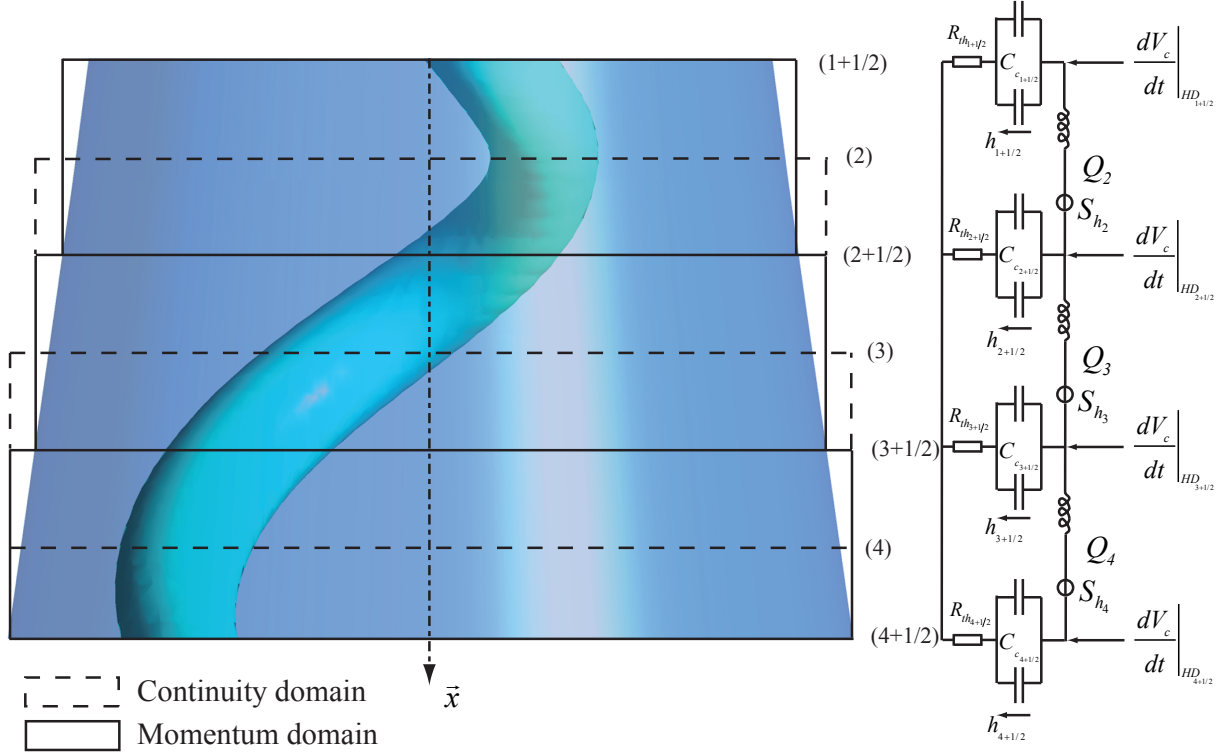


Figure 12.1: Principle of the computational domain discretization with respect to the HA model

is set to 3 and 30 respectively for single phase and two phase simulations with a rms convergence criterion of the residual specified to 10^{-4} . The influence of the time step and space discretization have been extensively studied by Zobeiri [96]. The boundary conditions are a prescribed velocity profile at the runner inlet and an opening condition with "static pressure for entrainment" at the draft tube outlet. To derive the velocity profile at the inlet, two preliminary steady state calculations were performed. First, steady flow computation in the spiral casing and the distributor is performed. Results are used as inlet conditions for a second steady flow computation in the stay vanes, guide vanes and runner assembly. For that case, inlet conditions for the unsteady computation is extracted at the runner inlet including turbulent kinetic energy and dissipation rate profiles. The investigated operating point is the one given in Table 11.1. The Thoma number allows to define the prescribed outlet pressure of the computational domain which is a decisive boundary condition for two phase simulation. From the Thoma number definition given in Equation 2.9 the flow and the energy coefficients $\varphi - \psi$ are introduced to derive the pressure at the diffuser outlet:

$$p_{\bar{I}} = \rho \cdot \psi \cdot \frac{U_{\bar{I}}^2}{2} \cdot \sigma + p_v + \rho g (Z_{ref} - Z_{\bar{I}}) - \rho \cdot \varphi^2 \cdot \frac{U_{\bar{I}}^2 \cdot A_{\bar{I}}^2}{2 \cdot A_{\bar{I}}^2} \quad (12.1)$$

As observed in Figure 12.2, the computational domain is extended to avoid flow recirculations at the outlet of the computational domain. Therefore, to deduce the outlet pressure, analytical formulations of head losses through this extension are used.

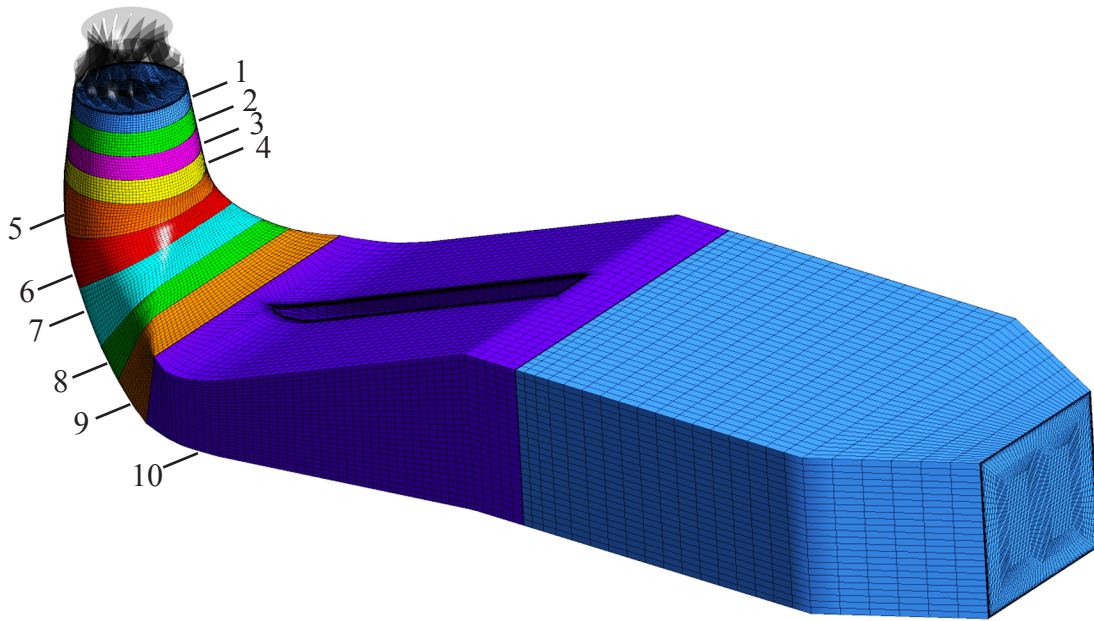


Figure 12.2: Grid mesh and corresponding momentum control volumes

12.1.2 Simulation Results

The cavitation volume of the vortex rope is a decisive quantity to derive the HA draft tube parameters. In the case of single phase simulations, the cavitation volume is assumed to correspond to the flow region bounded by the vapor pressure p_v set to 2338 Pa at 20°C. However, for two phase simulations, the state variable of the HD model called vapor volume fraction β is integrated over a specified volume on which the user wants to assess the cavitation volume V_c :

$$V_c = \int_V \beta dV \quad (12.2)$$

By applying the outlet pressure derived from Equation 12.1 corresponding to the investigated Thoma number of $\sigma = 0.38$, no cavitation volume can be observed contrary to experiments. Hence, a ratio is applied to the outlet pressure to fulfill two conditions. First, to get a cavitation volume qualitatively in agreement with experimental visualizations and then to obtain a vortex rope precession frequency matching with measurements. Indeed, for two phase simulations, the simulated vortex rope precession frequency depends on the Thoma number value as shown in Figure 12.3. This ratio can be formulated as function of the simulated and the experimental Thoma numbers as follows:

$$\frac{\sigma_{sim}}{\sigma_{exp}} = 0.59 \quad (12.3)$$

Afterwards, the subscript *sim* will be omitted. In Figure 12.3 the vortex rope precession frequency obtained by numerical simulation is plotted as function of the corrected Thoma number. For single phase simulation (SPS) the frequency is constant and equal to $0.32n$

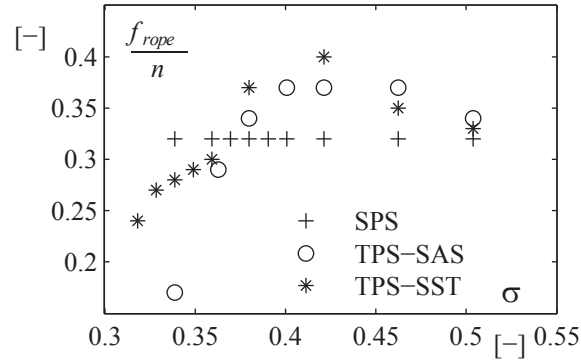


Figure 12.3: Evolution of the vortex rope frequency as function of σ

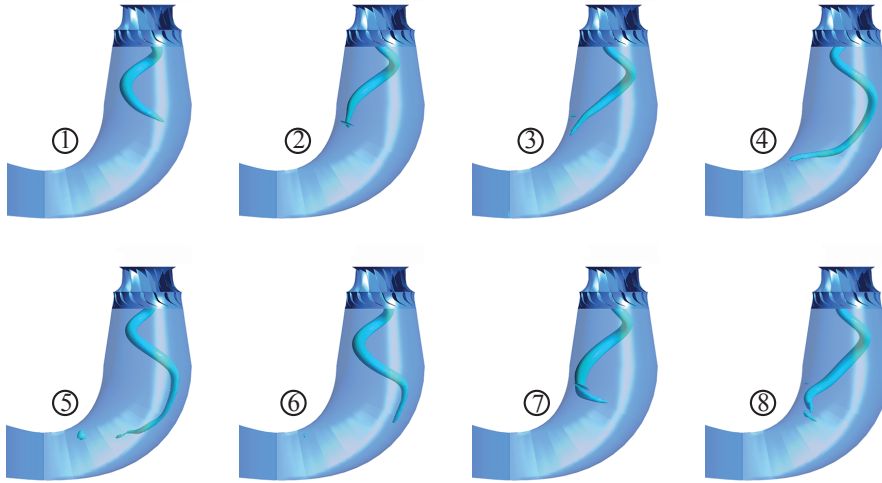


Figure 12.4: Single phase simulation (SPS) of the vortex rope precession

whereas for two phase simulations (TPS) the frequency is influenced by the Thoma number. At the investigated cavitation conditions corresponding to a Thoma number value of 0.38, the precession frequency is respectively equal to $0.34n$ and $0.37n$ for the two phase simulations with SAS-SST and SST turbulence models. When cavitation occurs in the vortex core, the precession frequency is higher than the cavitation free case which is in good agreement with experimental measurements, see Figure 11.2. Regarding the two phase simulation with the SAS-SST turbulence model, the frequency obtained for high σ values tends to the case of computation without cavitation model. Moreover, by decreasing the σ value, frequency increases slightly up to a critical σ value for which the frequency decreases dramatically. The slope of this decreasing is higher for the SAS-SST model than the SST model.

In Figure 12.4 the vortex rope precession obtained with single phase simulation is shown at different time steps. The cavitation volume experiences volume fluctuations. At each vortex rope revolution, the inner part of the draft tube elbow is in contact with the vortex rope's tip. This contact induces the increase of the vortex rope's length in the direction of the elbow outlet. Then its length decreases to experience the same dynamic



Figure 12.5: Two phase simulation (TPS) of the vortex rope precession with the SAS-SST turbulence model

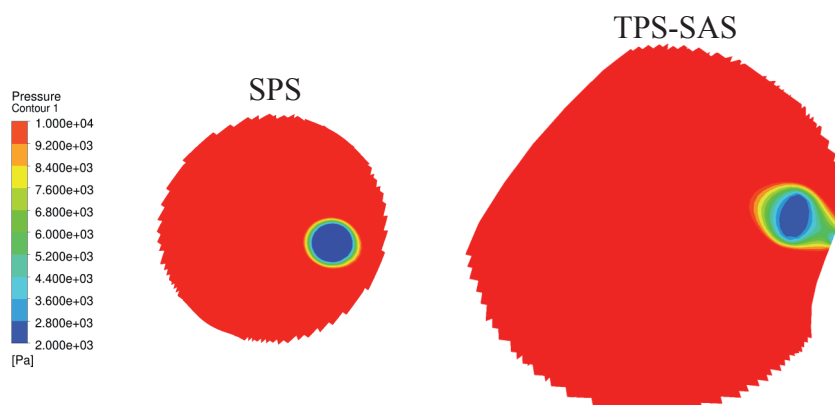


Figure 12.6: Comparison of the vortex rope cross section between single phase and two phase simulations

behavior for the next revolution.

In Figure 12.5 the vortex rope precession obtained with two phase simulation is shown at different time steps. For this illustration, results from the SAS-SST model is used. Despite of the same prescribed outlet pressure than the case illustrated in Figure 12.4, the vortex rope cross section is smaller and features an elliptical cross section as shown in Figure 12.6 by contour pressure levels. Moreover, the cavitation volume fluctuation is more unsteady in the case of two phase simulations. Just below the runner, the pitch of the helical vortex rope may reduces, as shown at the time step 3 of Figure 12.5, up to make a node shown in the time step 4. After this, the core of the vortex rope disappears to be recreated for the next revolution. This phenomenon does not appear at each vortex rope revolution. One can deduce that the cavitation volume either in single phase or two phase simulations is unsteady. In Figure 12.7, the time average of the fluctuating cavitation volume \bar{V}_c is computed for several Thoma numbers over a time simulation

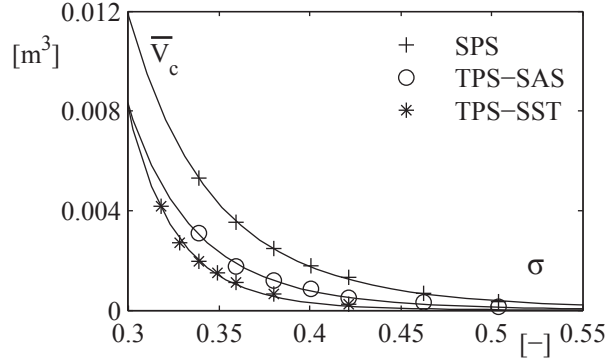


Figure 12.7: Evolution of the time averaged cavitation volume as function of σ

Table 12.1: Curve fitting of the time averaged cavitation volume with the Thoma number

Simulation	a	b	Fitting coefficient
SPS	$3.98 \cdot 10^{-6}$	-6.65	0.9994
TPS-SAS	$4.49 \cdot 10^{-7}$	-8.15	0.995
TPS-SST	$9.34 \cdot 10^{-9}$	-11.35	0.9945

corresponding to 60 runner revolutions. The time averaged cavitation volume is function of the Thoma number according to a power law defined as follows:

$$\bar{V}_c = a\sigma^b \quad (12.4)$$

Using curve fitting, the relations, given in Table 12.1, are established between the Thoma number and the time averaged cavitation volume. For a given Thoma number, the cavitation volume determined by the iso pressure p_v level, is higher in the case of single phase simulation. When cavitation model is used, the cavitation volume is lower and a slight difference can be observed between the SAS-SST and SST turbulence models.

12.2 Identification of HA Draft Tube Model Parameters

12.2.1 Momentum Source

The identification of the excitation source induced by a complex turbulent flow has been extensively used for aeroacoustic applications. In the first aeroacoustic theory by Lighthill in 1952 [62], sound is generated by unsteady flows through the nonlinear interaction of velocity fluctuations, entropy fluctuations, as well as viscous stress. Alternative but still exact formulations, Howe [47] and Powell [78] emphasize the role of vorticity as sound sources. The notion of "acoustic analogy" refers to the idea of representing a complex fluid mechanism process that acts as an acoustic source by an acoustically equivalent source term. The first and most well-known analogy was derived by Lighthill without approximation in the Navier-Stokes equations. A flow solution q , defined as vector of velocities

and thermodynamic variables, satisfies the Navier-Stokes equations $N(q) = 0$. Since part of q is source of sound, the Lighthill analogy is formulated by rearranging $N(q) = 0$ into $Lq = S(q)$, where L is a linear wave propagation operator and $S(q)$ is the nonlinear sound source. Even if the resulting Lighthill's wave equation is considered for the case of a limited source region embedded in an infinite uniform stagnant fluid, the formulation of the source term $S(q)$ is used in this Section to characterize the hydroacoustic sources contained in the draft tube flow. Then, a comparison of this Lighthill source term with the momentum sources S_h related to the forces induced by the flow on the draft tube wall is performed.

By taking the time derivative of the mass conservation law and the divergence of the momentum conservation law, it yields to the famous $L - S$ decomposition called Lighthill analogy:

$$\frac{\partial^2 \rho'}{\partial t^2} - a^2 \frac{\partial^2 \rho'}{\partial x_i^2} = \frac{\partial^2 T_{ij}}{\partial x_i \partial x_j} \quad (12.5)$$

where ρ' and a are respectively the density fluctuations from reference state and the wave speed defining a linear homogeneous medium scalar wave operator L which acts on the density. The excitation source induced by the turbulent flow is considered into S defined as the double divergence of the Lighthill stress tensor T_{ij} :

$$T_{ij} = \rho C_i C_j - \sigma_{ij} - a^2 \rho' \delta_{ij} \quad (12.6)$$

This double divergence in the right hand side of Equation 12.5 is the acoustic source term resulting from three basic acoustic processes. First the nonlinear convective forces described by the Reynolds stress tensor $\rho C_i C_j$. Then pressure and viscous forces described by the stress tensor $\sigma_{ij} = -p\delta_{ij} + \tau_{ij}$ and finally a deviation from an isentropic behavior $a^2 \rho' \delta_{ij}$. One can notice that in the case of incompressible flow simulations, the last contribution can not be considered. It is proposed in this Section to compare the momentum sources S_h with the source term in the right hand side of Equation 12.5 averaged on the momentum control volumes:

$$S = \frac{1}{V} \int_V \frac{\partial^2 T_{ij}}{\partial x_i \partial x_j} dV \quad (12.7)$$

Since the HA draft tube model is based on continuity and momentum equations, the momentum sources S_h are considered in the HA modeling instead of the volume averaged Lighthill source term which formulation is more adapted for wave equations. The Lighthill source term is computed only for single phase simulations with the help of additional variables in the ANSYS CFX 12.0 setup simulation. The double divergence of the Lighthill stress tensor T_{ij} is a scalar which is computed for each node of the grid mesh as it is shown in Figure 12.8. This source term is a scalar field available as the same way as the pressure in a post processing step in the whole computational domain.

Momentum source identification in single phase simulations (SPS)

Although the Thoma number does not influence the identification of the momentum source in a single phase simulation, its value is set up at 0.38 corresponding to the cavitation

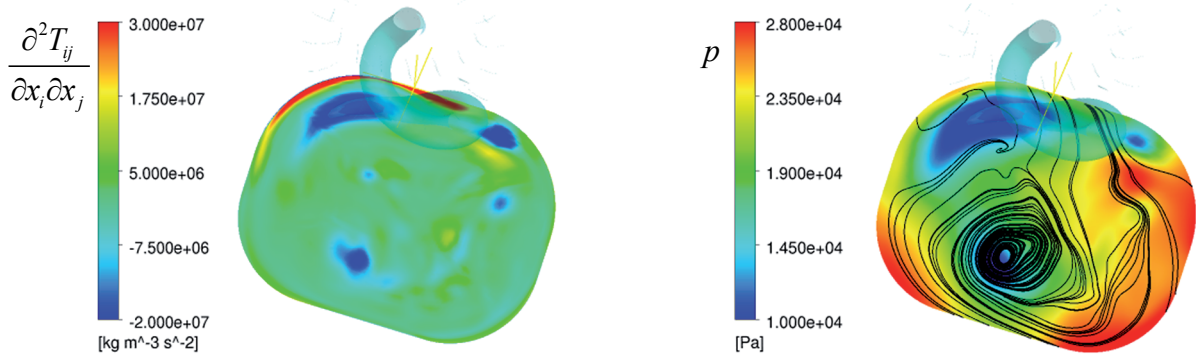


Figure 12.8: Visualization of the Lighthill source term (left) and the pressure (right) fields in an elbow cross section

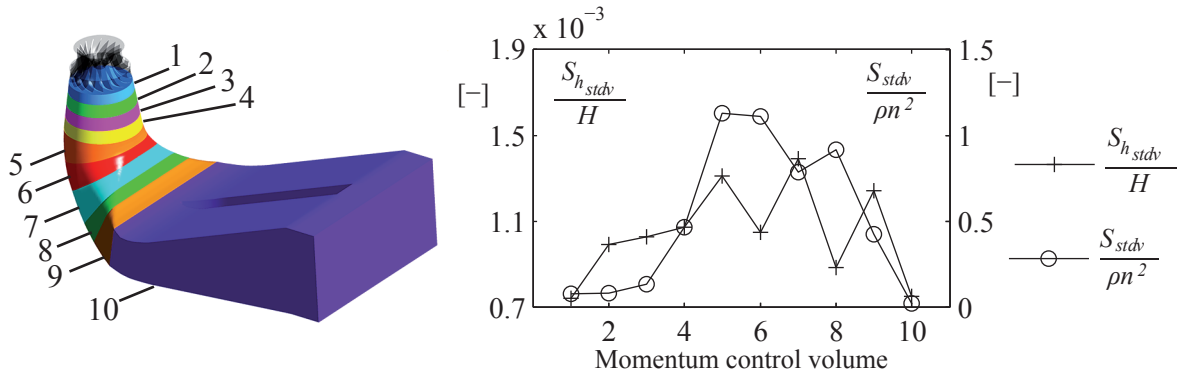


Figure 12.9: Standard deviations of the momentum sources S_h and the volume averaged Lighthill source term S as function of the location in the draft tube domain

conditions investigated during measurements, see Section 11.2. In Figure 12.9, standard deviations of the momentum sources S_h (defined by Equation 7.25) and the volume averaged Lighthill source term S (defined by Equation 12.7) are compared in each momentum control volume. These two terms are respectively normalized by the turbine head H and the quantity ρn^2 . The volume averaged Lighthill source term features a high intensity in the elbow draft tube contrary to the cone where intensity is very low. In comparison, the momentum sources derived from the forces feature the same evolution in the draft tube domain. The complex three dimensional flow in the elbow induces a HA source able to excite the connected hydraulic system.

The characteristic frequencies of the momentum sources S_h and the volume averaged of the Lighthill source term S , are compared in Figure 12.10. The two terms feature a fundamental frequency value of $0.32n$ corresponding to the vortex rope precession frequency. Regarding the harmonic components, the first five are contained in the time signal of the volume averaged Lighthill source term S whereas only the first three harmonics are available in the momentum source S_h .

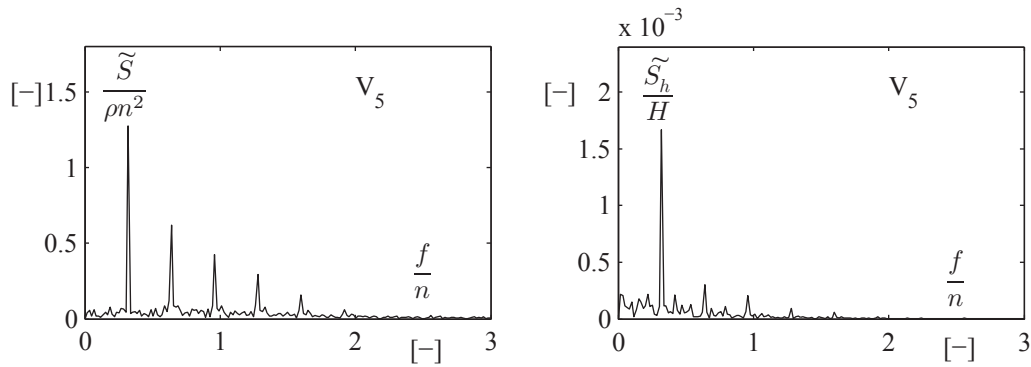


Figure 12.10: Comparison of amplitude spectra between the momentum source S_h and the volume averaged Lighthill source term S in the momentum control volume V_5 located in the elbow

The similitude between the amplitude spectra and the evolution of the standard deviation in the draft tube domain lead to the conclusion that the total force induced by the precessing vortex rope is the physical parameter to use in order to identify the momentum source contained in the elbow draft tube.

In Figure 12.11 amplitude spectra of the two terms are plotted in a waterfall diagram for each momentum control volume. The waterfall diagram of the Lighthill source term emphasizes the influence of the elbow on the excitation source generation. Indeed, in the first three momentum control volumes corresponding to the cone location, spectra of the Lighthill source term fluctuations do not feature any energy. However, momentum source fluctuations are experienced in the cone contrary to the Lighthill source term but with a lower intensity than in the elbow. According to Equation 7.25, these momentum sources are related to the forces induced by the fluid motion on the draft tube wall. Hence, the cone being a divergent, the fluid motion induces obviously an axial force. The excitation source is added to this force which explains why the intensity of the momentum sources increases in the elbow.

In Figure 12.12 the phases of the momentum sources fluctuations are analyzed between the different momentum control volumes along the draft tube. The first momentum control volume just under the runner is taken as reference to compute the phases with the help of the spectral density S_{xy} and the coherence function C_{xy} . The analysis between the first and the third or the first and the fifth momentum control volumes show that the fundamental frequency and the first harmonic are highlighted by the spectral density with a maximum energy transfer given by the coherence. However, regarding the analysis between the first and ninth momentum control volumes less coherence is observed. The argument of the spectral density corresponding to the last column in Figure 12.12 gives the phase for each frequency between the momentum sources in the different momentum control volumes. One can observe that the momentum sources are in phase in the cone between the first and the third momentum control volumes. In Figure 12.13 time history of momentum sources in the momentum control volumes located in the cone are plotted to confirm this observation.

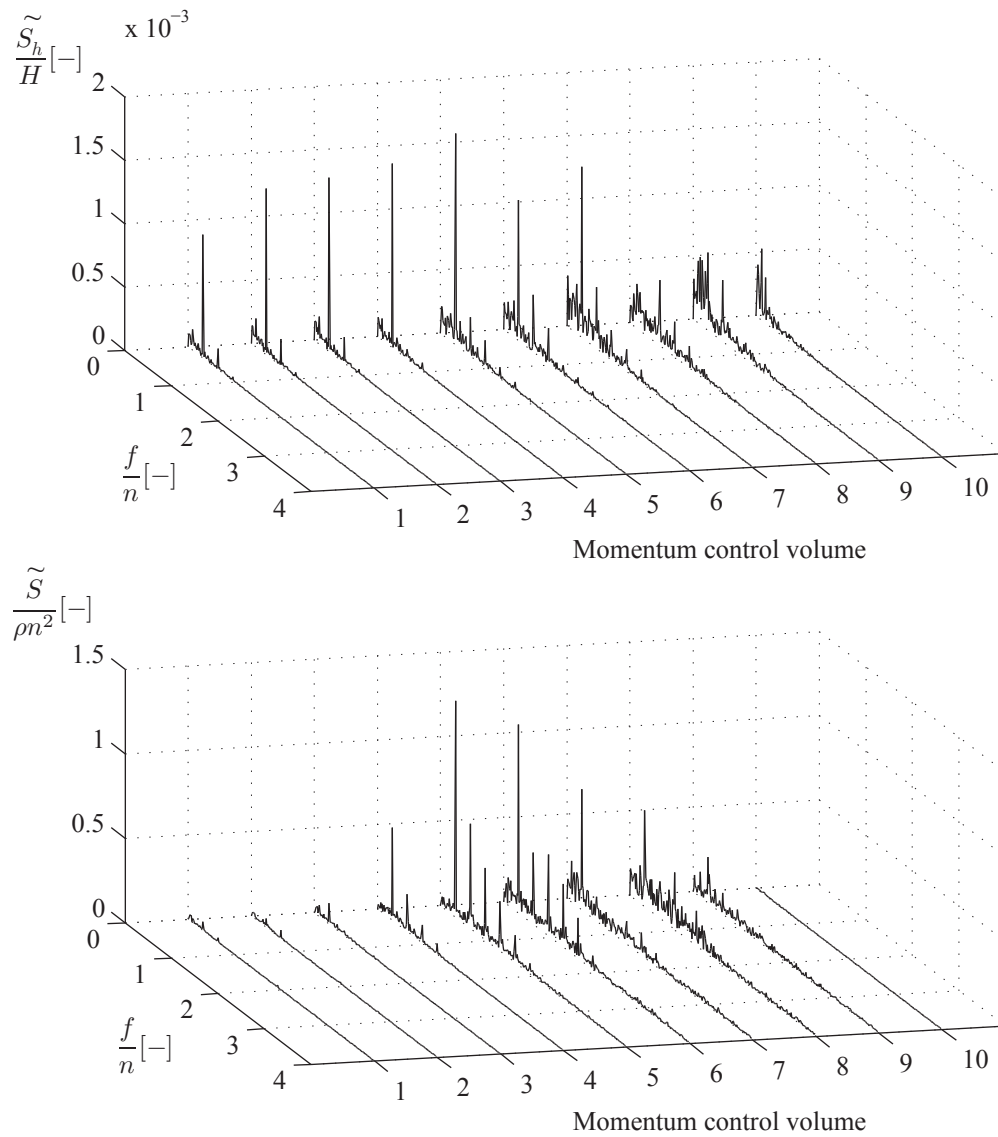


Figure 12.11: Waterfall diagram of the amplitude spectra of the momentum sources S_h (Top) and the volume averaged Lighthill source term S (Bottom) in the momentum control volumes

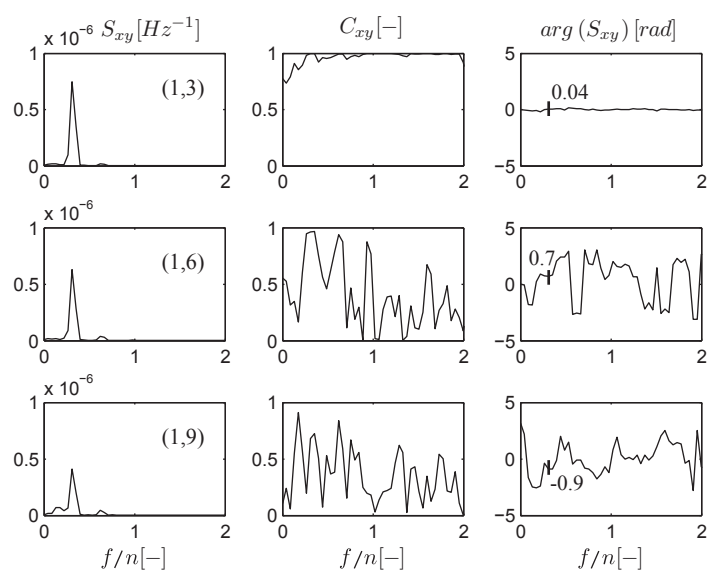


Figure 12.12: Phase analysis of momentum sources between the momentum control volumes

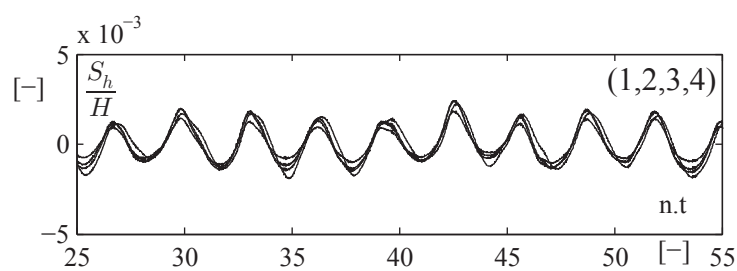


Figure 12.13: Time history of momentum sources fluctuations experienced in the first four momentum control volumes located in the cone

Momentum source identification in two phase simulations (TPS)

In a two phase simulation, the assessment of the Lighthill source term is quite complicated to compute and has not been investigated in this present work. It is proposed in this Section to compare the identification of the momentum sources S_h between two phase and single phase simulations at the investigated Thoma number value of 0.38. It has been already shown in Figure 12.3 that the excitation frequency is increased if a two phase simulation is carried out. Moreover, in Figure 12.14, the standard deviation is compared along the draft tube domain between single phase and two phase simulations. It is shown that in all the cases, the intensity features a maximum in the elbow region of

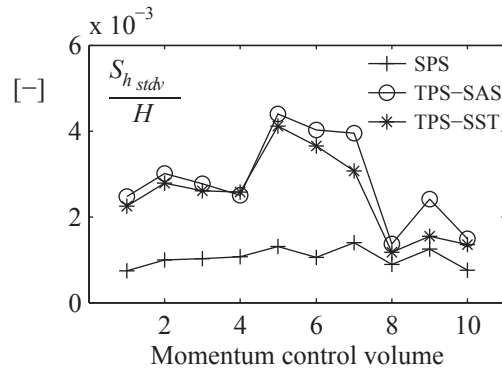


Figure 12.14: Comparison of the standard deviations of the momentum sources S_h between single phase and two phase simulations as function of the location in the draft tube domain

the draft tube and is much higher when two phase flow simulations are considered. Figure 12.15 compares the amplitude spectra of the momentum source fluctuations in the elbow between single phase and two phase simulations with the SAS-SST turbulence model. As expected, the fundamental frequency is changed from $0.32n$ to $0.34n$. However, harmonics are lost and the quantity features more energy in a broad band frequency range in the case of a two phase simulation.

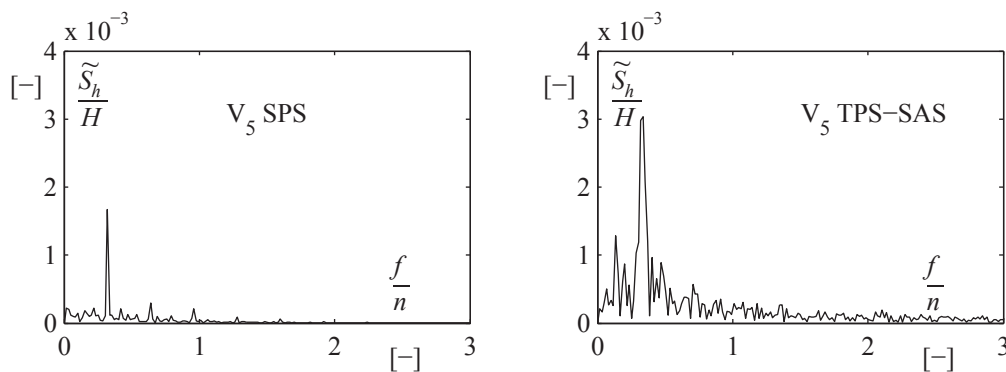


Figure 12.15: Comparison of the momentum source amplitude spectra in the fifth momentum control volume between single phase (left) and two phase (right) simulations

Influence of the Thoma number

It has been shown in Figure 12.3 that the Thoma number has an influence on the momentum sources frequencies. The same behavior can be observed on the intensity of the momentum source. To visualize this effect, for each Thoma number, the discretized momentum sources derived in each momentum control volumes are added to lead to a global momentum source. Then standard deviation of this global momentum source is computed and plotted as function of the Thoma number in Figure 12.16. As expected, the inten-

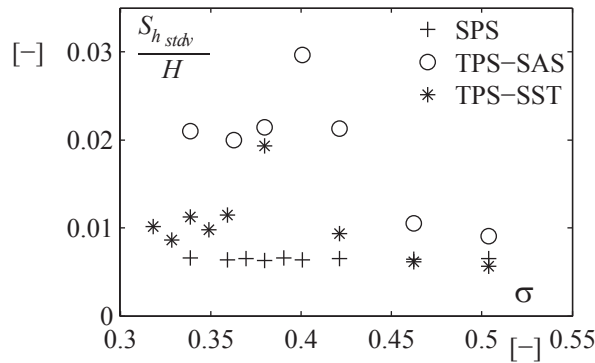


Figure 12.16: Evolution of the standard deviation of the global momentum source as function of the Thoma number

sity of the global momentum source is unchanged by the Thoma number for single phase simulation. However, in the case of a two phase simulation, the intensity changes and features a maximum as observed in Figure 12.16. It can be noticed that for high Thoma number, the global source intensity tends to an intensity equal to the one obtained with a single phase simulation.

12.2.2 Mass Source

As explained in Section 7.3.3, the mass source S_Q defined by Equation 7.17, can be split in a part due to the hydroacoustic field $S_{Q_{HA}}$ and another one due to the hydrodynamic incompressible fluid motion $S_{Q_{HD}}$:

$$S_Q = S_{Q_{HA}} + S_{Q_{HD}} \quad (12.8)$$

Considering a one way simulation, the hydroacoustic part $S_{Q_{HA}}$ is modeled through the equivalent capacitance C_{equ} and the hydrodynamic part $S_{Q_{HD}}$ is derived from unsteady simulations performed with the HD model in each continuity control volume. By convenience, this hydrodynamic part due to the unsteadiness of the hydrodynamic field is called afterwards mass source. The computation of the HA part is treated in details in Section 12.2.3 and the computation of the hydrodynamic part uses a central finite difference approximation of the cavitation volume time derivative. As described in Section 12.1.1, continuity control volumes are overlapped with the momentum control volumes, see Figure 12.1. Therefore only 9 continuity control volumes are available contrary to 10 for the momentum control volumes. As a first step the analysis of these mass sources

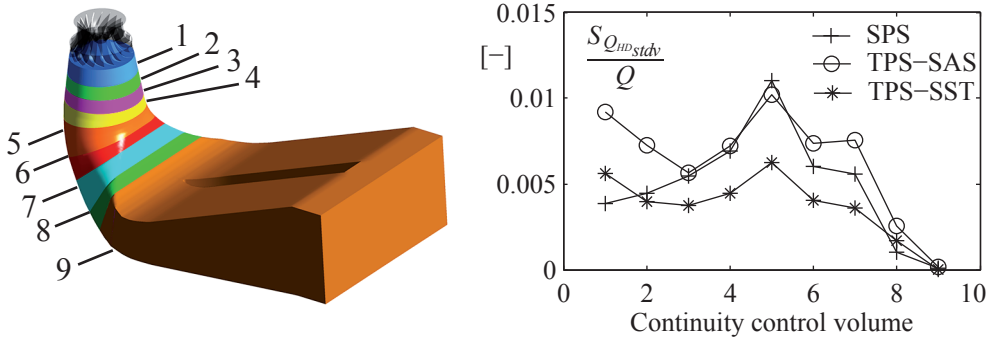


Figure 12.17: Standard deviations of the mass sources $S_{Q_{HD}}$ as function of the location in the draft tube domain

is carried out for the investigated Thoma number of 0.38. In Figure 12.17, standard deviation of the mass sources normalized by the flow rate Q of the investigated operating point, are plotted as function of the continuity control volume considered. The mass sources computed in single phase and two phase simulations are compared. In all the cases, a maximum of intensity is observed in the elbow at the fifth continuity control volume. However a difference between single phase and two phase simulations is observed in the first continuity control volumes under the runner where the intensity variation as function of the continuity control volume is the inverse. The characteristic frequencies components of these mass sources are analyzed by computing amplitude spectra as it is shown for the fifth continuity control volume in Figure 12.18. The fundamental fre-

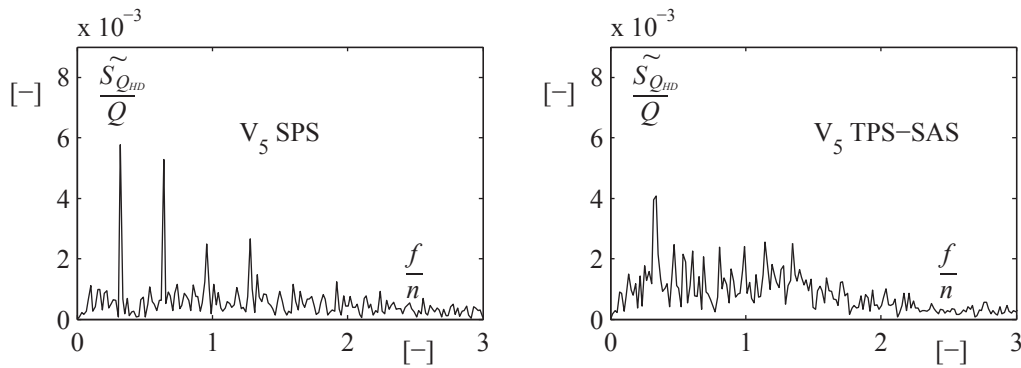


Figure 12.18: Comparison of the mass source amplitude spectra in the fifth continuity control volume between single phase (left) and two phase (right) simulations

quencies of these mass sources corresponding to the cavitation volume fluctuation due to the hydrodynamic field in the draft tube correspond to the frequencies found for the momentum sources: $0.32n$, $0.34n$ and $0.37n$ respectively for single phase and two phase simulations with the SAS-SST and SST turbulence models. In the fifth continuity control volume, the harmonics are contained in the time signal in single phase simulation whereas harmonics are less pronounced in the two phase simulation since the amplitude spectrum features more energy in a broad band frequency range. Finally, the influence of the Thoma

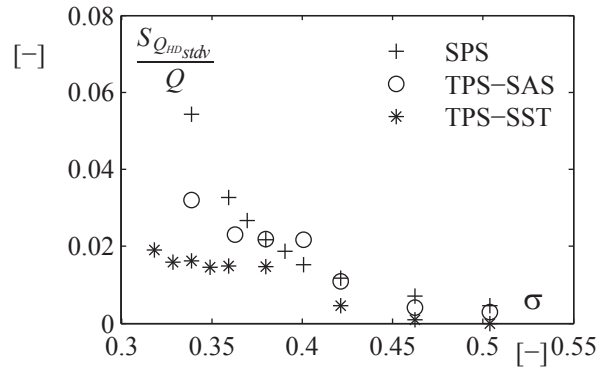


Figure 12.19: Evolution of the standard deviation of the global mass source as function of the Thoma number

number on the mass source intensity is investigated by computing a global mass source corresponding to the time derivative of the total cavitation volume which is the sum of the cavitation volume contained in each continuity control volume. The standard deviation of this global mass source is computed and plotted as function of the Thoma number in Figure 12.19. Comparison of the global mass source intensity as function of the Thoma number between single phase and two phase simulations is performed. In all the cases, the lower is the Thoma number, the higher is the intensity. However a saturation is observed for two phase simulations when low Thoma numbers are reached.

12.2.3 Cavitation Compliance

Two methodologies are proposed to compute the cavitation compliance parameter. Usually, in the literature, the cavitation compliance is computed for a lumped HA model shown in Figure 7.8 from the following equation:

$$C_c = -\frac{\partial V_c}{\partial h_{\bar{i}+1/2}} \quad (12.9)$$

Dörfler [25] computed experimentally this parameter by evaluating the variation of the cavitation volume as function of the Thoma number which corresponds to variation of a mean pressure level in the draft tube. In this Section, this methodology called afterwards "derivative method" will be employed with the help of numerical simulations with the HD model by considering a variation of the outlet pressure of the draft tube domain which is similar to a variation of the Thoma number. Therefore the cavitation compliance can be rewritten as function of the Thoma number as follows:

$$C_c = -\frac{\partial V_c}{\partial h_{\bar{i}+1/2}} \approx -\frac{\partial V_c}{\partial h_{\bar{i}}} = -\frac{1}{H} \frac{\partial V_c}{\partial \sigma} \quad (12.10)$$

To derive the corresponding wave speed, the definition of the equivalent capacitance given by Equation 10.17 is used. One can notice that this parameter takes into account compliances of the wall, the liquid phase and the cavitation. On the other side, a second methodology is compared by evaluating first the wave speed in the draft tube domain

from an analytical model. Then the equivalent compliance is computed from Equation 7.4. This methodology is called afterwards "analytical method". Many formulations can be found in the literature for the computation of the wave speed in a cavitating flow. The one which has been selected is the one developed by Rath [80]:

$$a = \left[\left(\beta \rho_c \frac{p}{p_0} + (1 - \beta) \rho \left(1 + \frac{1}{E_l} (p - p_0) \right) \right) \cdot \left(\frac{\beta}{p} + \frac{1 - \beta}{E_l} + \frac{D}{e \cdot E_{wall}} \right) \right]^{-\frac{1}{2}} \quad (12.11)$$

with:

- ρ_c the density of the water vapor,
- ρ the density of the liquid phase,
- β the cavitation volume fraction,
- E_l the bulk modulus of the liquid phase,
- E_{wall} the young modulus of the pipe wall,
- D the pipe diameter,
- e the thickness of the pipe wall.

As shown in Section 10.3, the spatial discretization of the HA draft tube model depends on the eigenmode order involved in the resonance simulation. When the resonance occurs with a low order eigenmode, a lumped HA model is sufficient to simulate the pressure fluctuations in the whole hydraulic system. However, when high order eigenmodes are involved, a distributed model must be chosen. The identification of the cavitation compliance is presented in this Section for both lumped and distributed models. Moreover, comparison of the two methodologies is available.

Cavitation compliance identification for a lumped HA model

The first step of the "derivative method" to derive the cavitation compliance for a lumped HA model is to compute the time history of the total cavitation volume for different Thoma numbers. Then, the time averaged value is computed and can be plotted as function of the Thoma number, see Figure 12.7. As described in Section 12.1.2, the data are fitted with a power law which coefficients are given in Table 12.1. Then, the derivative of the fitted curve is computed to derive the cavitation compliance C_c and therefore the equivalent compliance according to Equation 10.17. Finally, relations between the cavitation volume and the equivalent capacitance or the corresponding wave speed are obtained and plotted in Figure 12.20. A comparison of these look up tables between single phase and two phase simulations is shown. One can notice that the numerical simulations investigated at different Thoma numbers and the computation of the look up tables are performed at a pre-processing step. Hence, a relation can be established at each time step of the simulation between the total cavitation volume obtained with the HD model, and the equivalent capacitance of the HA model.

Regarding the "analytical method", the aim is to compute from Equation 12.11 the wave speed at each time step of a numerical simulation of the cavitating vortex rope with

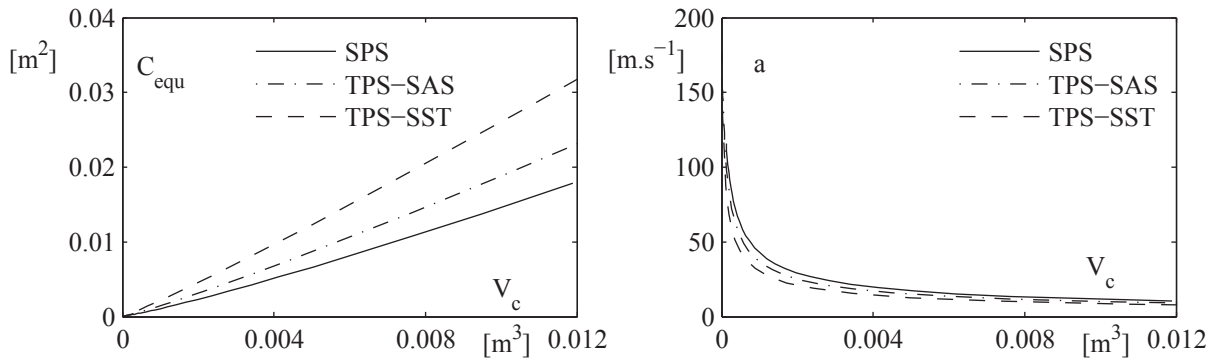


Figure 12.20: Equivalent compliance (left) and wave speed (right) as function of the cavitation volume

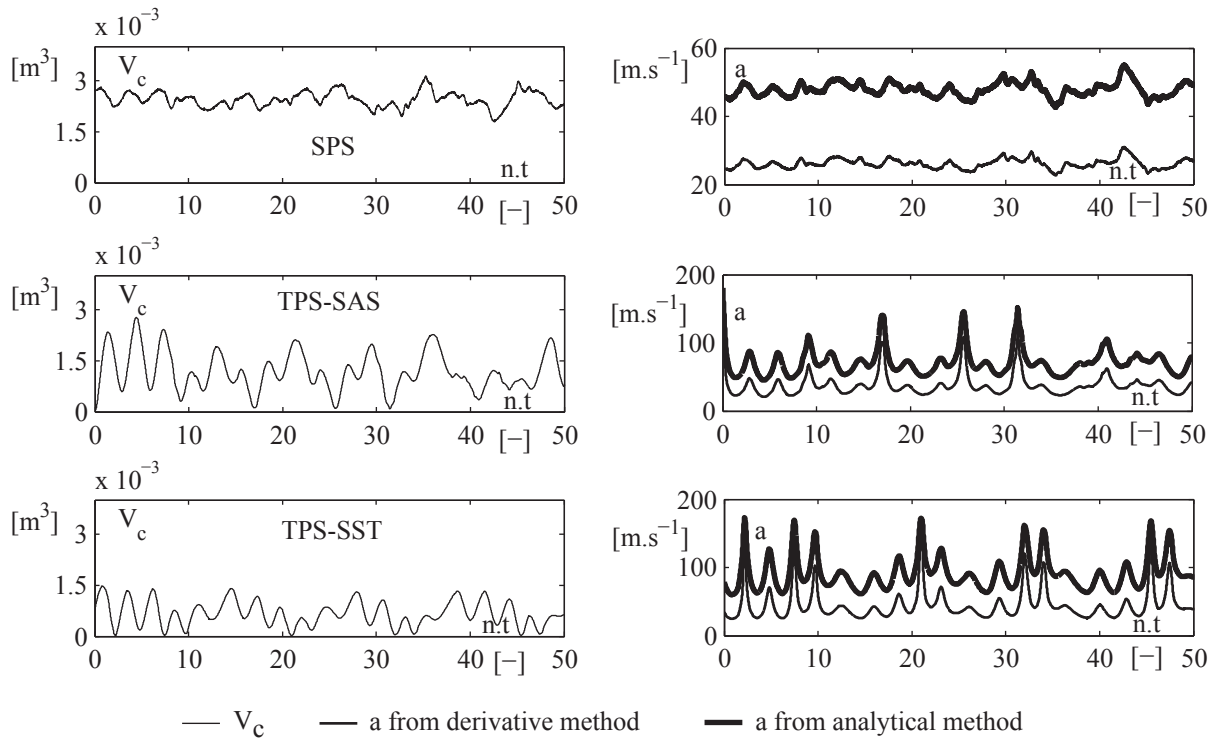


Figure 12.21: Comparison of the time history wave speed derived from the derivative and the analytical methods

the HD model. It has been observed that the cavitation volume experiences fluctuations despite constant boundary conditions applied to the HD model. The unsteady hydrodynamic field inside the draft tube flow is the cause of this cavitation volume fluctuations. The pressure p in Equation 12.11 can be split into two components: a HA part due to the propagation waves and a HD part due to the incompressible fluid motion. However, since a one way simulation is carried out to compute this wave speed, the HA part of the pressure field is not taken into account. Hence a reference pressure of the HD model is considered and set to the constant outlet pressure of the HD computational domain.

Table 12.2: Comparison of the time averaged equivalent compliance and wave speed derived from derivative and analytical methods applied to a lumped HA model

Method	Simulation	\bar{C}_{equ} [m ²]	\bar{a} [m.s ⁻¹]
Derivative	SPS	3.0 10 ⁻³	26
	TPS-SAS	1.8 10 ⁻³	38
	TPS-SST	1.4 10 ⁻³	45
Analytical	SPS	8.8 10 ⁻⁴	48
	TPS-SAS	4.4 10 ⁻⁴	72
	TPS-SST	2.7 10 ⁻⁴	92

Therefore, the wave speed variation in time is only due to the fluctuation of the cavitation volume fraction β .

In Figure 12.21, the time history of the cavitation volume is plotted and the resulting time history of the wave speed derived from the two methodologies are compared. The investigated Thoma number is 0.38 and a comparison between single phase and two phase simulations is shown. Whatever the simulation considered, a shift between the two methodologies is observed. The time averaged equivalent compliance and wave speed values are computed for the two methodologies and are summarized in Table 12.2.

Cavitation compliance identification for a distributed HA model

For a distributed HA model, the two methodologies can be used. Instead of considering the total cavitation volume in the cone and elbow parts, the cavitation volume is computed in each continuity control volume. For the "derivative method", a power law is found for each continuity control volume and look up tables making relation between the cavitation volume and the equivalent compliance or the wave speed are derived. Regarding the "analytical method", the pressure p in Equation 12.11 is still kept as a constant and equal to the outlet pressure of the computational domain. These two methodologies are compared and applied to a distributed HA model. In Table 12.3 the time averaged wave speeds obtained from the two methodologies are compared in each continuity control volume for single phase and two phase simulations. For convenience, the corresponding equivalent compliances are not mentioned in Table 12.3 since the difference between the two quantities is proportional to the geometrical data of the continuity control domains.

Whatever the simulation considered, the wave speed is the lowest in the continuity control volumes under the runner where the volume fraction of cavitation volume is the highest. Moreover, it can be deduced that the analytical method leads to higher wave speed values than the derivative method. This behavior has been observed as well when a lumped HA model is considered, see Table 12.2.

12.2.4 Thermodynamic Damping

The viscoelastic behavior of a standard pipe without cavitation onset allows to model the energy dissipation due to the wall deflection and the fluid compressibility. However, in the

Table 12.3: Comparison of the time averaged wave speed derived from derivative and analytical methods applied to a distributed HA model

Continuity domain	\bar{a} [m.s ⁻¹]					
	Derivative			Analytical		
	SPS	TPS-SAS	TPS-SST	SPS	TPS-SAS	TPS-SST
1	21.1	23.7	31.2	28.8	40.1	46.5
2	18.3	29.2	54.6	27.3	50.6	66.6
3	16.9	32.5	60.4	28.3	53.2	72.2
4	15.3	37.1	71.4	32.6	62.0	92.0
5	24.1	51.8	102.9	59.5	87.6	124.9
6	111.9	112.4	142.9	138.7	135.6	154.3
7	133.7	140.5	158.8	153.6	154.2	162.5
8	163.1	159.1	166.3	165.8	164.0	166.5
9	165.6	165.5	165.6	165.6	165.6	165.6
Lumped	26	38	45	48	72	92

HA draft tube model where cavitation may appear, this viscoelastic behavior is neglected since it is assumed that most of the dissipation is due to the cavitation compliance rather than the wall deflection. As described in Section 7.3.4, the bulk viscosity modeling this thermodynamic damping is computed from an analytical model developed by Pezzinga [75]. The formulation proposed by the authors is function of the cavitation volume fraction β , the wave speed a and the pressure p , see Equation 7.46. According to the equation, if cavitation does not occur, the bulk viscosity is equal to zero and energy dissipation in the HA draft tube model is not experienced since the viscoelastic behavior of the pipe is neglected. Therefore, by considering the dissipation only due to the cavitation compliance, a wrong modeling of the dissipation is carried out when cavitation does not occur. Equation 7.46 is used to derive the bulk viscosity at each time step of the numerical simulations performed with the HD model of the cavitating vortex rope. As the same approach as the "analytical method" to compute the equivalent compliance, the pressure p in Equation 7.46 is set to the outlet pressure of the HD computational domain.

In Table 12.4, and Table 12.5 the time averaged thermodynamic dampings (or bulk viscosities) are computed respectively for lumped and distributed HA draft tube models with wave speeds derived from the "derivative" and the "analytical" methods described in Section 12.2.3 for the investigated Thoma number of 0.38.

This bulk viscosity modeling a thermodynamic damping is not well known and order of magnitudes are difficult to find in the literature. However, the concept of the second viscosity modeling the viscoelastic behavior of the wall deflection has been more studied by some authors [42], [56], [46] who found out very high values around 10^9 Pa.s compared to the thermodynamic bulk viscosity derived from the Pezzinga's analytical model.

Table 12.4: Comparison of the time averaged thermodynamic dampings derived from derivative and analytical methods applied to a lumped HA model

$\bar{\mu}''$ [Pa.s]		
Simulation	Derivative	Analytical
SPS	612	6944
TPS-SAS	1238	14002
TPS-SST	1208	18808

Table 12.5: Comparison of the time averaged thermodynamic dampings derived from derivative and analytical methods applied to a distributed HA model

$\bar{\mu}''$ [Pa.s]						
Continuity domain	Derivative			Analytical		
	SPS	TPS-SAS	TPS-SST	SPS	TPS-SAS	TPS-SST
1	742	684	1516	2576	5093	6641
2	465	1042	2604	2313	7490	8017
3	318	935	2237	2486	7346	8183
4	161	999	2335	3339	9131	11049
5	298	1127	2762	10448	13311	12496
6	459	826	1081	8968	8598	5692
7	367	421	935	5840	4280	2560
8	31	95	32	608	1228	104
9	2	3	0	0	4	0
Lumped	612	1238	1208	6944	14002	18808

12.2.5 Influence of the Elbow on the HA Parameters

It has been shown in Section 12.2 that the intensity of the momentum and the mass sources feature high intensity in the elbow. It can be assumed that the complex 3D flow in the elbow gives rise to the hydroacoustic sources able to interact with the hydraulic system. This observation confirms the Fanelli's vortex rope model [36] which shows that the elbow is the driving mechanism of synchronous oscillations experienced by the flow. He assumed that the excitation is due to the interaction between the vortex rope and the secondary flow in the elbow and the divergent. To highlight the influence of the elbow on the hydroacoustic sources, the Lighthill source term S and the momentum sources S_h have been computed in a straight draft tube computational domain. This draft tube is fed with the same turbine runner rotating at the unchanged runner frequency n . A single phase computation is considered with the SAS-SST turbulence model and the same boundary conditions are applied. Figure 12.22 shows the new computational domain with the computed normalized standard deviations of the Lighthill source term S and momentum

source terms S_h as function of the momentum control volumes.

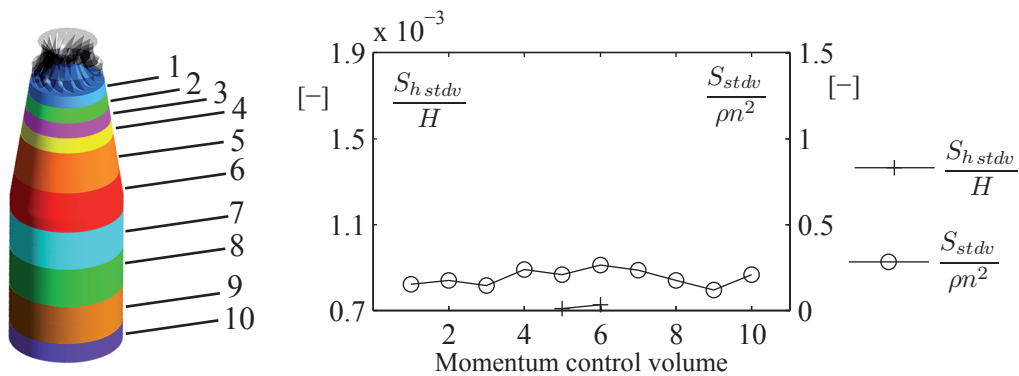


Figure 12.22: Standard deviations of the momentum sources S_h and the volume averaged Lighthill source term S as function of the location in the straight draft tube domain

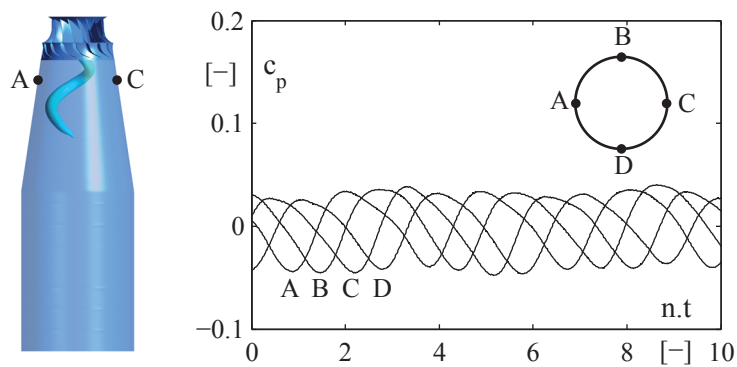


Figure 12.23: Computation of the helical vortex rope precession in a straight draft tube with the monitored wall pressure fluctuations in the cone

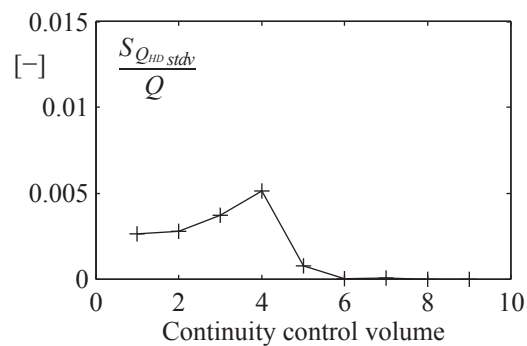


Figure 12.24: Standard deviations of the mass sources $S_{Q_{HD}}$ as function of the location in the straight draft tube domain

Compared to Figure 12.9 intensity of the hydroacoustic source terms are much lower for the computation with the straight draft tube domain. Despite this, a helical vortex rope is well developed in the flow as shown in Figure 12.23 by the surface region bounded by the vapor pressure p_v . Hence, wall pressure fluctuations in the cone are caused by the passage of the cavitating vortex rope near the wall. The time signals of the pressure fluctuations feature a rotating part much more higher than the synchronous part due to the excitation source. However, when the elbow is considered, the amplitude of this synchronous part in the time signals of pressure fluctuations is increased. Regarding the mass source plotted in Figure 12.24 as function of the continuity control volume, cavitation volume fluctuations are still experienced with a maximum intensity at the end of the cone but with a lower value than for the elbow draft tube computation. As conclusion, the amplitude of the hydroacoustic sources is strongly increased by the elbow part in which interaction between the vortex core and the secondary flows occurs, as explained by Fanelli [36]. However, even if the intensity is decreased with a straight draft tube, resonance phenomena can occur since excitation source is still generated.

12.3 Validation of HA Draft Tube Model Parameters

12.3.1 Hydraulic System Description

In this Section, it is proposed to validate the computed HA draft tube model parameters by performing a simulation of a part load resonance for which the precessing frequency of the cavitating vortex rope matches with one of the system's eigenfrequency. This phenomenon has been extensively studied experimentally by many authors [24], [25], [70], [71], [1], [39]. They analyzed the influence of the Thoma number on the pressure fluctuations in the system. By decreasing this parameter, the cavitation volume increases and modifies the eigenfrequencies of the system to match with the vortex rope precession frequency at the resonance. Figure 12.25 shows the typical evolution of pressure fluctuation amplitudes in the draft tube as function of the Thoma number measured by Dörfler in 1982 [25] and confirmed afterwards by other experimental investigations carried out by many authors.

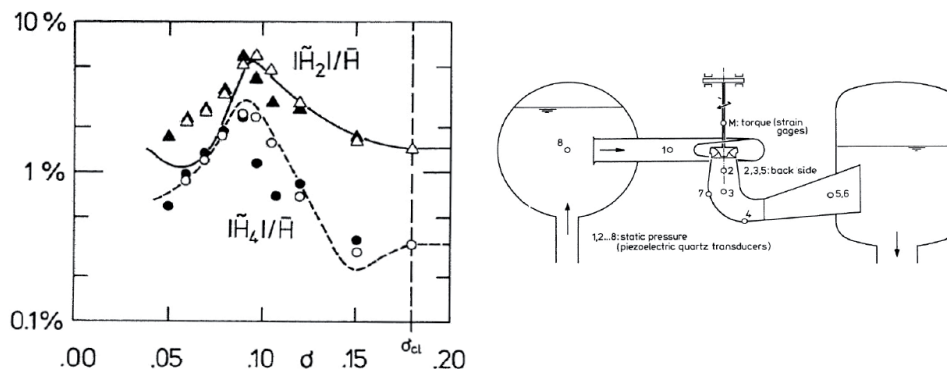


Figure 12.25: Pressure fluctuations measurements in the draft tube cone as function of the Thoma number [25]

Dörfler compared measurements to simulations results performed with a HA model of the test rig. Actually, he identified the momentum source from the synchronous component contained in the pressure fluctuations measured with four wall pressure sensors located in the same cone cross section. This momentum source identification was performed in cavitation free condition and assumed that the amplitude of this source is identical for cavitating regime. Moreover, he identified the cavitation compliance from the "derivative method" presented in Section 12.2.3 for a lumped model. By injecting both this momentum source and the cavitation compliance in his HA model, prediction of pressure fluctuations in the whole hydraulic system were in good agreement with measurements. The measured and predicted maximum of pressure fluctuation amplitude is found in the draft tube cone with an amplitude less than 10% of the turbine head, see Figure 12.25. In this Section, the aim is to reproduce this typical resonance curve from numerical simulations with the HA parameters identified in Section 12.2. The layout of the chosen test case is shown in Figure 12.26 and is constituted of an upstream reservoir, a penstock and the investigated Francis turbine model connected directly at the draft tube outlet to a downstream reservoir.

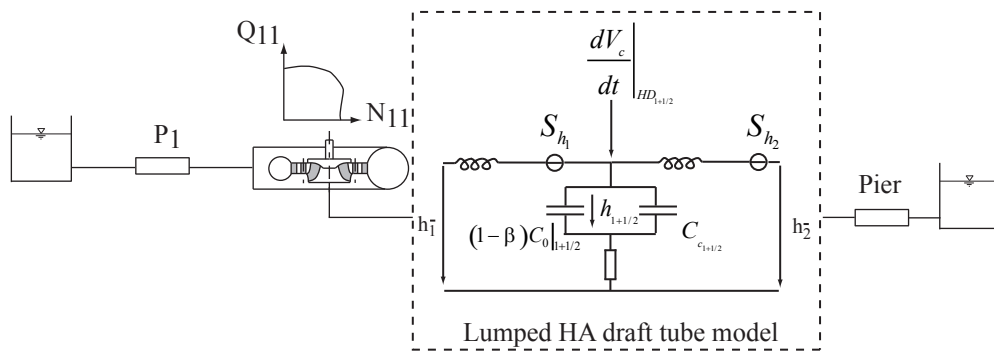


Figure 12.26: Layout of the hydraulic system used for validation of the HA parameters

To be able to compare with the Dörfler's investigation, a lumped draft tube model is used and the cavitation compliance is derived from the "derivative method". In the HA model, two momentum sources S_{h1} and S_{h2} must be setup whereas ten momentum sources have been computed. Since only the cone and the elbow parts are considered in the HA model, the nine first momentum control volumes are considered. Therefore, at each time step the momentum sources computed in each considered control volume are added and then divided by two. The length of the upstream pipe is set to 75 meters long to get a resonance on the first eigenmode. Regarding the water levels in the reservoirs they are set up to insure a flow rate through the turbine equal to the one of the operating point simulated with the HD model and a static pressure at the draft tube outlet $p_{\bar{1}}$ in accordance with Equation 12.1 for the Thoma number of interest. The eigenfrequencies of this hydraulic system are driven by the wave speed set in the lumped HA model. By decreasing the Thoma number, the wave speed decreases inducing a decrease of the eigenfrequencies. In Figure 12.27, the evolution of the wave speed and the normalized first eigenfrequency as function of the Thoma number are plotted. The variation law of the wave speed has been derived from a combination between two look up tables: the one making a relation between the cavitation volume and the wave speed given in Figure

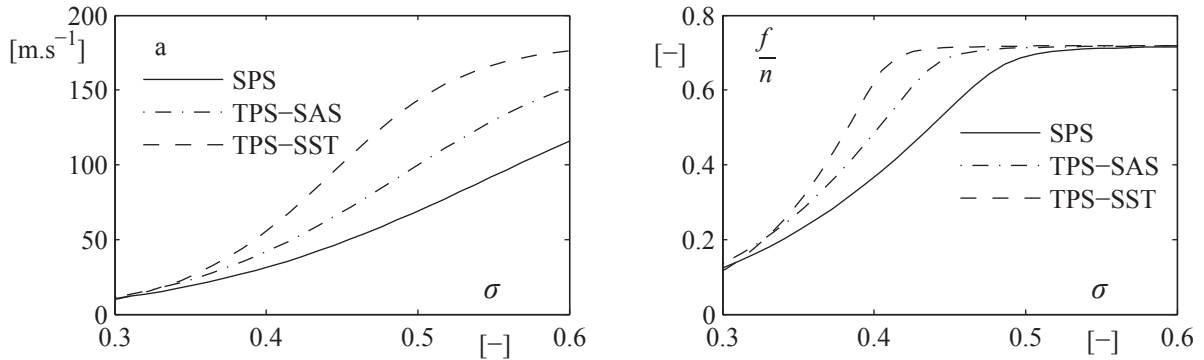


Figure 12.27: Evolution of the wave speed (left) and the normalized first eigenfrequency (right) as function of the Thoma number

12.20 and the other one making a relation between the cavitation volume and the Thoma number given in Figure 12.7. Once this variation law is defined, the correspondence between the wave speed and the first eigenfrequency of the hydraulic system is determined by using a small perturbation stability analysis as described in Section 10.2. As a result, the evolution of the first eigenfrequency as function of σ is found. Knowing that the precessing vortex rope frequency is around $0.3n$, the resonance will occur with the first eigenmode of this hydraulic system.

12.3.2 One Way Simulation of a Part Load Resonance

For each Thoma number, a one way simulation is carried out. This means that the time histories of the HA parameters identified in the HD model as a pre-processing step are injected in the HA model of the hydraulic system.

First, results from single phase simulations are considered. In Figure 12.28 the standard deviation of the pressure fluctuations in the draft tube as function of the Thoma number is plotted. A resonance phenomenon is experienced for a Thoma number of 0.38 with a maximum amplitude of 6.8% of the turbine head. Moreover, the typical shape of the resonance curve is found with an amplitude of 1% out of resonance conditions. These order of magnitudes are in good agreement with the amplitudes found in the literature. Moreover, the influence of the mass source and the thermodynamic damping on the amplitudes are investigated. Indeed, the maximum amplitude strongly depends on these two HA parameters. If the mass source or the thermodynamic damping are not taken into account in the modeling, the maximum amplitude is respectively decreased up to 4% and increased up to 11% of the turbine head. The pressure fluctuations frequencies in the whole hydraulic system are represented in Figure 12.29 for two cavitation conditions. These surfaces are built from the amplitude spectra pressure fluctuations plotted at each pressure node of the HA model including the one in the draft tube (DT), located at the node number 41, where the maximum of pressure fluctuation amplitude is experienced when cavitation onset fulfills the resonance condition. This observation is due to the huge cavitation compliance in the draft tube which tends to deform the shape of the first eigenmode by moving the antinode toward the vapor cavity location. Moreover, the fundamental frequency of pressure fluctuations corresponds to the vortex rope fre-

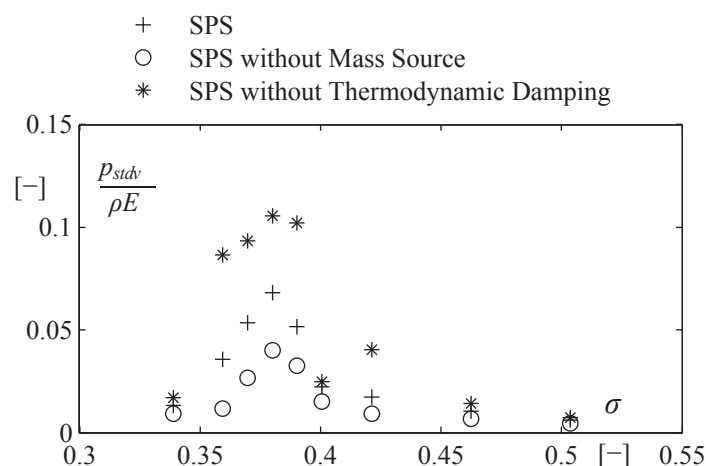


Figure 12.28: Standard deviation of pressure fluctuations at the draft tube pressure node as function of the Thoma number using numerical results from single phase simulation

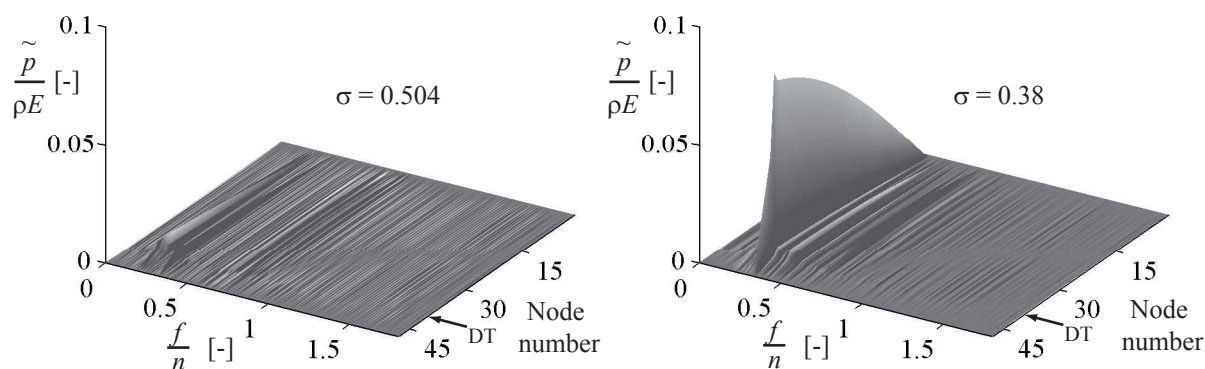


Figure 12.29: Surface representation of amplitude spectra pressure fluctuations as function of the position in the hydraulic system out of resonance (left) and at resonance (right) conditions

quency which matches with the first eigenmode frequency of the hydraulic system. The methodology employed to compute the HA draft tube parameters from the HD model by considering single phase simulation is able to predict a resonance occurrence with pressure fluctuations amplitudes in good agreement with the literature.

However, the results obtained with HA draft tube parameters derived from two phase simulations are less satisfying. In Figure 12.30, the standard deviation of the pressure fluctuations in the draft tube as function of the Thoma number is plotted. The maximum of amplitude exceeds 10% of the turbine head which is higher than the case where HA draft tube parameters are derived from single phase simulations. Moreover, the shape of the resonance curve is less conventional according to the measurements found in the literature. In Figure 12.31, pressure fluctuations frequencies in the whole hydraulic system are plotted. One can observe that many frequencies are contained in the time signal of pressure fluctuations in the system. It seems that high order eigenmodes may respond to

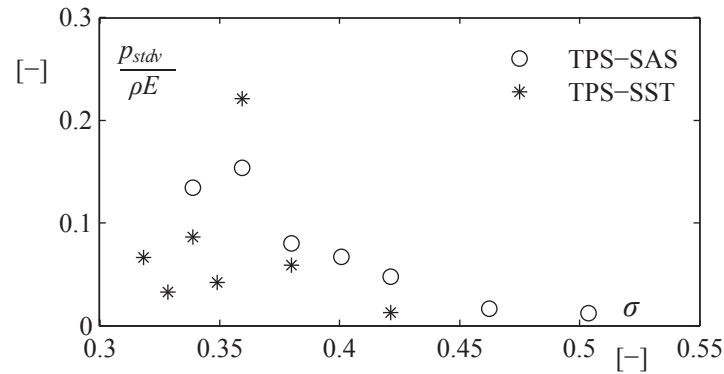


Figure 12.30: Standard deviation of pressure fluctuations at the draft tube pressure node as function of the Thoma number using numerical results from two phase simulation

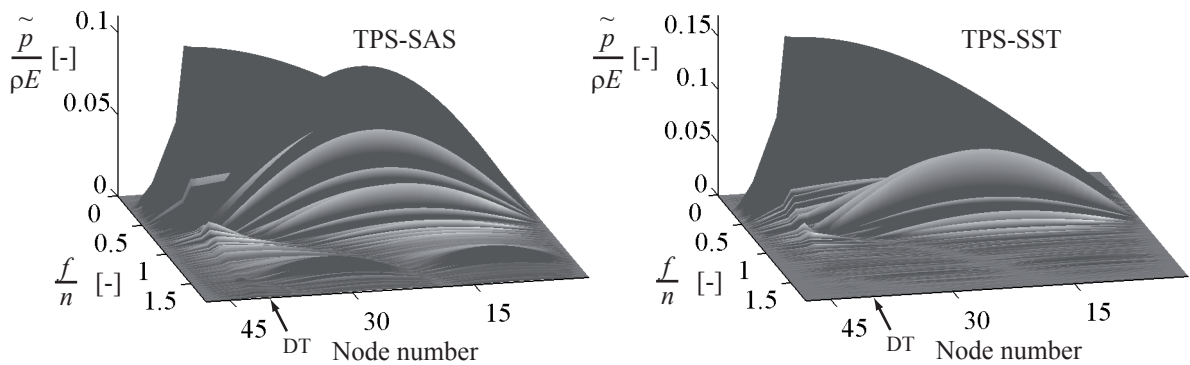


Figure 12.31: Surface representation of amplitude spectra pressure fluctuations as function of the position in the hydraulic system at the resonance. Comparison between SAS-SST (left) and SST (right) turbulence models

the excitation induced by the cavitating vortex rope. This may be due to the fact that two phase flow simulations feature more unsteady behavior and thus provide more energy in a broad band range.

12.3.3 Modeling of Nonlinear Hydroacoustic Feedback

The above resonance curves have been derived from one way simulations consisting in injecting the HA parameters derived from the HD model in the HA draft tube model. The feedback of the HA field on the HA draft tube parameters is modeled and considered on the mass source by introducing the wave speed parameter, see Section 7.3.3. Considering a one way simulation, parameters related to the cavitation volume such as the wave speed and the thermodynamic damping experience fluctuations due to the cavitation volume fluctuations induced by the unsteady HD field in the draft tube. However, a feedback of the HA field on the cavitation volume fluctuations and consequently on the wave speed and the thermodynamic damping parameters should be taken into account. It is proposed in this Section to model a nonlinear HA feedback on the cavitation volume fluctuations which implicitly influences nonlinearly the wave speed and the thermodynamic damping

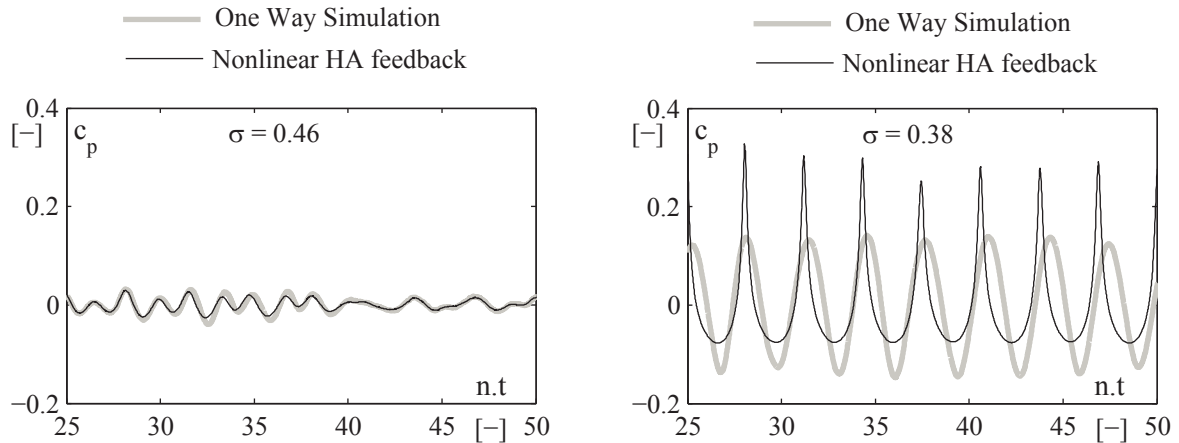


Figure 12.32: Comparison of the simulated pressure fluctuations in the draft tube between one way simulation and simulation with nonlinear HA feedback on the wave speed and the thermodynamic damping parameters

parameters. By comparing the results obtained between single phase and two phase simulations, it is proposed in this Section to apply the nonlinearity to the HA draft tube parameters derived from single phase simulations. The nonlinearity is assumed to be due to a dependency of the HA parameters to the hydroacoustic pressure field p_{HA} as follows:

$$\begin{aligned} a &= f(p_{HD}, p_{HA}) \\ \mu'' &= g(p_{HA}, \beta(p_{HD}, p_{HA})) \end{aligned} \quad (12.12)$$

For the following simulations presented in this Section it is assumed that the contribution of the HD pressure field p_{HD} is much less important than the contribution of the HA pressure field especially at hydroacoustic resonance conditions. The variation laws of the wave speed and the cavitation volume fraction β as function of the HA pressure are derived in two steps. First a relation between the wave speed or the cavitation volume fraction and the Thoma number is set from the look up tables given respectively in Figure 12.27 and Figure 12.7. Then the correspondence between the Thoma number and the pressure is derived from Equation 12.1. In Figure 12.32 a comparison of the simulated pressure fluctuations in the draft tube between a one way simulation and a simulation with nonlinear HA feedback is shown for two Thoma numbers. In the left figure, the Thoma number is set to $\sigma = 0.46$ which corresponds to a system in out of resonance conditions. In that case the influence of the HA field on the HA parameters is negligible since the results between the two simulations are quite similar. However when the Thoma number is set to $\sigma = 0.38$ corresponding to resonance conditions, the simulated pressure fluctuations feature different shape and slightly different amplitude. Hence, at the resonance the nonlinear HA feedback has an influence. This typical shape obtained with nonlinear HA parameters is usually measured on test rig, such as the experimental investigation of Fritsch and Maria [39] shown in Figure 12.33. Amplitude spectra of pressure fluctuations at the Thoma number value of 0.38 are plotted in Figure 12.34 to compare the results between the one way simulation and the simulation with nonlinear HA feedback. For the one way simulation, spectrum features only the fundamental frequency of the cavitating

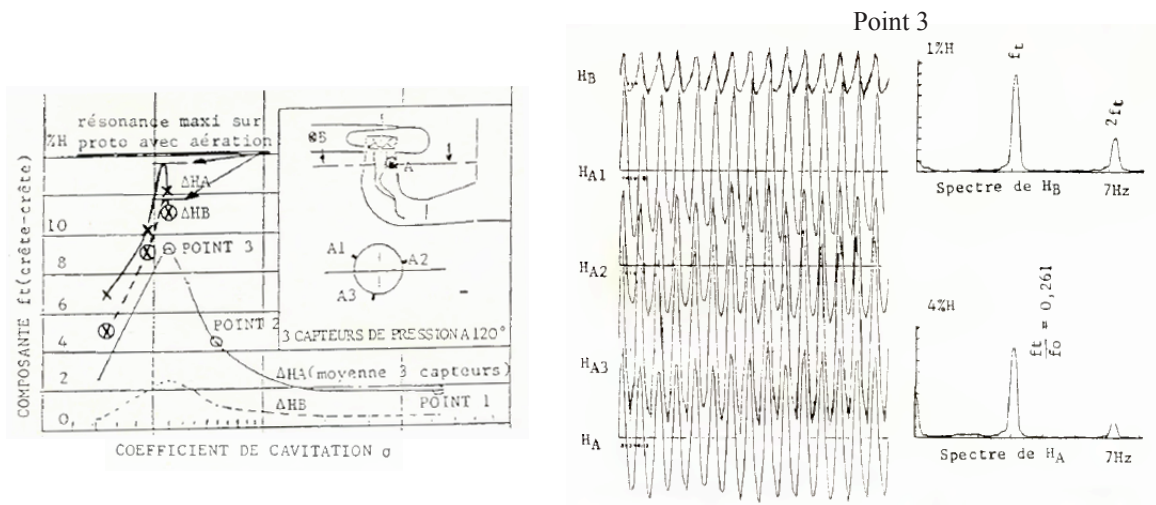


Figure 12.33: Pressure fluctuation measurements in the draft tube cone at part load resonance [39]

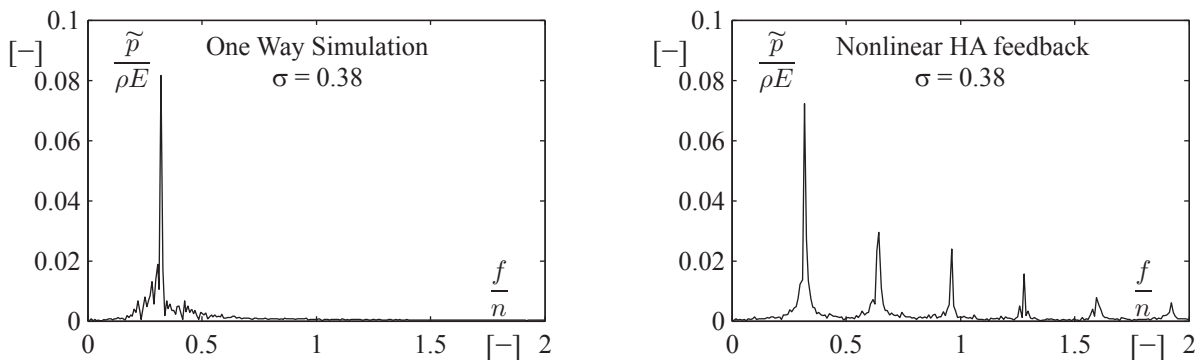


Figure 12.34: Amplitude spectra of pressure fluctuations in the draft tube obtained in the one way simulation (left) and simulation including nonlinear HA feed back (right) at the Thoma number value of $\sigma = 0.38$

vortex rope precession due to the sinusoidal shape of the time signal. However, in the case of nonlinear HA feedback, the sharpened shape of the time signal induces in the amplitude spectrum the fundamental and the first harmonics. The amplitude of the fundamental is slightly lower than the case of the one way simulation. This can be explained by the wave speed fluctuation which is higher than in the one way simulation. Indeed, this parameter defines the eigenfrequencies of the hydraulic system and therefore the matching between the vortex rope frequency and the first eigenfrequency is less precise if nonlinear HA feedback is considered. The fluctuations of the wave speed and the thermodynamic damping during the simulation are plotted in Figure 12.35 for a Thoma number value of $\sigma = 0.38$.

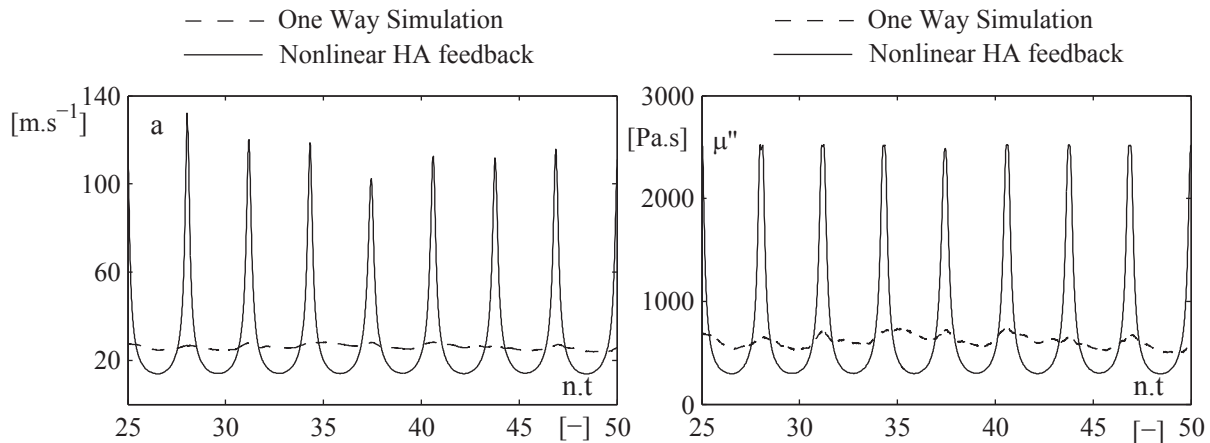


Figure 12.35: Wave speed (left) and thermodynamic damping (right) fluctuations obtained with a one way simulation and with a simulation with nonlinear HA feedback at the Thoma number value of $\sigma = 0.38$

12.4 Upper Part Load Resonance Simulation

12.4.1 Identification of Cavitation Volume Fluctuation

The swirling flow leaving the runner in Francis turbine under part load operation leads to pressure fluctuations featuring fundamental frequency in the range of 0.2 to 0.4 times the runner rotational frequency. This frequency may matches with one of the eigenfrequency of the system leading to resonance phenomena as simulated in Section 12.3. For the upper part load operation range, pressure surge fluctuations may occur in a higher frequency range between 2 and 4 times the runner frequency and may feature modulations at the vortex rope precession frequency. Nowadays the mechanism being able to induce this upper part load resonance is still unknown. Some authors explain this phenomenon as the response of the hydraulic system to periodic impacts of the vortex rope on the inner elbow part of the draft tube [27] [68] [4], whereas others think that it is related to the self rotation of the cavitating vortex core featuring an elliptical shape [55] [43] [77] [69]. As described in details in Section 11.1, the occurrence of this phenomenon is very sensitive to the Thoma number and appeared at a Thoma number value of 0.38. Regarding the analysis of the hydroacoustic sources performed in Section 12.2, an excitation frequency around $2.5n$ has not been observed at this Thoma number value. Neither periodic impacts nor self rotation vortex rope core have been identified.

Since this phenomenon is strongly influenced by the Thoma number, the global momentum source has been computed for several Thoma numbers considering both single phase and two phase simulations with the SAS-SST and SST turbulence models. The occurrence of an excitation frequency around $2.5n$ in the global momentum source has been observed only for the two phase simulation with the SST turbulence model. Indeed the SAS-SST turbulence model do not allow to capture this frequency. In Figure 12.36, the amplitude spectra of the global momentum source are computed for a two phase simulation with the SST turbulence model as function of the Thoma number. These amplitude spectra are computed over a time simulation corresponding to 60 runner revolutions. For

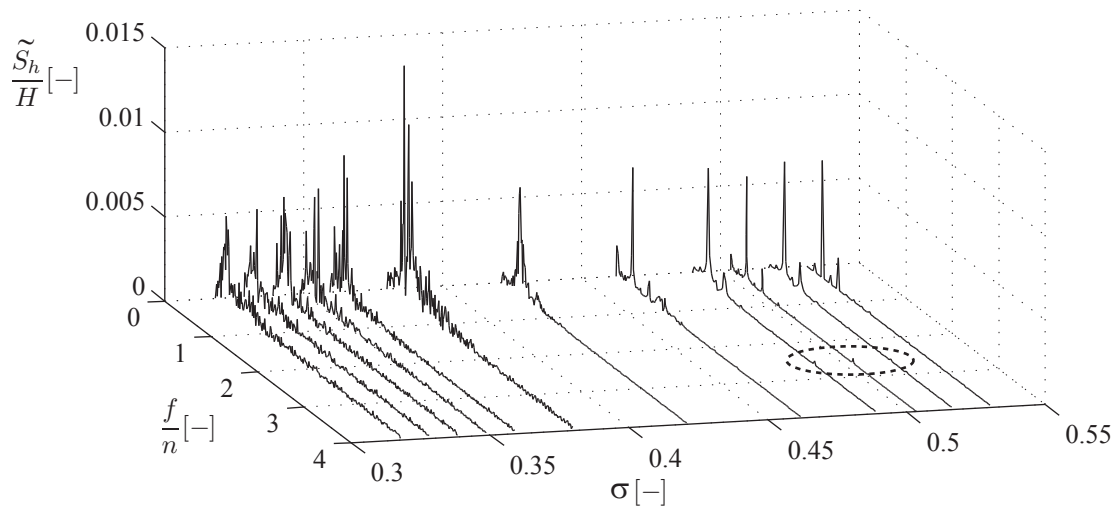


Figure 12.36: Influence of the Thoma number on the global momentum source derived from the HD two phase flow simulation with the SST turbulence model

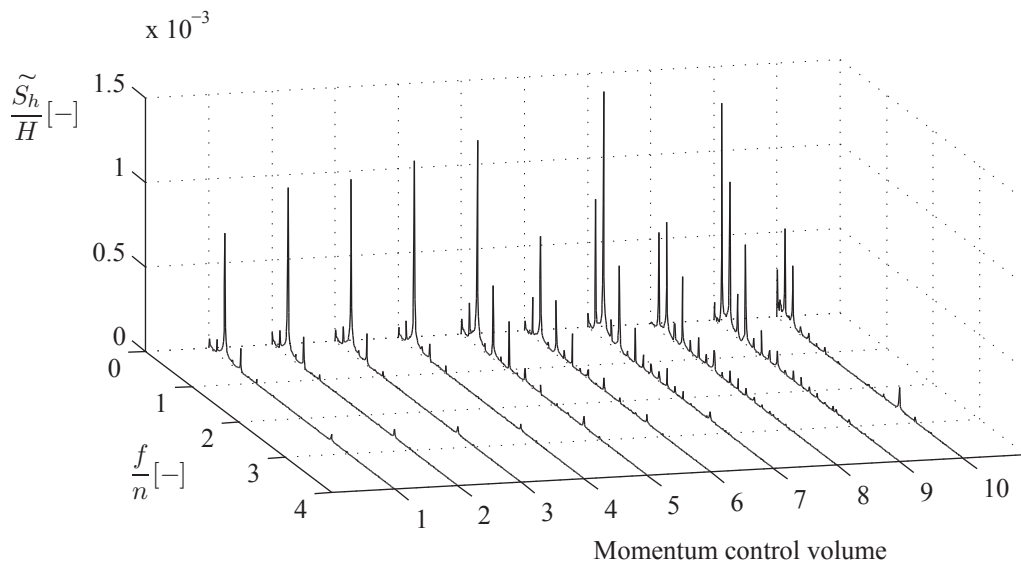


Figure 12.37: Waterfall diagram of the amplitude spectra of the momentum sources S_h in the momentum control volumes derived from the HD two phase flow simulation with the SST turbulence model

the low Thoma numbers where cavitation volume is higher than for high Thoma numbers, the amplitude spectra are much noisier due to the unsteadiness of the cavitation influence. One can observe that a frequency component at $2.6n$ appears for a Thoma number value between 0.49 and 0.52 which is far from the experiments. For these high Thoma number values the cavitation volume is very small compared to the experiments.

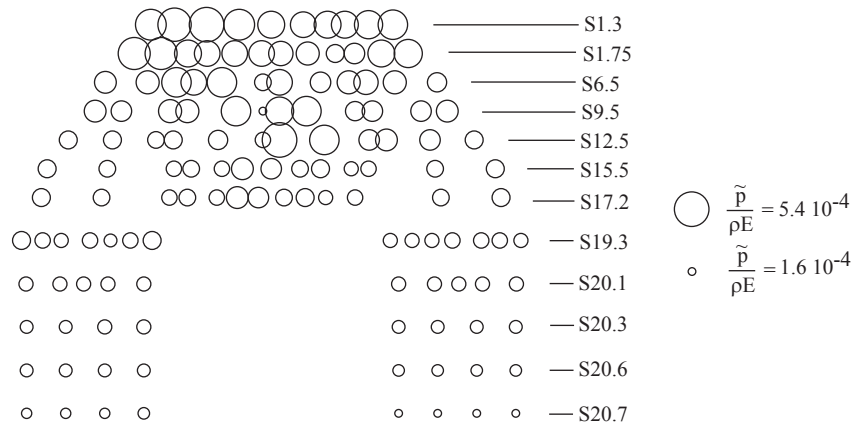


Figure 12.38: Representation of the wall pressure fluctuation amplitudes in the draft tube at the frequency $2.6n$

For the analysis of the phenomenon, the Thoma number value of 0.504 is considered afterwards where the amplitude of the high frequency component is maximum. In Figure 12.37, a waterfall of the amplitude spectra of the momentum sources considered along the draft tube domain is plotted. The high frequency component is found in the whole draft tube domain. This high frequency component observed on the HA sources, can be observed on the wall pressure fluctuations as well. Therefore, wall pressure monitoring points have been setup in the HD model and located in the cross sections represented in Figure 11.5. The wall pressure fluctuations amplitudes considered at the high frequency component are plotted in an unfolded draft tube representation, see Figure 12.38. Each horizontal line represents an unfolded draft tube cross section as the ones defined in Figure 11.5. The high frequency component amplitude, measured for each monitoring points, is represented by a circle whose diameter is proportional. Hence, one can observe that the amplitude decreases along the draft tube length and feature high amplitudes near the cavitation volume location just below the runner. Moreover, for any given cross section, wall pressure fluctuations at this high frequency component are in phase. To understand this phenomenon, the downstream flow rate fluctuations at the elbow outlet cross section Q_2 are monitored. Due to the high Thoma number value, only liquid phase is considered in this cross section.

In Figure 12.39 the amplitude spectrum of the outlet flow rate fluctuations is plotted and compared to the one of the global mass source corresponding to the cavitation volume fluctuations. The outlet flow rate features fluctuations at the high frequency component. However, the prescribed inlet flow rate of the HD model at the runner inlet Q_1 is constant. By applying the continuity equation to a control volume defined between the runner inlet and the elbow outlet, it yields to:

$$Q_1 - Q_2 = - \left. \frac{dV_c}{dt} \right|_{HD} = S_{Q_{HD}} \tag{12.13}$$

Since the inlet flow rate is constant, the downstream flow rate fluctuations are due to the cavitation volume fluctuations shown in Figure 12.39 by the amplitude spectrum of the global mass source which features this high frequency component as well. Therefore, the

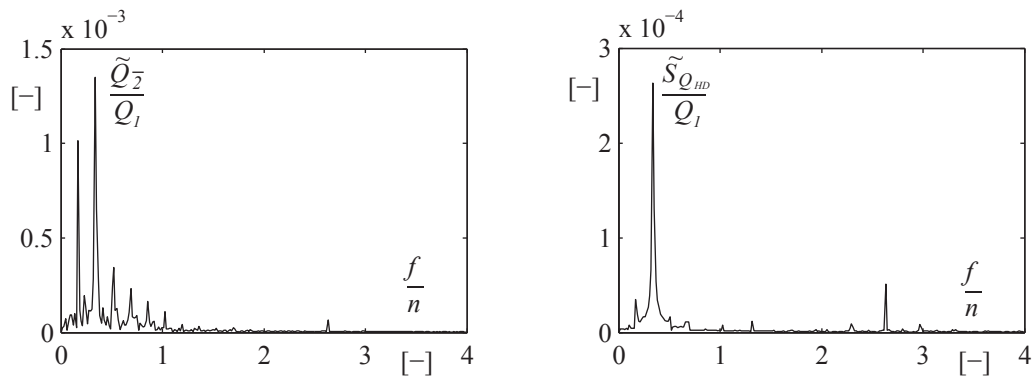


Figure 12.39: Amplitude spectra of the outlet flow rate Q_2 fluctuations (left) and mass source $S_{Q_{HD}}$ fluctuations (right) derived from the HD two phase flow simulation with the SST turbulence model

mechanism inducing upper part load resonance with the hydraulic system is identified to be related to an undesirable volume fluctuation occurring under certain cavitation conditions with a frequency pulsation which can match with an eigenfrequency of the system.

12.4.2 Hydroacoustic One Way Simulation

The fluctuations of the cavitation volume, described in previous Section, occur at a high Thoma number compared to the experiments. In this Section, the aim is to simulate the HA upper part load resonance from the HA draft tube model parameters derived at the same Thoma number as the experiments: $\sigma = 0.38$. First of all, HA draft tube model parameters are derived from the HD model considering the experimental Thoma number and then, the fluctuations at the high frequency component are modeled and integrated.

In Figure 12.40 the layout of the test rig where resonance has been experienced is given. The test rig is a closed loop system with one reservoir and two feed pumps in parallel. The HA model of the whole test rig has been built with the SIMSEN software

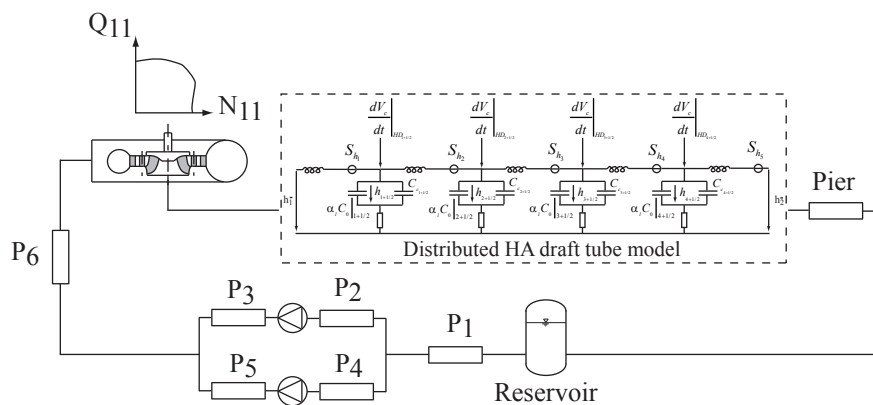


Figure 12.40: Layout of the test rig

Table 12.6: Comparison of the test rig's eigenfrequencies derived from the cavitation compliance computation with the derivative and the analytical methods

Eigenmode order	f/n [-]					
	Derivative			Analytical		
	SPS	TPS-SAS	TPS-SST	SPS	TPS-SAS	TPS-SST
1	0.30	0.38	0.57	0.52	0.64	0.65
2	0.68	0.68	0.71	0.69	0.80	0.95
3	1.23	1.23	1.24	1.24	1.25	1.27
4	1.44	1.64	1.91	1.83	1.91	1.92
5	1.92	1.92	2.57	1.91	2.61	2.61
6	2.39	2.61	2.71	2.62	2.98	3.32

by using both standard viscoelastic pipe models for the water passages and the turbine characteristic for the Francis turbine runner. The main HA model parameters of the water passages are taken from a previous model built for the analysis of the upper part load resonance as well but where it was assumed that the excitation source is periodic impacts on the inner elbow part [68]. A distributed HA draft tube model is chosen since the resonance occurs with a high order eigenmode, see Section 10.3.

In Table 12.6 the eigenfrequencies of the hydraulic system are computed by using a small perturbation stability analysis with the wave speed draft tube parameter setup from Table 12.3. The wave speed strongly influences the eigenfrequencies of the hydraulic system. However two methodologies have been proposed to compute the wave speed: the "derivative" and the "analytical" methods which provide different results. Hence eigenfrequencies differ according to the employed methodology. Moreover, differences between single phase and two phase simulations are observed. To perform the hydroacoustic upper part load resonance simulation, one methodology and one simulation must be chosen. From the experiment reports, the part load resonance with the first eigenmode at the vortex rope precession frequency was not feasible on the test rig for the investigated runner frequency. Knowing that the vortex rope precession frequency is near $0.3n$, the derivative method can be excluded since the part load resonance would have occurred with the first eigenmode. Hence, the analytical method which gives higher wave speed parameter values is chosen. The logic would like to use the two phase simulation results obtained with the SST turbulence model since it corresponds to the configuration where the cavitation volume fluctuation has been observed. However, using this configuration, hydroacoustic simulation is numerically unstable because of a wrong combination between the wave speed parameter and the thermodynamic damping.

The only working configuration is the case of the single phase simulation results for which the wave speed parameter is derived from the analytical method. In that case, the resonance would occur with the sixth order eigenmode which frequency value is $2.62n$. The shape of this eigenmode is given in Figure 12.41. In the left part of Figure 12.41, the eigenmode shape is plotted in the whole hydraulic system where the first and the last nodes correspond to the reservoir location. The draft tube component (DT) being located

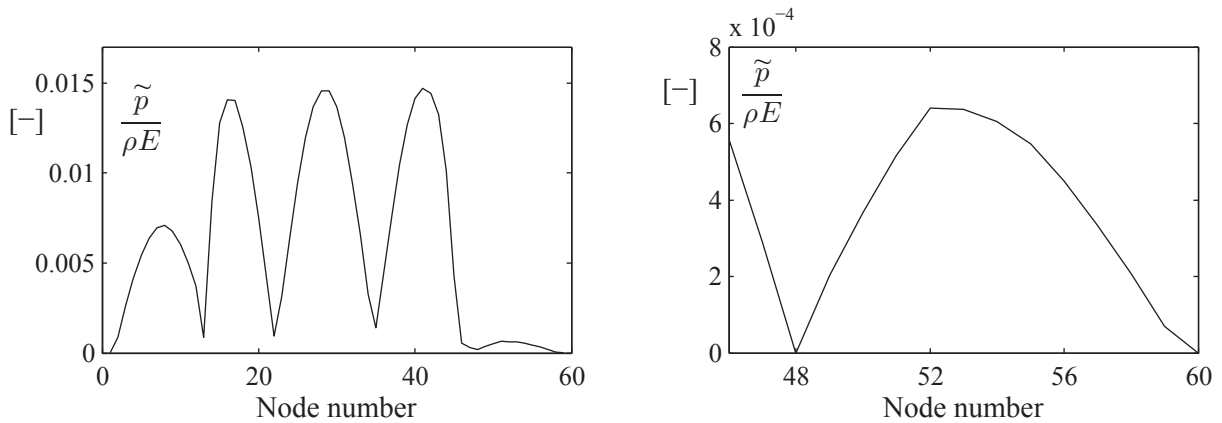


Figure 12.41: Shape of the sixth eigenmode in the whole hydraulic system (left) and in the draft tube component (right) with enlarged scale

between node numbers 46 and 60. In the right part, the shape is plotted in the draft tube component including the cone, the elbow and the two diffuser channels. The plotted pressure variable corresponds to the modulus of the complex eigenvectors which explains positive fluctuations in the whole system. However, the phases of these fluctuations are given by the argument of the eigenvectors. Due to the modeling approach which neglects the convective terms in the set of equations, the phase can only reach $\pm\pi$ values. At each pressure node, the phase changes to the opposite value. In the cone and the elbow parts, a pressure node is experienced which is in good agreement with experimental measurements showing a phase shift of 150° between the inlet and the outlet cone pressure fluctuations, see Figure 11.5.

The modeling of the cavitation volume fluctuations at the high frequency component is based on the results obtained at the high Thoma number value of 0.505. It has been found that a fluctuation of 1% of the time averaged cavitation volume induces a fluctuation of the hydroacoustic momentum sources in each momentum control volume around 0.005% of the turbine head. This ratio has been conserved as a reference to create a relation between cavitation volume fluctuation amplitude and momentum sources fluctuation amplitudes. Then, the amplitude of the cavitation volume fluctuation is taken as a parameter and an "optimal" value is determined in order to get amplitudes of pressure fluctuations at the high frequency in general agreement with measurements. In Figure 12.42, the chosen modeling is illustrated by the time history of the cavitation volume and the momentum source in the first control volume. Finally, the amplitude of the cavitation volume fluctuation corresponds to 15% of the time averaged cavitation volume.

Once the HA draft tube parameters are modified to model the cavitation volume fluctuations at the high frequency component, a one way simulation is carried out. This means that the time histories of the HA draft tube parameters are injected in the HA model of the complete hydraulic system. The resulting pressure fluctuation frequencies in the whole hydraulic system are represented in Figure 12.43. In the left part, the surface representation is built from the amplitude spectra pressure fluctuations plotted at each pressure node of the HA model. The draft tube component (DT) being located between node numbers 46 and 60. In the right part, the amplitude spectrum of pressure fluctuations in the draft tube cone is plotted. As expected, the sixth eigenmode responds

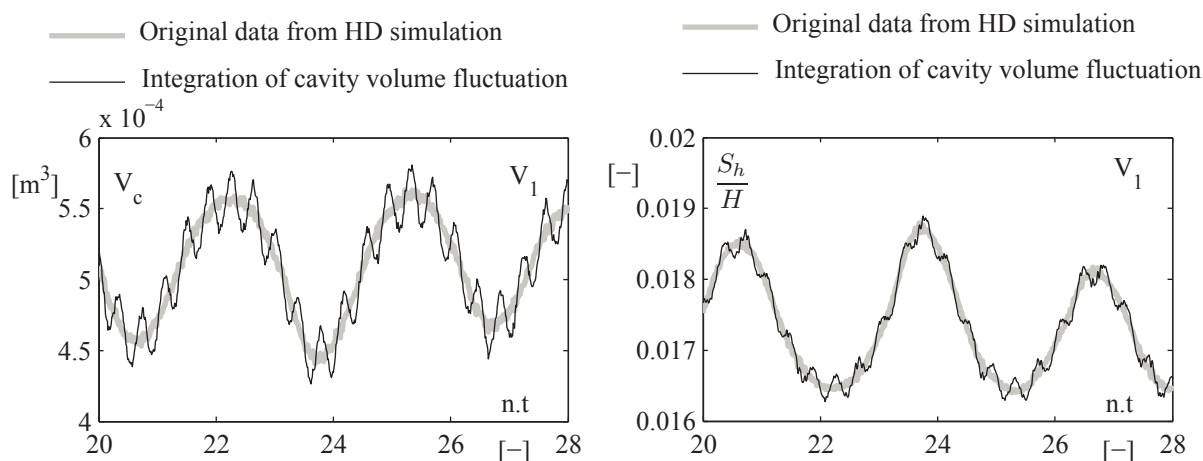


Figure 12.42: Integration of the cavitation volume fluctuation to the HD simulation data in the first control volume V_1

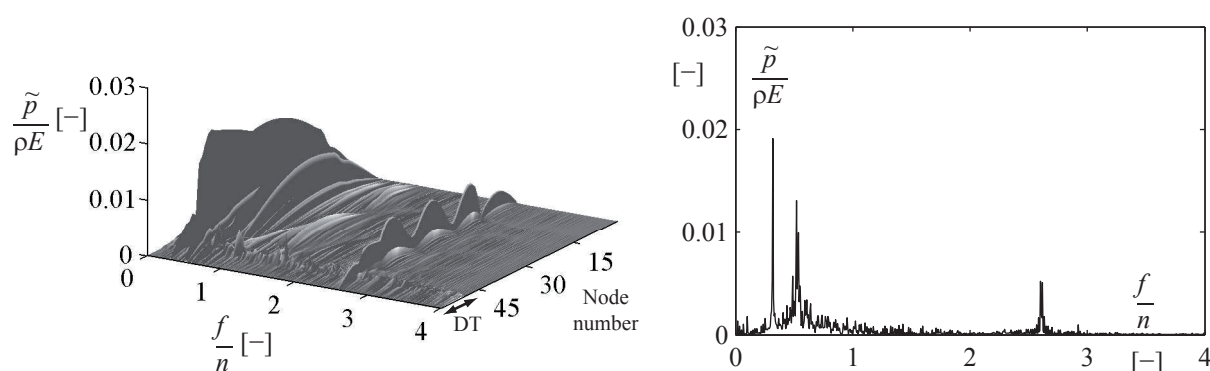


Figure 12.43: Surface representation of amplitude spectra pressure fluctuations as function of the position in the hydraulic system (left) and pressure fluctuations in the draft tube cone (right)

to the excitation due to the cavitation volume fluctuations. However, the first eigenmode characterized by a frequency of $0.52n$, responds as well contrary to the measurements. This maybe due to the second harmonic of the fundamental frequency corresponding to the vortex rope precession matching with the first eigenmode whose frequency fluctuates because of the unsteadiness of the wave speed parameter. In Figure 12.44, the influence of the thermodynamic damping is investigated by performing a one way simulation without considering this HA parameter. One can observe that the amplitude of the first eigenmode is much higher which confirms the importance of the thermodynamic damping parameter when cavitation is taken into account in the modeling.

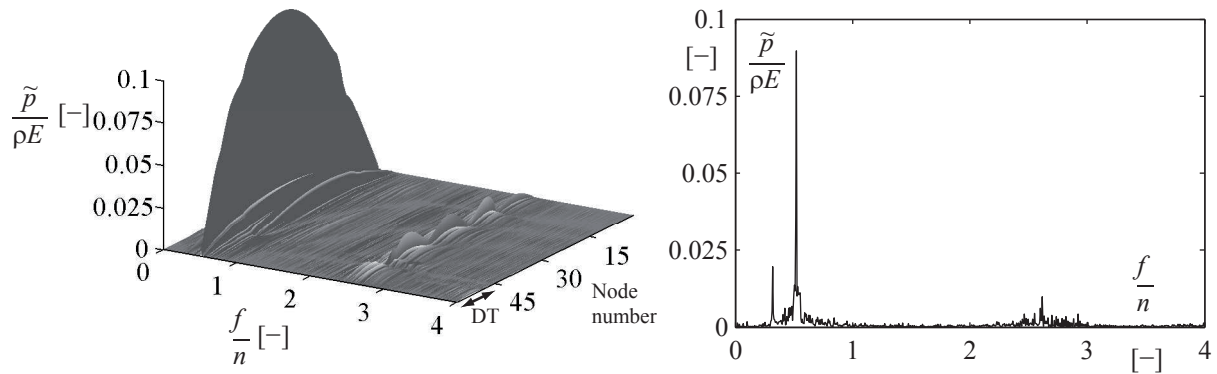


Figure 12.44: Surface representation of amplitude spectra pressure fluctuations as function of the position in the hydraulic system (left) and pressure fluctuations in the draft tube cone (right) without considering the thermodynamic damping parameter

12.5 Two Way Simulation of a Part Load Resonance

12.5.1 Hydraulic System Description

In this Section, the influence of a two way simulation on the HA draft tube model parameters is investigated at part load resonance conditions. The upper part load resonance phenomenon has not been chosen since the undesirable cavitation volume fluctuation, responsible of this kind of resonance, can be simulated for cavitation conditions inducing small cavitation volume compared to the experiments. In Section 12.3, a simple hydraulic system made of an upstream reservoir, a penstock and the investigated Francis turbine model connected directly at the draft tube outlet to a downstream reservoir has been used for a one way simulation of a part load resonance. It has been shown that due to the very low wave speed in the draft tube, the antinode of the pressure eigenmode is moved toward the vapor cavity location. Since a pressure antinode corresponds to a flow rate node of the flow rate eigenmode, the flow rate fluctuations experienced at the turbine inlet are negligible. Hence, according to the data flow described in Section 9, if this hydraulic system is used for the two way simulation, inlet boundary condition of the HD model would experience negligible fluctuations. For this investigation, the hydraulic system is chosen to experience a maximum of inlet boundary condition fluctuations applied to the HD model. Hence, to avoid the deformation of the eigenmode shape due to the low wave speed in the draft tube, the total length of the hydraulic system must be very long. It is proposed to use the HA model of the test rig, used for the upper part load simulation, whose length is increased in order to match the first eigenmode frequency with the vortex rope precession frequency. The layout of the hydraulic system is given in Figure 12.45. By increasing the length of the pipe P6 from 34m to 105m and considering the time averaged wave speed parameter derived from single phase simulation with the analytical method, see Table 12.3, the first eigenfrequency value is decreased up to $0.3n$ leading to the expected part load resonance phenomenon. The resulting spatial shape of the first eigenmode is given in Figure 12.46. The draft tube (DT) being located near the node number 100, one can observe that a maximum of flow rate fluctuations through the turbine is experienced.

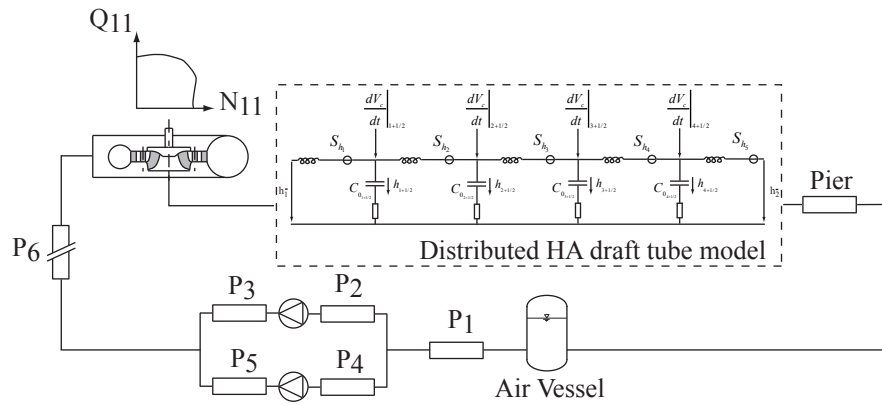


Figure 12.45: Layout of the hydraulic system used for the two way simulation

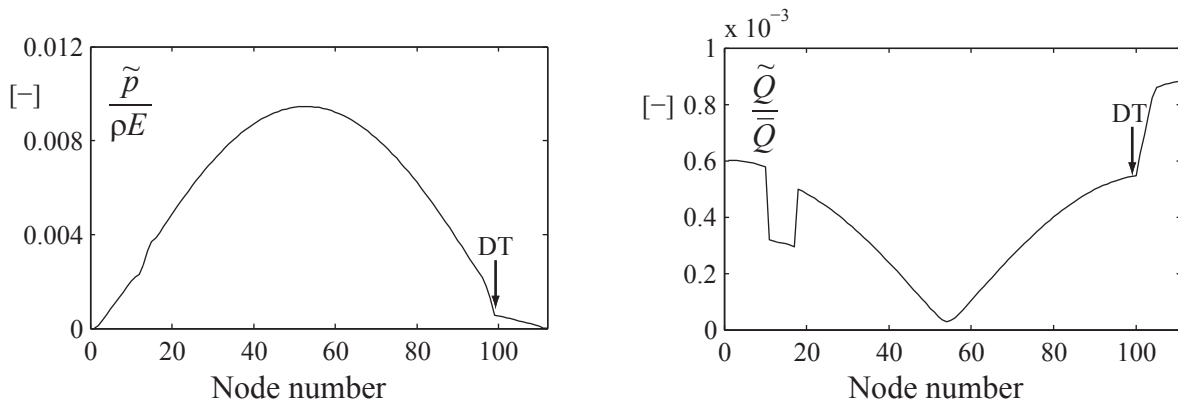


Figure 12.46: Shape of the first pressure (left) and flow rate (right) eigenmode

12.5.2 Data Flow and Time Integration

Since HA draft tube model parameters are computed at each time step in the different control volumes of the HD model, the discretized HA draft tube model is used for the two way simulation. The data flow between the two models has been described in details in Section 9. For a two way simulation, the modeling of the hydroacoustic feedback on the mass source leading to the cavitation compliance parameter is not used anymore since it is assumed that this feedback is included in the HD model due to the coupling. This data flow configuration has been tested at resonance conditions. However, the coupled simulation diverges immediately because of the mass source exchange. To avoid this divergence, a hybrid data flow configuration dealing with the mass source has been tested. The HA part of the mass source is assumed to be dominant compared to the HD part which is therefore not taken into account. Moreover, this HA part is still modeled with the cavitation compliance parameter. At each time step, the cavitation volume is computed in the control volumes of the HD model and the wave speed parameter, defining the equivalent capacitance C_{equ} , is derived from the analytical method, see Equation 12.11. Regarding the time integration, the time step and the time marching methods are different between the HD and the HA models. Indeed an implicit method with a time step dt_{HD}

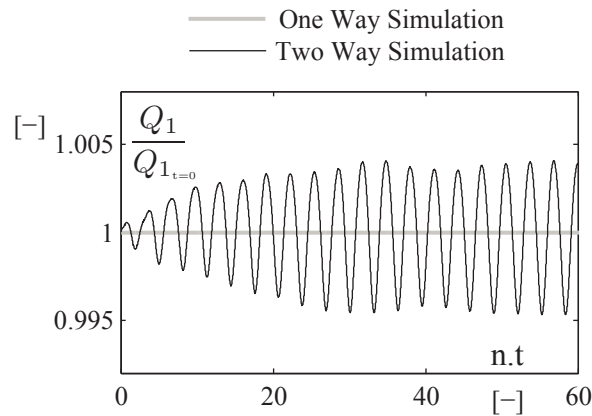


Figure 12.47: Time history comparison of the flow rate Q_1 applied at the inlet runner of the HD model between one way and two way simulations

is used to integrate the HD model whereas an explicit method with smaller time step $dt_{HA} = dt_{HD}/10$ is used to integrate the HA model [82]. Hence, within one time step of the HD model, the HA model is put forward of ten time steps. It is assumed that during these intermediate HA time steps, the HA source terms and the HA parameters derived from the HD model are constant.

12.5.3 Results

In this Section a comparison between one way simulation and "hybrid" two way simulation results is performed. In Figure 12.47 the time history of the flow rate applied at the runner inlet of the HD model is plotted.

At these resonance conditions the flow rate at the inlet runner experiences fluctuations of 1% of the mean flow rate. The aim is to assess if these fluctuations applied to the HD model modify the identification of the HA parameters. The pressure fluctuations frequencies in the hydraulic system are represented in Figure 12.48 and compared between one way and two way simulations. In both cases, the maximum amplitude of pressure fluctuations is experienced in the middle of the hydraulic system with about 8% of the turbine head, see Figure 12.49. Finally, in Figure 12.50 the momentum source and the wave speed parameter derived from the HD model in the fifth control volume are compared between one way and two way simulations. The parameters are slightly modified by the inlet flow rate fluctuations. With this hydraulic layout and these cavitation conditions, high HA flow rate fluctuations combined with low HA pressure fluctuations inside the draft tube are experienced but they are not sufficient to influence the HA draft tube model parameters. However, the configuration with the hydraulic system used in Section 12.3 would be interested since high HA pressure fluctuations are experienced in the draft tube even if flow rate fluctuations at the runner inlet are negligible. Hence, the coupling strategy with the exchange of the flow rate at the turbine inlet is not appropriate for this hydraulic layout. In that case, the idea would be to impose the HA pressure fluctuations to the HD model which would be feasible only if the HD model is compressible.

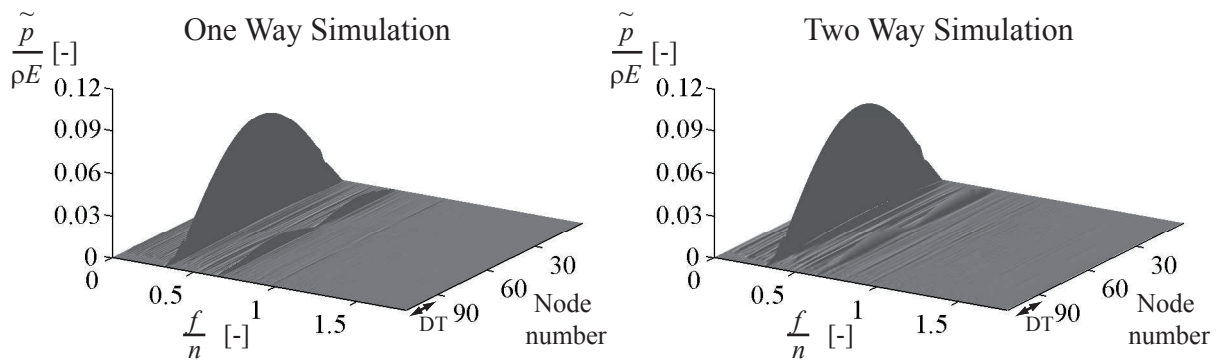


Figure 12.48: Comparison of pressure fluctuations in the whole hydraulic system between one way (left) and two way (right) simulations

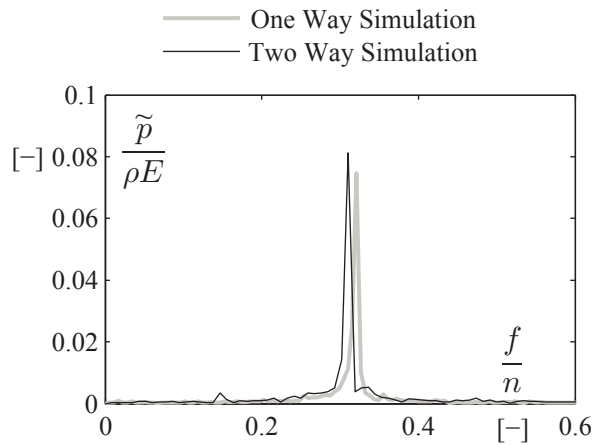


Figure 12.49: Comparison of amplitude spectra pressure fluctuations at the middle of the hydraulic system between one way and two way simulations

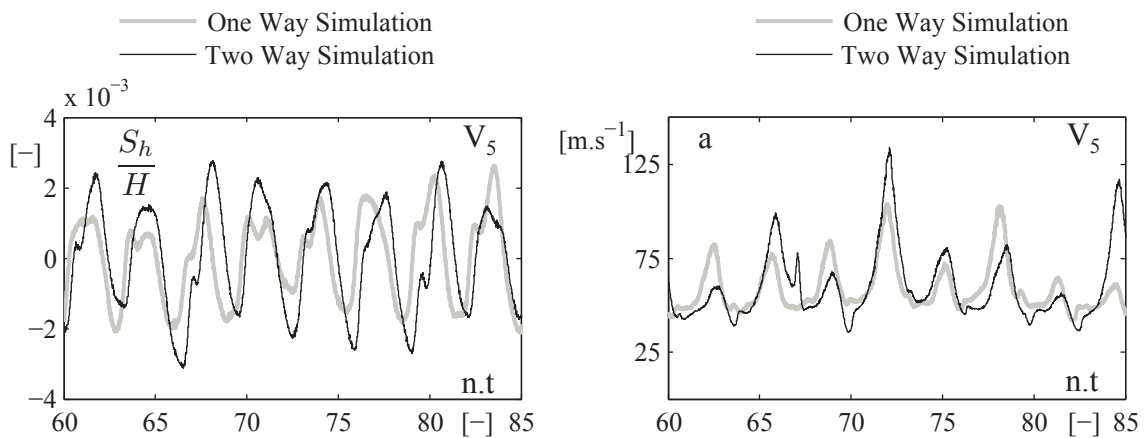


Figure 12.50: Time history comparison of the momentum source (left) and the wave speed parameter (right) in the fifth control volume

Part IV

Full Load Operating Conditions

Chapter 13

Case Study

13.1 MICA Hydroelectric Powerplant

Commissioned in 1970's, the Mica powerhouse features four existing 435MW generating units, each equipped with a Francis type turbine rated at power output of 443.7 MW under the 170.7 m rated net head, . Two additional units are planned to be installed at Mica power plant in the future. Each existing unit is supplied by individual power conduits including intake, penstock and draft tube. Units 1, 2 and 3 share a common tailrace tunnel (i.e. free surface flow) while Unit 4 and two future units share another common tailrace tunnel. The length of each penstock is about 310 meters and the tailrace tunnel each is about 425 meters long. An overview of the hydraulic layout of the Mica power plant is shown in Figure 13.1.

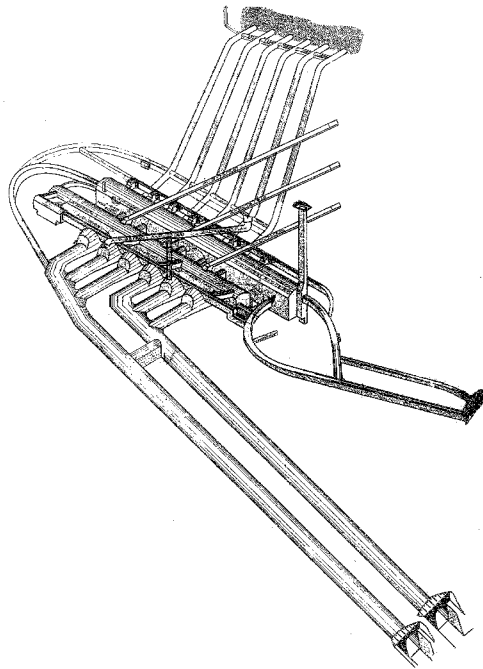


Figure 13.1: Layout of the MICA power plant

Table 13.1: Surging scenario

Unit N° [–]	Gate [%]	Unit output power [MW]
1	100	466±29
2	58	269
3	53	294
4	Down	Down

13.2 Phenomenon of Interest

Pressure and power fluctuations are experienced when three out of four Mica units are operated simultaneously. The surging scenario given in Table 13.1 corresponds to Unit 1 at full load; Unit 4 shutdown and both Unit 2 and Unit 3 operated near their best efficiency points. Under these operating conditions, Unit 1 was the only unit which experienced high power swings and high pressure fluctuations in the penstock and draft tube. Site measurements were performed to provide automatic data acquisition to record the surging. The measured frequency of Mica Unit 1 full load instability was 0.46 Hz. In order to decrease these pressure fluctuations, a prototype air admission valve was designed, fabricated and installed on Unit 1. Despite the installation of this device, instability remained: air flow rate, air pressure and diaphragm displacement were measured to confirm the full load instability frequency of 0.46 Hz.

13.3 Objectives

To analyze and predict this full load instability on prototype, experimental investigations have been carried out on the reduced scale model. The instability was reproduced on the test rig which allowed as a first step to validate the procedure to compute the HA draft tube model parameters of the reduced scale model, see Section 15.2. Then, in Section 15.4 time domain simulation of the instability occurring on the test rig is performed and compared with measurements. Finally, transposition rules of the draft tube model parameters are setup in Section 15.5 to predict the prototype instability.

Chapter 14

Experimental Investigations

14.1 EPFL Experimental Validation Facilities

Three test rigs at the EPFL Laboratory for Hydraulic Machines are available to test reduced scale model which maximum output power can reach 300 *kW*, see Figure 14.1. The test rig satisfies the IEC 60193 Standards allowing to reach an accuracy of 0.5% on the global efficiency for the acceptance tests. The Mica reduced scale model has been installed on the second test rig for which the maximum head, maximum flow rate and maximum rotational speed are respectively equal to 120 *m*, 1.4 $m^3.s^{-1}$ and 2500 *rpm*. One feeding pump of 1000 *kW* output power ensures the flow in the closed loop system. Therefore, the range of operating points is adjusted from the pump head, the flow rate and the rotational speed of the turbine. A cooling system is installed in the closed loop system to keep water temperature constant. Flow rate measurements are performed with an electromagnetic flow meter and differential diaphragm pressure sensors Keller are used to measure the turbine head. A PC manages the program measurements by using both a PGIB link with the acquisition center and a RS232 link with an automaton to drive the whole installation from the PC. Several dynamic pressure sensors were installed on the reduced scale model and measurements were synchronized with a high speed video camera allowing to visualize the behavior of the cavitation volume of the vortex rope in the cone. Figure 14.1 shows the location of the sensors of interest for this analysis:

- #5, #6, #7 and #8 have been located in the same cone cross section with a geometrical phase shift of 90°,
- #10 and #13 are in the alignment of sensor #6 along the draft tube curvilinear abscissa,
- #11 is located upstream to the turbine intake.

For the camera, a resolution of 1024 x 1024 pixels and an acquisition rate of 50 frames/s have been used. Regarding the pressure sensors, measurements have been performed with a sampling frequency of 1200 Hz and a sampling number of 2^{17} corresponding to a time acquisition of 109 s.

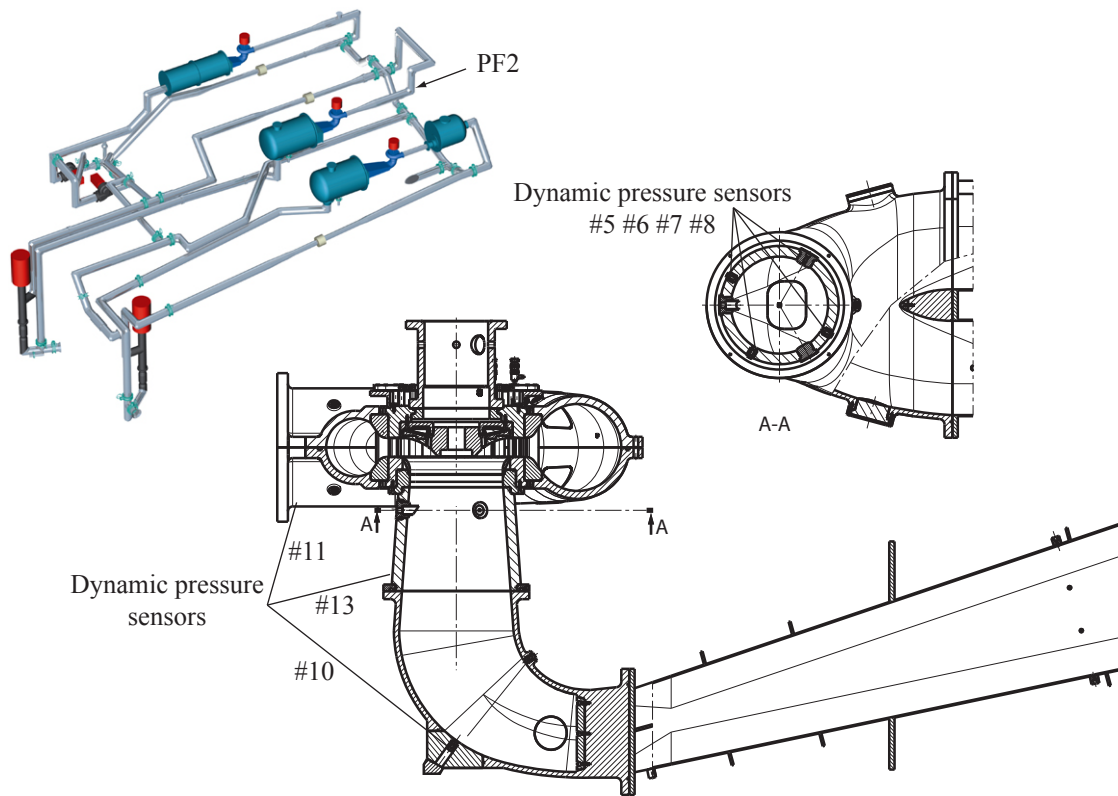


Figure 14.1: Drawing of the reduced scale model and location of dynamic pressure sensors

Table 14.1: Operating points conditions

Operating Point N°	E	Q	N _{ED}	Q _{ED}	T _{ED}	σ	Froude
[—]	[J.kg ⁻¹]	[m ³ .s ⁻¹]	[—]	[—]	[—]	[—]	[—]
OP #1	115.8	0.347	0.275	0.268	0.135	0.11	5.8
OP #2	364.6	0.628					10.3

14.2 Measurements

The presented measurements correspond to an unstable operating point characterized by the onset of vortex rope pulsations at very low frequency. Influence of the Froude number on pressure fluctuations is investigated. This non-dimensional number affects the distribution of cavitation in the flow driving the instability onset, as it determines the pressure gradient relative to the size of the machine. The measurement conditions are summarized in Table 14.1. OP #1 is set up at the Froude similitude to overcome scale effects on the vortex rope cavitation volume regarding transposition from the reduced scale model to the prototype. On the other hand, a higher Froude number is investigated for OP #2 inducing a higher time averaged cavitation volume. In both cases, the Thoma number is set up according to the machine setting level of the power plant. Under these operating conditions, cavitation volume pulsations are experienced as it is shown in Figure

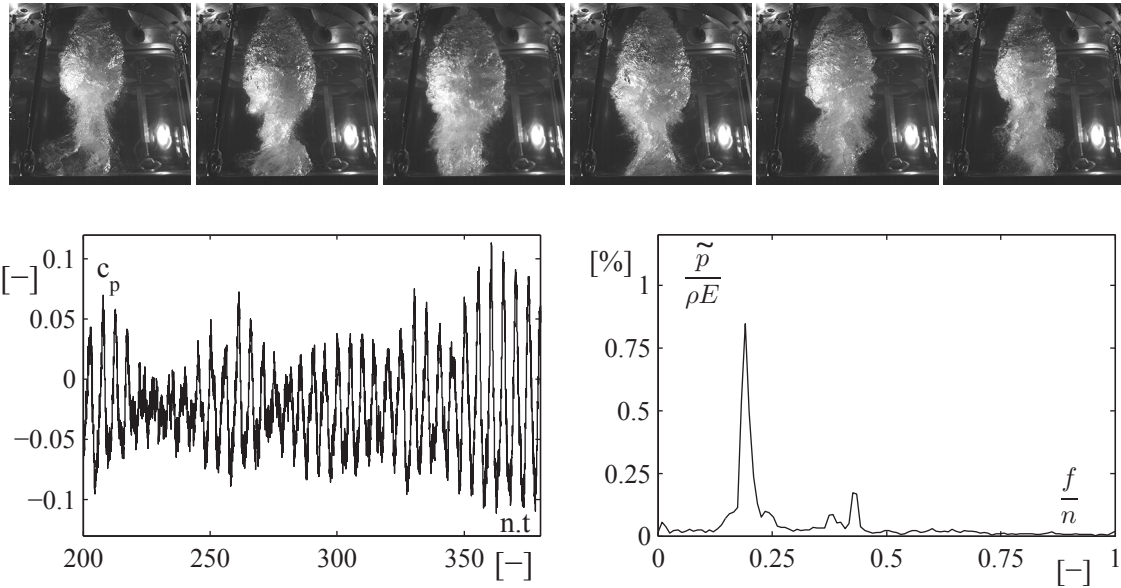


Figure 14.2: OP #1: Cavitation volume pulsation (top), time history (bottom left) and amplitude spectrum (bottom right) of pressure fluctuations in the cone measured at sensor #6

14.2 and Figure 14.3 respectively for Froude numbers $Fr_{OP\#1} = 5.8$ and $Fr_{OP\#2} = 10.3$. More than cavitation volume pulsations, time history and amplitude spectrum of pressure fluctuations are plotted in Figure 14.2 and Figure 14.3. One can observe that for the low Froude number $Fr_{OP\#1} = 5.8$ the amplitude of the rope pulsation is smaller than the high value of Froude number. This is confirmed by the amplitude of pressure fluctuations in the time history and the amplitude spectrum. Moreover, cavity pulsations at the OP #1 are intermittent yielding to the modulation observed in the time history, see Figure 14.2. The stable phase is synchronized with low pressure fluctuations level as observed in Figure 14.2 near the time corresponding to the 230th runner revolution for instance. Therefore the OP #1 is considered at the limit of instability whereas OP #2 is continuously unstable. The fundamental instability frequency of pressure signals, corresponding to the vortex rope volume pulsations observed with the high speed camera, changes as function of the Froude number:

- $f_{OP\#1} = 0.19n = 1.61 \text{ Hz}$ for $Fr_{OP\#1} = 5.8$,
- $f_{OP\#2} = 0.17n = 2.49 \text{ Hz}$ for $Fr_{OP\#2} = 10.3$.

In the case of the high Froude number value, the amplitude spectrum of the pressure signal exhibits all the harmonics of the fundamental, while for the low Froude number value only the second harmonic is visible at $f = 0.38n = 3.22 \text{ Hz}$. Moreover, for the later case, a third frequency at $f = 0.43n = 3.59 \text{ Hz}$ is contained in the amplitude spectrum of pressure fluctuations. Pressure fluctuations of the three remaining sensors located in the same cross section are analyzed in Figure 14.4 with the help of the spectral density S_{xy} and the coherence function C_{xy} . For the two investigated operating points, the fundamental frequency and the harmonics are highlighted by the spectral density with a maximum

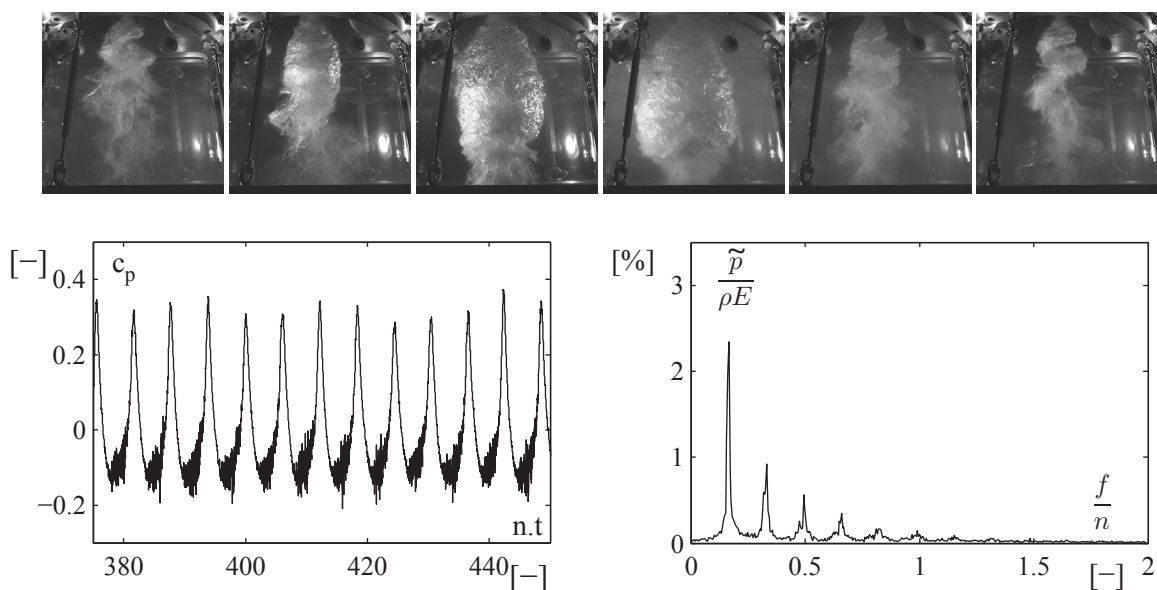


Figure 14.3: OP #2: Cavitation volume pulsation (top), time history (bottom left) and amplitude spectrum (bottom right) of pressure fluctuations in the cone measured at sensor #6

energy transfer given by the coherence. Moreover, the argument of the spectral density gives the phase for each frequency between the sensor signals. It can be concluded that at the fundamental frequency all the sensors located in the same cone cross section are in phase. Therefore, the observed phenomenon is an interaction between the cavitation volume and a standing HA plane wave. These pressure fluctuations are measured in the whole draft tube as shown in Figure 14.5 but also at the turbine intake which proves that these frequencies are related to a standing HA plane wave and not to pressure fluctuations induced by the local flow in the draft tube.

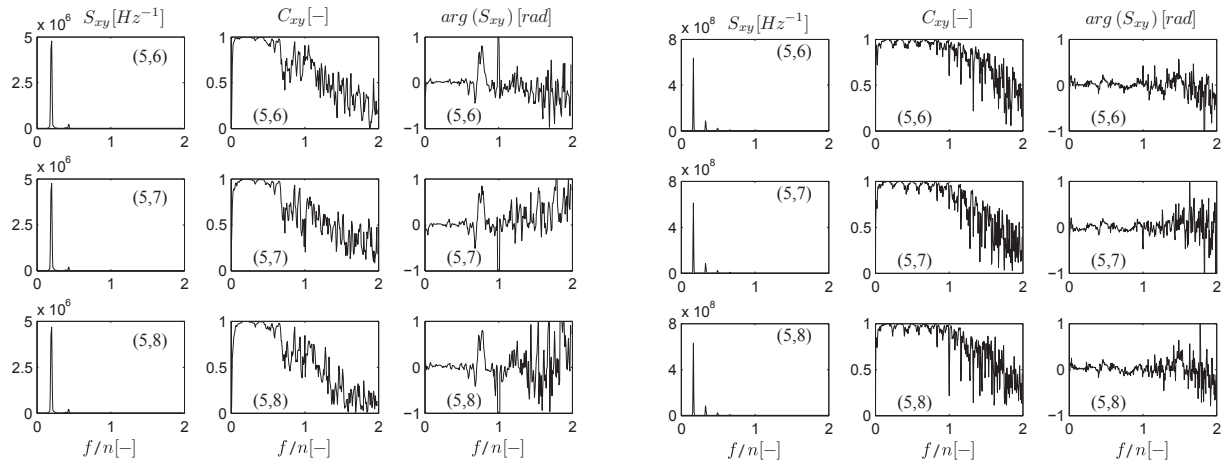


Figure 14.4: Phase analysis of pressure fluctuations in the cone cross section for OP#1 (left) and OP#2 (right)

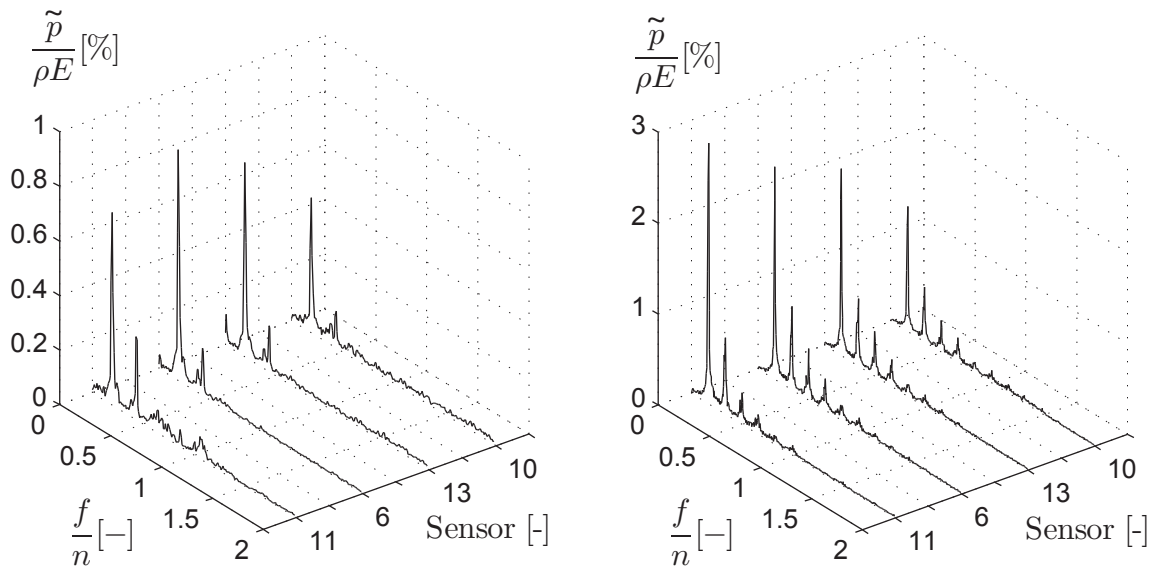


Figure 14.5: Waterfall diagram of pressure fluctuations at the turbine intake (sensor #11) and in the draft tube (sensors #6, #13, #10) for OP#1 (left) and OP#2 (right)

Chapter 15

Numerical Investigations

15.1 The 3D HD model

15.1.1 Setup

Numerical simulations of the three dimensional flow in the draft tube, with the commercial code ANSYS CFX 11.0 have been performed to derive the HA draft tube model parameters. This software, based on finite volume methods, solves the incompressible steady Reynolds Average Navier-Stokes equations in their conservative form by considering single phase simulations. The set of equations is closed with a two-equation turbulence model, the Shear Stress Transport, see Menter [64]. The computational domain is the complete machine consisting of the spiral case, the stay vanes, the guide vanes, the runner and the draft tube, see Figure 15.1. The rotating part containing the runner features two

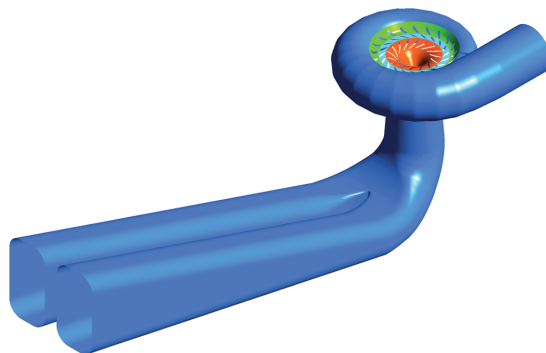


Figure 15.1: Computational domain of the MICA reduced scale model

interfaces "Frozen Rotor" with the stationary parts such as the guide vane row and the draft tube. The computational domain is discretized with a structured mesh of 6 million nodes carried out with ANSYS ICEM 11.0. The boundary conditions are a prescribed flow rate at the spiral case inlet and an opening condition with "static pressure for entrainment" at the draft tube outlet set to 0 Pa. To derive the numerical pressure field p^{num} corresponding to the investigated Thoma number, a post processing correction is applied as follow:

$$p = p^{num} - \rho g Z + p^{offset} \quad (15.1)$$

The hydrostatic contribution is taken into account which could be decisive for prototype computations. Moreover, this offset is determined from the draft tube outlet static pressure derived from the Thoma number definition:

$$p^{offset} = \rho\sigma E + p_v + \rho g Z_{ref} - \rho \frac{Q^2}{2A_I^2} \quad (15.2)$$

Hence this post-processing correction of the numerical pressure field allows to perform only one computation to derive the cavitation volume for different Thoma number values. Once this correction is performed, the vortex rope cavitation volume is assumed to correspond to the flow region bounded by the vapour pressure p_v set to 2338 Pa at 20°C.

15.1.2 Simulation Results

In Figure 15.2, the obtained steady axi-symmetric vortex rope is shown for the two investigated operating points. At *OP#2*, the cavitation volume is higher than for the *OP#1* due to the higher Froude number. This result is in good agreement with the visualizations shown respectively for *OP#1* and *OP#2* in Figure 14.2 and Figure 14.3. Moreover, the vortex rope shape seems to be well predicted especially for the upper part where the density of the mixture water-vapor is the highest. However, the lower part where the mixture of the tip vortex is diffuse, the shape is not reproduced by the single phase simulation. It has been shown by Flemming et al. [37] that two phase simulations would allow to predict this diffusive lower part of the cavitation volume. To derive the HA draft

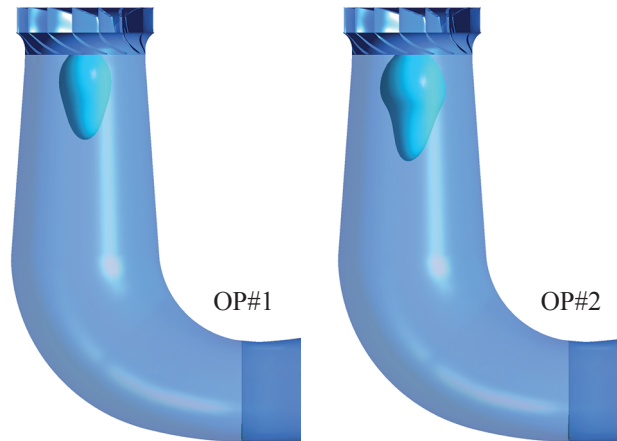


Figure 15.2: Numerical simulation of the steady vortex rope for the two operating points

tube model parameters, the variation of the cavitation volume as function of the Thoma number is decisive. In Figure 15.3, this variation is plotted for the two operating points of interest. Whatever the Thoma number considered, the cavitation volume of the *OP#2* is always higher. With the same procedure as the one used for the part load conditions the data are fitted with a power law:

$$V_c = a\sigma^b \quad (15.3)$$

In Table 15.1 the coefficients of the power law for the two operating points are given with the fitting coefficients.

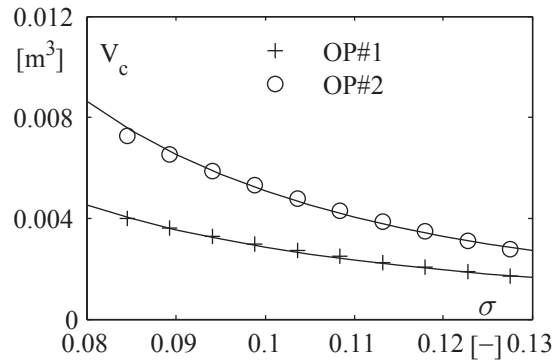


Figure 15.3: Variation of the cavitation volume as function of the Thoma number

Table 15.1: Curve fitting of the steady cavitation volume with the Thoma number

OP	a	b	Fitting coefficient
#1	$2.43 \cdot 10^{-5}$	-2.07	0.997
#2	$2.13 \cdot 10^{-5}$	-2.38	0.994

15.2 Identification of HA Draft Tube Model Parameters

15.2.1 Mass Flow Gain Factor

According to Equation 7.47, the mass flow gain factor $\chi_{\bar{2}}$ is defined as the vortex rope cavitation volume variation as function of the downstream flow rate variation $Q_{\bar{2}}$. In the case of single phase simulation, the upstream and the downstream flow rates in the HD model are equal due to the incompressibility of the fluid. Therefore it is assumed that:

$$\chi_{\bar{2}} = -\frac{\partial V_c}{\partial Q_{\bar{2}}} \approx -\frac{\partial V_c}{\partial Q_{\bar{1}}} \quad (15.4)$$

To derive this parameter, three flow numerical simulations are performed with the same outlet pressure reference set to 0 Pa. However three inlet flow rates are specified: the nominal flow rate Q_n corresponding to the operating point which is compared to a higher and lower flow rate difference of 5%. This methodology is applied for the two operating points and the evolution of the cavitation volume as function of the Thoma number is shown in Figure 15.4. For each Thoma number, the central finite difference approximation of the cavitation volume over the flow rate leads to the evolution of the mass flow gain factor parameter as function of the Thoma number, see Figure 15.5. The variation law is quite linear and the mass flow gain factor value derived for *OP#1* is lower than for *OP#2* for every Thoma number value in the plotted range. At the investigated Thoma number value of $\sigma = 0.11$, the computed mass flow gain factor parameters are given in Table 15.2.

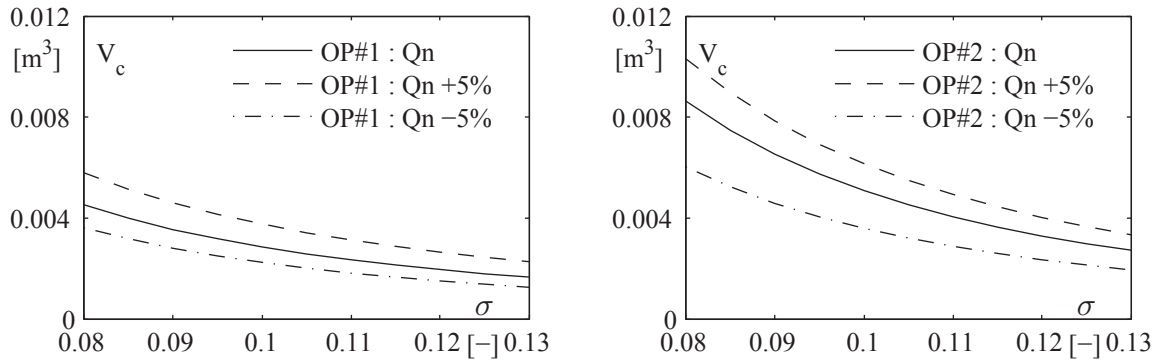


Figure 15.4: Variation of the cavitation volume for $OP\#1$ (left) and $OP\#2$ (right) as function of the Thoma number for three specified inlet flow rates

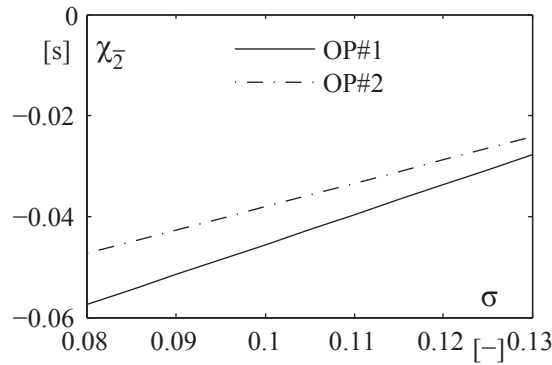


Figure 15.5: Variation of the mass flow gain factor as function of the Thoma number

15.2.2 Cavitation Compliance

A central finite difference approximation of the cavitation volume over the Thoma number gives the cavitation compliance as function of the Thoma number. Then the equivalent compliance taking into account the effect of the wall compliance is computed according to Equation 10.17. The variation law of this equivalent compliance is plotted in Figure 15.6 with the corresponding wave speed parameter. At the investigated Thoma number value of $\sigma = 0.11$, the computed equivalent compliance and wave speed parameters are given in Table 15.3. One can observe that the wave speed derived for $OP\#2$ is higher than $OP\#1$ although the cavitation volume is higher. This result could be surprising since at a first

Table 15.2: Mass flow gain factors at the investigated Thoma number value of $\sigma = 0.11$

OP	χ_2
[-]	[s]
#1	-0.039
#2	-0.033

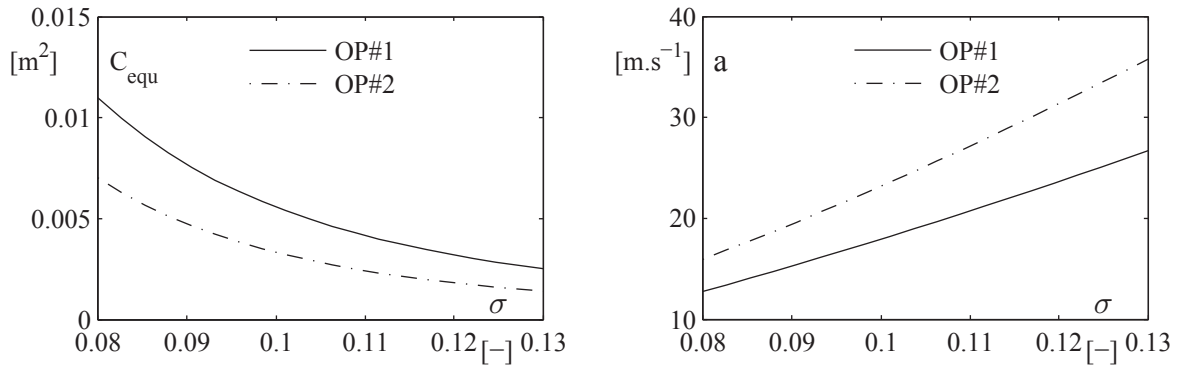


Figure 15.6: Variation of the equivalent compliance (left) and the wave speed (right) parameters as function of the Thoma number

Table 15.3: Equivalent compliance and wave speed parameters at the investigated Thoma number value of $\sigma = 0.11$

OP	C_{equ}	a
[-]	$[m^2]$	$[m.s^{-1}]$
#1	$4.1 \cdot 10^{-3}$	20.8
#2	$2.4 \cdot 10^{-3}$	27.4

approach, we assume that if there is more cavitation, the wave speed would be lower. However, the pressure dependency of the wave speed explains this behavior. Indeed, the increase of the Froude number induces an increase of the mean pressure level in the draft tube which at its turn increases the wave speed. To highlight this pressure dependency, the wave speed has been computed from the analytical model in the same way as the part load conditions according to Equation 12.11. The pressure is considered at the outlet of the HD model. The obtained analytical wave speeds values are 22.9 m.s^{-1} and 29 m.s^{-1} respectively for operating points *OP#1* and *OP#2*. Hence, the same tendency is observed due to the pressure dependency.

15.2.3 Thermodynamic Damping

The last HA parameter to derive from the HD model is the thermodynamic damping μ'' . This parameter models the energy dissipation in unsteady cavitating flows due to a combination between the gas release and the heat exchange between the gas and the surrounding liquid. Considering both effects and assuming an homogeneous bubbly cavitation in the pipe cross section, Pezzinga developed an analytical formulation for the second viscosity according to Equation 7.46. Obviously, vortex rope volume at full load conditions is far from the assumption of an homogeneous cavitation development in the pipe. However, this parameter being unknown for the vortex rope model, this formulation is considered as a first approximation to get an order of magnitude of this parameter. To derive this parameter from the HD model, the same methodology as for the part load

Table 15.4: Thermodynamic damping at the investigated Thoma number value of $\sigma = 0.11$

OP	μ''
[-]	[Pa.s]
#1	2744
#2	1555

conditions is used. The pressure is considered at the outlet of the HD model whereas the wave speed and the cavitation volume have been computed previously. By applying the formula for the two investigated operating points the obtained thermodynamic dampings are given in Table 15.4.

15.3 Validation of HA Draft Tube Model Parameters

A set of HA parameters have been derived from the HD model for the two operating points considered at the Thoma number value of $\sigma = 0.11$. The HA model of the complete test rig including the draft tube component set with the above HA parameters is developed with the SIMSEN software. Hence, a small perturbation stability analysis of the reduced scale model installed on the test rig can be performed by computing eigenvalues and eigenvectors of the complete hydraulic system. In Figure 15.7, the first four eigenvalues are plotted in the complex plan where the x-axis corresponds to the modal damping and the y axis to the modal frequency.

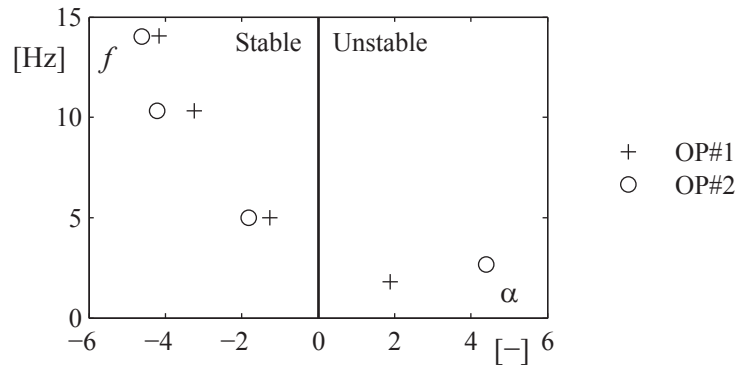


Figure 15.7: Eigenvalues in the complex plan of the 1D HA model set up with the HA parameters derived from the 3D HD model

For the both investigated operating points, the unstable eigenmode corresponding to a positive modal damping, is the first eigenmode which frequency is 1.8 Hz and 2.7 Hz respectively for $OP\#1$ and $OP\#2$. Therefore, using the HA parameters derived from the HD model, the unstable frequency of the vortex rope pulsation is predicted with an error of 11% and 8% according to the experimental frequency value of 1.61 Hz and 2.49 Hz respectively for $OP\#1$ and $OP\#2$. Moreover, it has been observed experimentally that the $OP\#2$ is much more unstable than $OP\#1$ which is assumed to be at the limit

of the stability. This experimental observation is confirmed by the modal damping of the unstable eigenmode. Indeed, the damping of $OP\#1$ is nearer to the stability limit than $OP\#2$. However, this prediction from the small perturbation stability analysis does not allow to predict that the instability would occur by intermittence. It can be just concluded that $OP\#2$ is more unstable than $OP\#1$. This unstable eigenmode is plotted in Figure 15.8.

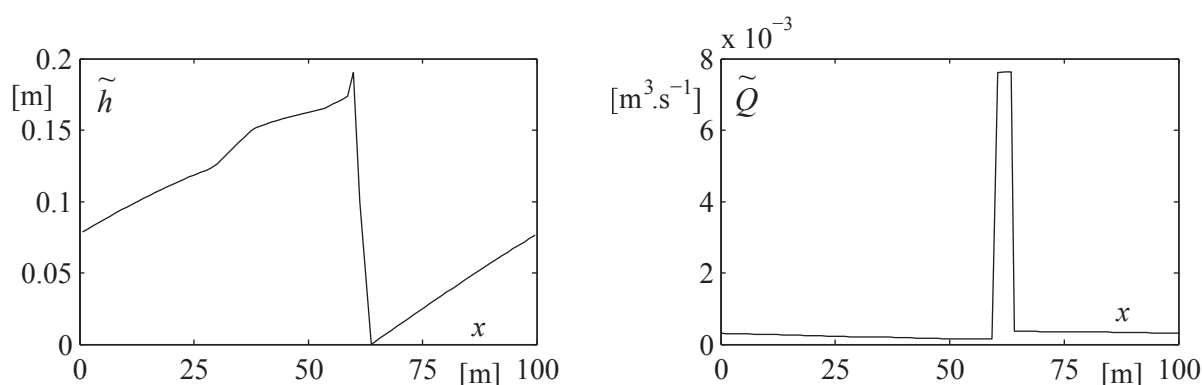


Figure 15.8: Shape of the first unstable eigenmode: pressure (left) and flow rate (right) fluctuations

The x axis is the abscissa representing the location in the test rig. Being a closed loop system, abscissa $x = 0\text{m}$ and $x = 100\text{m}$ correspond to the same location, being the feeding pump location. The draft tube component is defined from the runner outlet location at $x = 59\text{m}$ to the downstream reservoir location at $x = 64\text{m}$. One can observe that the standing wave in the test rig, features large flow rate fluctuations Q_2 downstream the cavity due to the large cavitation compliance compared to the pipes. The linearization of the set of differential equations allows to identify the system stability and predicts system eigenfrequencies and related mode shapes. However, this method does not give any information about the amplitude of the oscillations. Indeed, this linear theory only predicts that the amplitudes of the eigenmode fluctuations given in Figure 15.8 grow exponentially in time according to the modal damping given in Figure 15.7. In the next Section, the aim is to simulate in the time domain, pressure and flow rate fluctuations of the standing wave which should grow exponentially until a maximum, called a "limit cycle".

15.4 Full Load Instability Simulation

This Section is aiming to predict and simulate the instability phenomenon with its corresponding limit cycle. In 2006, Koutnik et al. [56] performed a time domain simulation of a self excitation occurring in a four 400MW Francis Pumped-Storage plant. In order to obtain finite fluctuations called "limit cycle", nonlinearity on the cavitation compliance as function of the Thoma number is introduced. Moreover, the system is pushed to the limit of the instability by setting a mass flow gain factor parameter very low compared to the one derived from the HD model according to the same methodology as the one described in Section 15.2. Hence, during the transient simulation, the hydraulic system

enters in unstable conditions and nonlinearity of the compliance switches between stable and unstable conditions allowing to reach the limit cycle. It has been shown by authors that limit cycle is reachable only if nonlinearity of HA parameters is taken into account.

To validate the influence of the nonlinearity it is chosen to simulate the instability observed for the *OP#2*. In the mechanical field, the best known mechanism of self oscillation excitation is so called negative friction [60]. Considering a spring-mass system with a damper in parallel, the self oscillation mechanism is driven by a linear equation of the following form:

$$m \cdot \ddot{x} + c \cdot \dot{x} + k \cdot x = 0 \quad (15.5)$$

When the damping c is negative, instead of energy being lost due to the friction, energy is generated within the system. A slight disturbance from equilibrium leads to the system being carried far from the equilibrium state without reaching a limit cycle. However, if a nonlinear damping is introduced the limit cycle is reachable. The well known mechanical system is the Kaidanovsky-Khaikin frictional model [60] [63] which consists of a mass fixed to a wall by a spring and lying over a transmission belt moving with a given velocity. The nonlinear dry friction force on the belt can under certain conditions induce negative friction.

Inspired by these mechanical models, the nonlinearity of the thermodynamic damping is introduced to reach the limit cycle and combined with nonlinearity of the cavitation compliance parameter as already performed by Koutnik et al. [56].

15.4.1 Calibration of the Thermodynamic Damping

The nonlinearity of the thermodynamic damping is assumed to be due to the pressure state variable only. As a first approach, the nonlinearity of the thermodynamic damping has been derived from a combination of the Pezzinga's analytical formulation with the variation laws of the wave speed and the cavitation volume as function of the pressure derived from the HD model in Section 15.2.

The resulting variation law of the thermodynamic damping based on the HD model nonlinearities is called afterwards HydroDynamic Law (HDL). However, using this HDL, the hydraulic system does not reach a physical limit cycle in the time domain simulation: pressure and flow rate fluctuations diverge. As conclusion, the nonlinearity introduced by the thermodynamic damping is not high enough to reach the limit cycle.

The global variation of the HDL is compared to another variation law called afterwards Perfect Gas Law (PGL) which corresponds to the Pezzinga's analytical formulation given in Equation 7.46 applied to an ideal gas model. The state equation of an ideal gas being:

$$p \cdot V_c = n \cdot R \cdot T \quad (15.6)$$

the gas fraction β and the wave speed a can be modeled by the following relations:

$$\beta = \frac{K_1}{p} \quad C_c = -\rho g \frac{\partial V_c}{\partial p} \Rightarrow a^4 = K_2 p^4 \quad (15.7)$$

Replacing these equations in Equation 7.46 it yields to the following expression for the thermodynamic damping applied to a perfect gas:

$$\mu'' = \Theta \cdot \rho_c \cdot R \cdot T \cdot K_2 \cdot \left(K_1^3 \cdot \frac{(\rho_c - \rho)^2}{p} + K_1 \cdot \rho^2 \cdot p + 2 \cdot K_1^2 \cdot \rho \cdot (\rho_c - \rho) \right) \quad (15.8)$$

The constants K_1 and K_2 are determined to fit the wave speed and the thermodynamic damping at a target pressure equal to the pressure derived from the Thoma number definition. For the investigated Thoma number value of $\sigma = 0.11$ the target pressure corresponds to $h_{target} = 4.44$ m. K_2 is determined by the wave speed value of $27.4 \text{ m}\cdot\text{s}^{-1}$ and K_1 is the solution of the cubic polynomial to get the target thermodynamic damping value of $1555 \text{ Pa}\cdot\text{s}$. In Figure 15.9, the variation laws of the thermodynamic damping are compared between the HDL and the PGL.

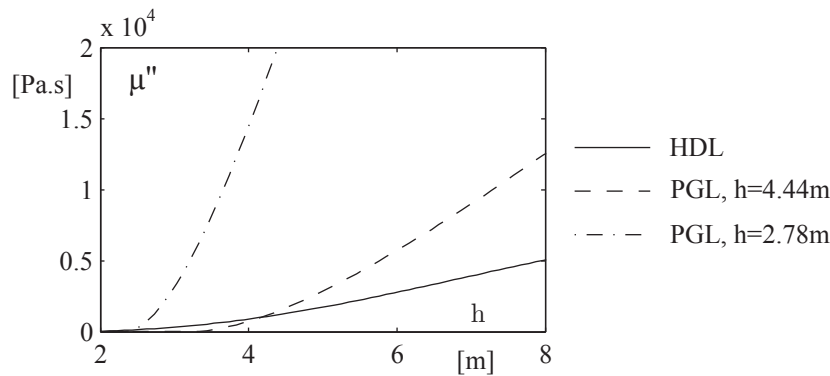


Figure 15.9: Comparison of the HydroDynamic variation Law (HDL) with the Perfect Gas variation Law (PGL) fitted for two target pressure values

The PGL fitted for the target pressure value of $h_{target} = 4.44$ m has a variation much higher than the HDL. The thermodynamic damping reaches the zero value when the cone and the elbow parts are filled entirely with gas. Hence, it can be observed that this phenomenon appears for a pressure higher than the vapor pressure of $h_v = 2.28$ m. It is decided that the zero value must be reached at the vapor pressure. Hence a new PGL is fitted on a lower target pressure value of $h_{target} = 2.78$ m plotted in Figure 15.9. This new fitting leads to a PGL which variation as function of pressure is much higher, being able to dissipate more to reach the limit cycle. For all the above cases, the variation laws are monotonically increasing with the pressure. However, the using of the PGL fitted for the target pressure value of $h_{target} = 2.78$ m does not induce still enough dissipation to reach the limit cycle obtained experimentally. Hence it is proposed to increase the slope of the variation law at the same target pressure value of $h_{target} = 2.78$ m. The used methodology is to find a new set of constants K_1 and K_2 which satisfy both target thermodynamic damping value of $1555 \text{ Pa}\cdot\text{s}$ and target slope of the variation law. Hence, K_1 and K_2 are two unknowns which are solution of the following set of equations:

$$\begin{cases} K_1^3 \cdot K_2 \cdot \frac{(\rho_c - \rho)^2}{p} + K_1 \cdot K_2 \cdot \rho^2 \cdot p + 2 \cdot K_1^2 \cdot K_2 \cdot \rho \cdot (\rho_c - \rho) - \frac{\mu''}{\Theta \cdot \rho_c \cdot R \cdot T} = 0 \\ -K_1^3 \cdot K_2 \cdot \frac{(\rho_c - \rho)^2}{p^2} + K_1 \cdot K_2 \cdot \rho^2 - \frac{1}{\Theta \cdot \rho_c \cdot R \cdot T} \cdot \frac{d\mu''}{dp} = 0 \end{cases} \quad (15.9)$$

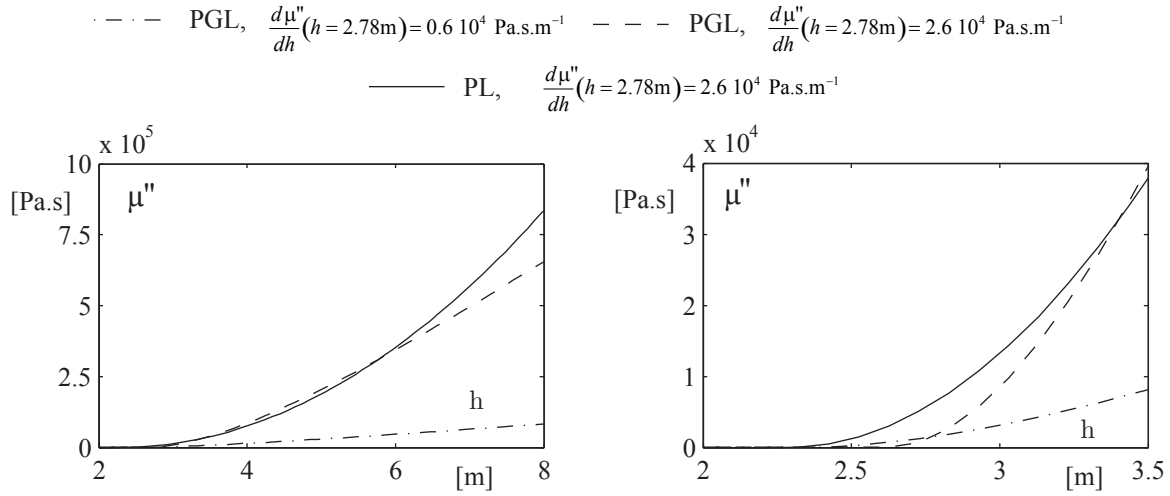


Figure 15.10: Comparison of the Parabolic variation Law (PL) with the Perfect Gas variation Laws (PGL)

In Figure 15.10, PGL featuring a higher slope is compared to the reference PGL obtained previously. In the left part of the figure, the variation laws are plotted for a pressure range from 2 m to 8 m whereas on the right part, a zoom around the target pressure value of $h_{target} = 2.78$ m is shown. The dissipation induced by the PGL featuring a higher slope is efficient when pressure increases. However, when pressure reaches low pressure values, the parameter decreases quickly to a zero value which avoids the system to reach the limit cycle. Finally, the variation law must respect two fundamental characteristics: a high slope to be dissipative when pressure increases and a progressive decrease to the zero value. To answer to these two characteristics, a Parabolic variation Law (PL) is set to fit time domain simulations with measurements by specifying the same slope as the PGL at the target pressure value of $h_{target} = 2.78$ m. This condition leads to a PL which satisfies a thermodynamic damping value of 6375 Pa.s instead of 1555 Pa.s at the target pressure value. As it will be shown in the next Section, this Parabolic variation Law allows to simulate the limit cycle according to experiments. Obviously, this result does not confirm that this variation law is the real one. Indeed it has been derived empirically to show that the nonlinearity of this parameter is decisive to reach the limit cycle. Further investigations must be carried out to derive properly an analytical formulation of this parameter applied to an axi-symmetric cavitating vortex rope.

15.4.2 Nonlinear Time Domain Simulation

Time domain simulation of the *OP#2* full load instability is performed with constant and nonlinear HA draft tube model parameters. Regarding the simulation with constant parameters, the mass flow gain factor and the wave speed are set up respectively according to Table 15.2 and Table 15.3. Moreover, the thermodynamic damping value is derived from the calibrated Parabolic variation Law (PL) considered at the target pressure value of $h_{target} = 2.78$ m being the initial pressure condition in the draft tube. For the simulation with nonlinear parameters, the mass flow gain factor is kept constant, the wave speed

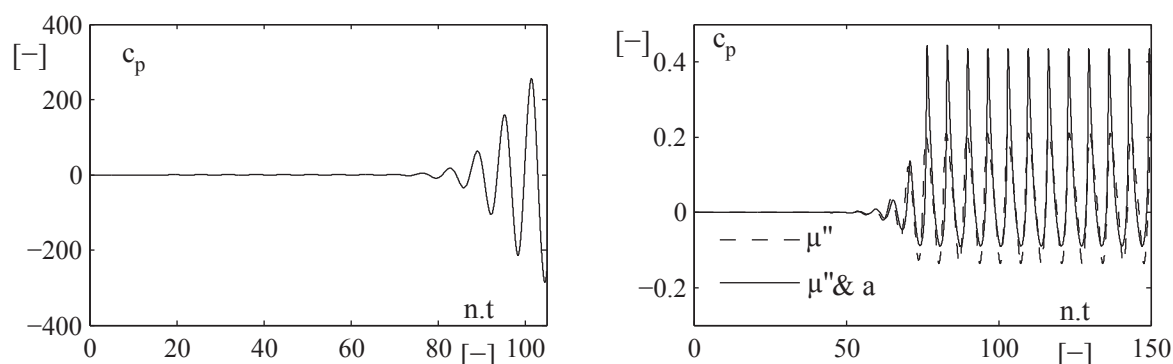


Figure 15.11: Time history of pressure fluctuations in the draft tube with constant (left) and nonlinear (right) HA draft tube model parameters

variation law is the one given in Section 15.2.2 and the thermodynamic damping variation law is the Parabolic Law derived in Section 15.4.1.

A comparison of the pressure coefficient fluctuations between simulations with constant and nonlinear HA parameters is given in Figure 15.11. In the case of constant HA parameters, simulation is divergent which induces very high pressure fluctuations without reaching the limit cycle. However, in accordance with the eigenvalue analysis, the simulated unstable frequency is $f = 2.7$ Hz. In the right part of Figure 15.11, influence of nonlinearity of each parameter on the time domain simulation is investigated by comparing pressure fluctuations with and without wave speed nonlinearity. The introduction of a nonlinear thermodynamic damping allows to reach the limit cycle. However, pressure fluctuations keep sinusoidal shape whereas experimental data feature higher number of harmonics due to the "overshoots". By including the nonlinearity of the wave speed, the typical researched shape is obtained and the unstable frequency is conserved.

The upstream and downstream flow rates to the cavitation volume, respectively Q_1 and Q_2 , experience fluctuations which are plotted in Figure 15.12. It shows that during the instability, cavitation volume pulsation is due to a downstream mass water oscillation between the draft tube and the downstream tank. When the vortex rope volume increases,

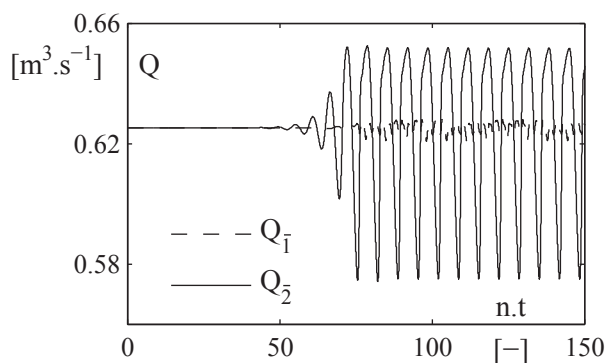


Figure 15.12: Time history of the upstream Q_1 and downstream Q_2 flow rates of the cavitation volume

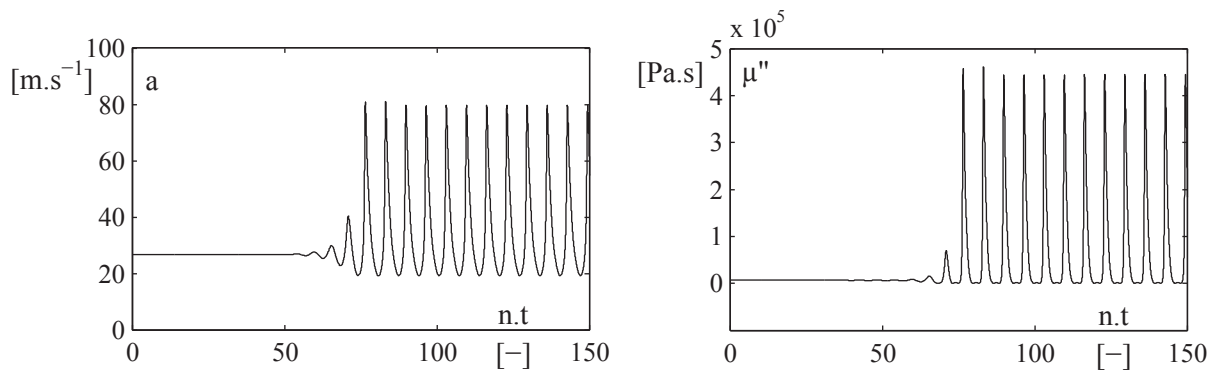


Figure 15.13: Time history of the wave speed (left) and the thermodynamic damping (right) fluctuations

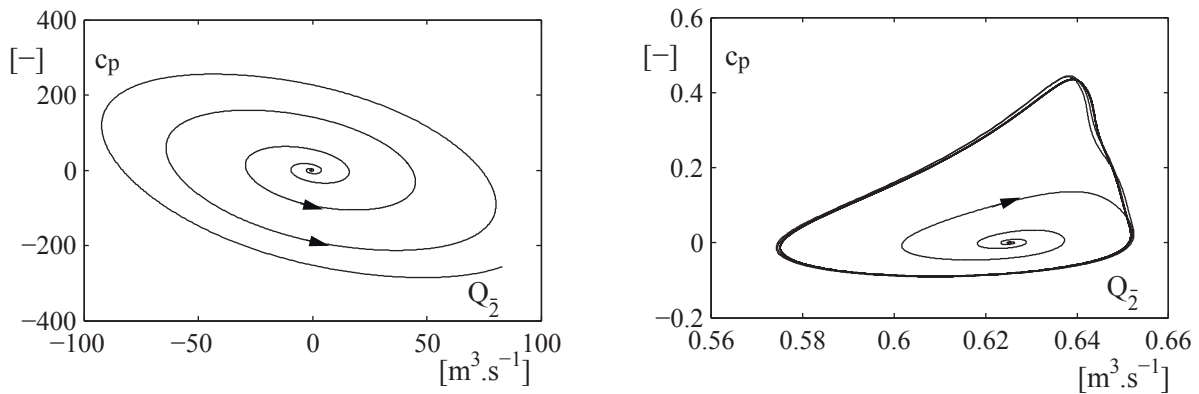


Figure 15.14: Phase plane diagram for constant (left) and nonlinear (right) HA draft tube model parameters

the downstream flow rate increases and vice versa. Moreover, this cavitation volume fluctuation induces implicitly wave speed and thermodynamic damping fluctuations which increase dramatically the energy dissipation of the system allowing to reach the limit cycle, see Figure 15.13.

15.4.3 Energy Balance

In the field of mechanical oscillations, a typical representation, called the "phase plane", is extensively used to obtain properties of the differential equations such as equilibrium, periodicity or stability. Usually, for hydroacoustic systems, the phase plane represents the pressure as function of the flow rate [23] and the resulting curve is called the phase path.

In Figure 15.14, pressure as function of the downstream flow rate is plotted for the simulations with constant and nonlinear HA draft tube parameters. By definition, a limit cycle is an isolated periodic solution of the system [53] and is represented in the phase plane by an isolated closed path. During one period T along the closed path, the total

energy of the system ξ returns to its original value, see Equation 15.10.

$$\xi(T) - \xi(0) = 0 \tag{15.10}$$

Hence, at the equilibrium, the energy loss in the system is balanced by the energy gain of the vortex rope excitation. In the following, an energy balance approach is developed to understand this interaction between the excitation source and the dissipation of the circuit during the limit cycle.

The first step is to find a formulation of the total energy ξ of the fluid system as function of the state variables of the equivalent electrical model in SIMSEN. The total energy is constituted of a kinetic energy ξ_k , a potential energy ξ_p and a source energy ξ_s [19]:

$$\xi = \xi_k + \xi_p + \xi_s \tag{15.11}$$

Considering that the equivalent electrical model of the test rig is divided in n meshes, the total energy of the system is the sum of the energies included in each mesh:

$$\xi = \sum_{i=1}^n \xi_i = \sum_{i=1}^n \xi_{k_i} + \sum_{i=1}^n \xi_{p_i} + \sum_{i=1}^n \xi_{s_i} \tag{15.12}$$

In the right part of Figure 15.15 the electrical mesh including the excitation mass source represented by the mass flow gain factor $\chi_{\bar{2}}$ is given, whereas in the left part a standard electrical mesh is shown. In the investigated model, the energy of the excitation source is concentrated in only one mesh represented in the right part of Figure 15.15. During the limit cycle this energy can be expressed as:

$$\xi_s = \rho \cdot g \cdot \chi_{\bar{2}} \cdot Q_{\bar{2}} \cdot h_{\bar{1}+1/2} \tag{15.13}$$

However, for the kinetic and the potential energies, all the meshes must be taken into account. Considering a standard mesh given in Figure 15.15:

$$\begin{cases} \xi_k = \sum_{i=1}^n \xi_{k_i} = \sum_{i=1}^n \left(\frac{1}{2} \cdot \rho \cdot g \cdot L \cdot Q_i^2 \right) \\ \xi_p = \sum_{i=1}^n \xi_{p_i} = \sum_{i=1}^n \left(\int \rho \cdot g \cdot (h_{i-1/2} - h_{i+1/2}) \cdot Q_i \cdot dt \right) \end{cases} \tag{15.14}$$

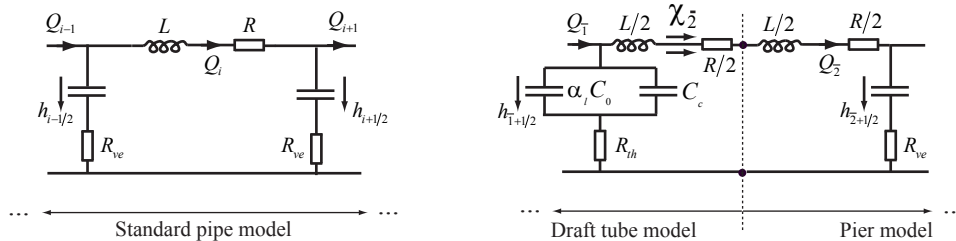


Figure 15.15: Schemes of a standard electrical mesh (left) and electrical mesh including the downstream mass flow gain factor $\chi_{\bar{2}}$ (right)

The second step is to derive the total energy according to the time:

$$\begin{aligned} \frac{d\xi}{dt} &= \sum_{i=1}^n \left(\rho \cdot g \cdot Q_i \cdot \left(L \cdot \frac{dQ_i}{dt} + h_{i-1/2} - h_{i+1/2} \right) \right) \\ &+ \rho \cdot g \cdot \chi_{\bar{2}} \cdot \left(\frac{dQ_{\bar{2}}}{dt} \cdot h_{\bar{1}+1/2} + Q_{\bar{2}} \cdot \frac{dh_{\bar{1}+1/2}}{dt} \right) \end{aligned} \quad (15.15)$$

Using the Kirschoff law applied to the voltages in the standard electrical mesh it yields to:

$$\begin{aligned} L \cdot \frac{dQ_i}{dt} + h_{i+1/2} - h_{i-1/2} &= R_{ve} \cdot (Q_{i-1} - Q_i) - R_{ve} (Q_i - Q_{i+1}) - R \cdot Q_i \\ &= -H_{l_i} \end{aligned} \quad (15.16)$$

Integrating Equation 15.16 in Equation 15.15, the derivative of the total energy can be rewritten as:

$$\begin{aligned} \frac{d\xi}{dt} &= - \sum_{i=1}^n (\rho \cdot g \cdot Q_i \cdot H_{l_i}) + \rho \cdot g \cdot \chi_{\bar{2}} \cdot \left(\frac{dQ_{\bar{2}}}{dt} \cdot h_{\bar{1}+1/2} + Q_{\bar{2}} \cdot \frac{dh_{\bar{1}+1/2}}{dt} \right) \\ &= \left. \frac{d\xi}{dt} \right|_l + \left. \frac{d\xi}{dt} \right|_s \end{aligned} \quad (15.17)$$

Therefore, the variation of the total energy is due to a balance between the lost power $\left. \frac{d\xi}{dt} \right|_l$ in the resistive components of the electrical circuit and the gain power $\left. \frac{d\xi}{dt} \right|_s$ due to the excitation source.

In Figure 15.16, time histories of these two powers are plotted. During one period T , the dissipation can provide energy to the system since the power becomes positive. Hence, in order to balance the total energy, the excitation source dissipates since the power becomes strongly negative. According to Equation 15.10, the total energy returns to its original value during a period T . According to the previous development Equation 15.10 can be rewritten as:

$$\xi(T) - \xi(0) = \int_0^T \frac{d\xi}{dt} \cdot dt = \int_0^T \left. \frac{d\xi}{dt} \right|_l \cdot dt + \int_0^T \left. \frac{d\xi}{dt} \right|_s \cdot dt = 0 \quad (15.18)$$

Integrating numerically the two power curves shown in Figure 15.16 over a period, the equality of Equation 15.18 is confirmed.

In this Section, it has been shown that consideration of constant parameters is useful to perform a stability analysis based on eigenvalues and eigenvectors computation. In that case, this linear method allows to identify the stability of the system and to find out unstable frequencies with mode shapes. However, time domain simulation with constant parameters is divergent without reaching a maximum called the limit cycle. For this reason, nonlinearity of parameters is introduced. It is shown that the essential parameter which allows to reach the limit cycle is the thermodynamic damping. Regarding the nonlinearity of the wave speed, it allows to reproduce the typical shape of the pressure fluctuations measured on the test rig. Amplitude of the limit cycle is in good agreement with experiments since the variation law of the thermodynamic damping has been fitted to obtain this result. Therefore, further investigations must be carried out to derive an analytical model for this key parameter. Moreover, an energy approach during the limit

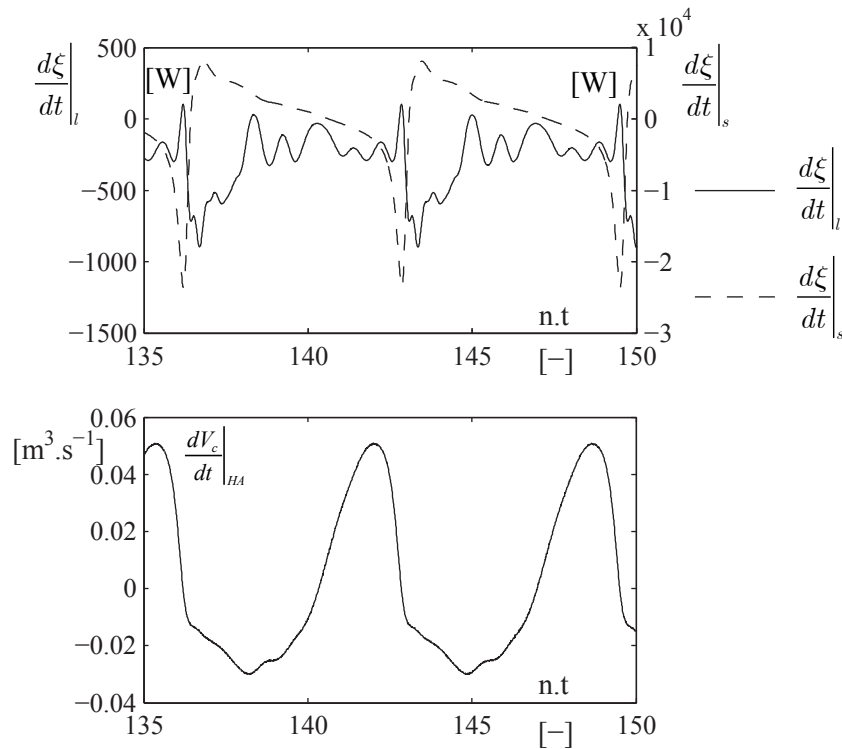


Figure 15.16: Time history of the lost power and the gain power (top) and time history of the cavitation volume fluctuations (bottom)

cycle showed the interaction process between the excitation mass source of the vortex rope and the system dissipation to reach an equilibrium. Indeed, it brings out that over one period, the dissipation can provide energy to the system whereas the mass source dissipates to ensure the equilibrium.

15.5 Prediction of Prototype Instability

To predict the prototype instability from investigations on the reduced scale model, measurements corresponding to the *OP#1* are considered. Indeed, this reduced scale model operating point is carried out at the Froude similitude to overcome scale effects on the vortex rope cavitation volume regarding transposition from the reduced scale model to the prototype. This condition allows defining the specific energy E of the reduced scale model and rotational speed is imposed by the equality of the speed factor N_{ED} between the reduced scale model and the prototype. Finally, the guide vane opening y corresponds to the prototype output power corresponding to the surging scenario given in Table 13.1.

This Section presents the methodology developed to predict the instability on the Mica power plant prototype using both experimental measurements at the *OP#1* and numerical simulations performed on the reduced scale model. The full load HA draft tube model including the thermodynamic damping parameter is used and calibrated for the reduced scale model according to the measurements and experimental observations. Then, transposition laws of the HA parameters are established and stability of the prototype is

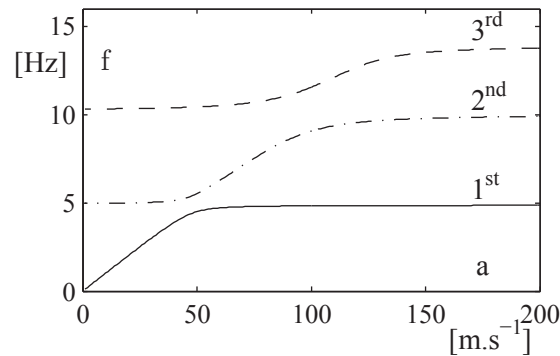


Figure 15.17: Eigenfrequencies as function of the wave speed parameter

predicted by small perturbation analysis.

15.5.1 Calibration of HA parameters

Using a small perturbation stability analysis of the reduced scale model installed on the test rig, the wave speed and the thermodynamic damping parameters are calibrated. Regarding the mass flow gain factor, the value is derived from the HD model according to Table 15.2. As explained in Section 10.2, this stability analysis in SIMSEN is based on the linearization of the set of hydroacoustic differential equations of the system around the operating point and then, stability is deduced from eigenvalues of the linearized set of equations. Damping and oscillation frequency of the eigenmodes are given respectively by the real part and the imaginary part of the eigenvalues.

To calibrate the wave speed, eigenfrequencies of the test rig are computed as function of this parameter, see Figure 15.17. For a critical wave speed value depending on the eigenmode considered, the eigenfrequency decreases when the wave speed is decreased. To determine the wave speed induced by the cavitation volume of the vortex rope, the experimental unstable frequency value of $f = 1.61$ Hz is used. Since this unstable frequency corresponds to an eigenfrequency of the system [51], this frequency is reached by the first eigenmode when the wave speed is set to $a = 15$ m.s⁻¹. However, if the wave speed derived from the HD model would have been considered as mentioned in Table 15.3, the first eigenfrequency value would be equal to 1.8 Hz as computed in Section 15.3.

Regarding the computation of the thermodynamic damping, it is based on the computation of the system stability diagram. For a given thermodynamic damping, eigenvalues are computed for pairs of parameters $a - \chi_2$. If at least one of the eigenvalues has a positive real part, the system is identified as unstable. In Figure 15.18, two stability diagrams are computed for two thermodynamic dampings. Moreover the set of parameters $a - \chi_2$ derived respectively from eigenfrequencies computation and from the HD model are located in the diagram. By modifying the thermodynamic damping, the limit of stability moves accordingly. The more the damping is increased, the more the system tends to become stable. In Section 14, experiments showed that the system is at the limit of stability. Therefore, the thermodynamic damping is set to $\mu'' = 6000$ Pa.s to move the stability limit up to the computed set of parameters $a - \chi_2$. Finally, the calibrated set of HA parameters according to experimental observations are given in Table 15.5.

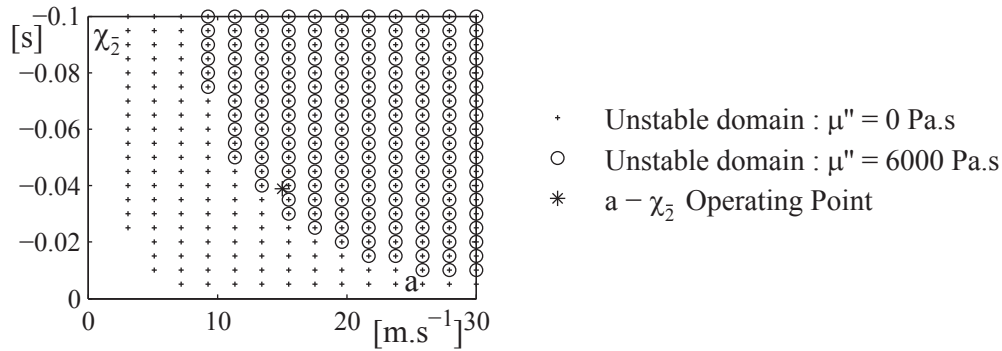


Figure 15.18: Stability diagram of the reduced scale model installed on the test rig computed for two thermodynamic damping values

Table 15.5: Calibrated reduced scale model HA parameters

a	χ_2	μ''
$[m.s^{-1}]$	$[s]$	$Pa.s$
15	-0.039	6000

15.5.2 Transposition to the Prototype

In the previous Section, the key HA parameters of the reduced scale draft tube model have been calibrated with the help of both numerical simulations of the three dimensional flow in the draft tube and the stability analysis of the system based on eigenfrequencies and eigenmodes computation. To investigate the stability operation of the prototype, these HA parameters need to be transposed to the prototype conditions according to similitude laws. To define these similitude laws, a dimensional analysis of each parameter is performed and is expressed as a function of the reference diameter D_{ref} and the runner frequency n by assuming that the influence of the Reynolds number on the transposition is negligible. Then, the dimensionless parameters are defined to establish the relation between the prototype and the reduced scale model parameters. Transpositions of the wave speed and the thermodynamic damping are performed respectively through the electrical components such as capacitance and the thermodynamic resistance. By definition, the cavitation compliance is proportional to the partial derivative of the cavitation volume with respect to the pressure:

$$C_c \sim \frac{\partial V_c}{\partial h} [m^2] \quad (15.19)$$

Dividing by the gravity it yields to:

$$\frac{C_c}{g} \sim \frac{\partial V_c}{\partial (gh)} \quad (15.20)$$

Expressing the dimensions of the cavitation volume V_c and the energy gh as function of the reference diameter and the runner frequency, it yields to:

$$\frac{C_c}{g} \sim \frac{D_{ref}^3}{n^2 D_{ref}^2} \sim \frac{D_{ref}}{n^2} \quad (15.21)$$

Hence, the transposition relation between the prototype and the reduced scale model compliances is:

$$C_c^P = C_c^M \cdot \left(\frac{n^M}{n^P} \right)^2 \cdot \frac{D_{ref}^P}{D_{ref}^M} \quad (15.22)$$

where the superscripts P and M represent the prototype and the model values respectively. The mass flow gain factor is proportional to the partial derivative of the vortex rope cavitation volume with respect to the flow rate:

$$\chi_{\bar{2}} \sim \frac{\partial V_c}{\partial Q} [\text{s}] \quad (15.23)$$

Expressing the dimensions of the cavitation volume V_c and the flow rate as function of the reference diameter and the runner frequency, it yields to:

$$\chi_{\bar{2}} \sim \frac{D_{ref}^3}{D_{ref}^3 n} \sim \frac{1}{n} \quad (15.24)$$

Hence, the transposition relation between the prototype and the reduced scale model mass flow gain factor is:

$$\chi_{\bar{2}}^P = \chi_{\bar{2}}^M \cdot \frac{n^M}{n^P} \quad (15.25)$$

The dimension of the thermodynamic resistance $R_{th} = \mu''/\rho g A l$ is $[\text{s} \cdot \text{m}^{-2}]$. Since the dimensions of the mass flow gain factor and the cavitation compliance are respectively $[\text{s}]$ and $[\text{m}^2]$, the non-dimensional formulations described above with the reference diameter and the runner frequency can be used:

$$R_{th} \cdot g \sim \frac{1}{n} \cdot \frac{n^2}{D_{ref}} \quad (15.26)$$

Therefore, the transposition relation between the prototype and the reduced scale model is:

$$R_{th}^P = R_{th}^M \cdot \frac{D_{ref}^M}{D_{ref}^P} \cdot \frac{n^P}{n^M} \quad (15.27)$$

By assuming that both the Thoma similitude and the Froude similitude conditions are fulfilled between the reduced scale model and the prototype, these transposition relations are applied to the set of calibrated HA parameters, see Table 15.6.

Table 15.6: Transposition of HA parameters

	a [$m.s^{-1}$]	χ_2 [s]	μ'' [$Pa.s$]
Model	15	-0.039	6'000
Prototype	59	-0.157	363'707

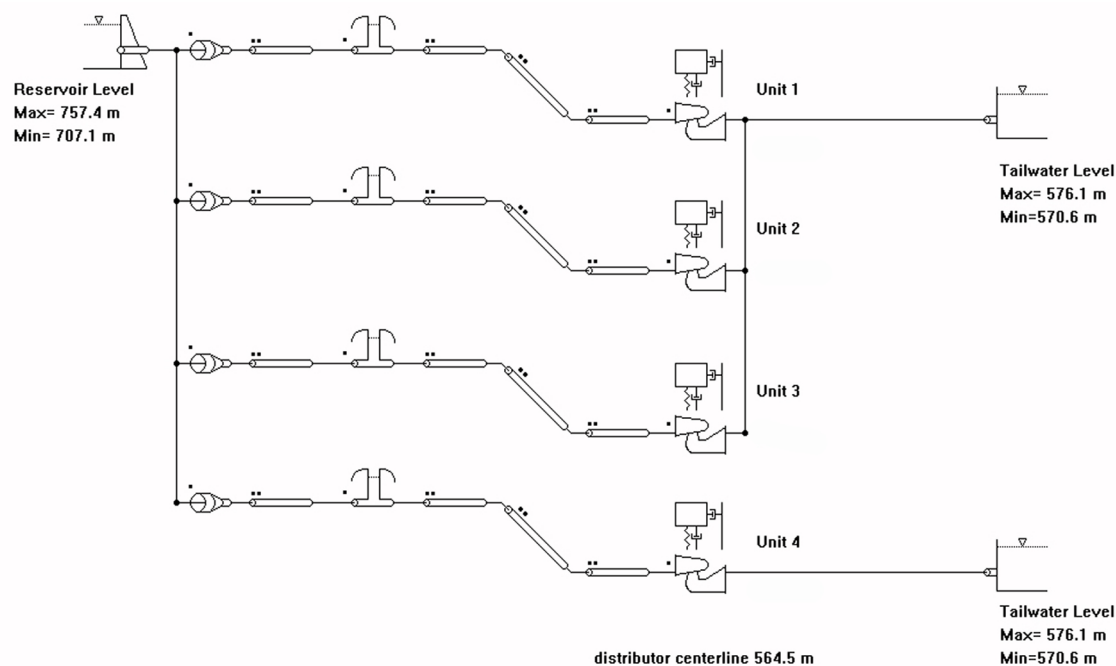


Figure 15.19: HA SIMSEN model of the power plant

15.5.3 Prediction

To investigate the prototype instability, the HA SIMSEN model of the complete power-plant has been set-up, see Figure 15.19. In the HA SIMSEN model, a common constant pressure at the draft tube outlets is applied. Therefore the model behaves as if each unit was isolated without any interaction between units with the same boundary conditions. This independence of the units is clearly debatable since the tailrace tunnel may induce interactions between the Units which would change independently the outlet conditions of the units and therefore would change the hydroacoustic parameters. However, for the investigated surging scenario defined in Table 13.1 only Unit 1 is operating at full load conditions whereas Unit 2 and Unit 3 are near their best efficiency points and Unit 4 is at rest. Therefore, it is assumed that Unit 2, Unit 3 and Unit 4 have a "passive" behavior on the observed surging of the power plant. Hence draft tube HA parameters are applied only for Unit 1.

The stability diagram of the power plant including water conduits and turbine units is plotted in Figure 15.20 with the set of prototype parameters $a-\chi_2$ derived by transposition and given in Table 15.6. As observed experimentally, the operating point is found to be

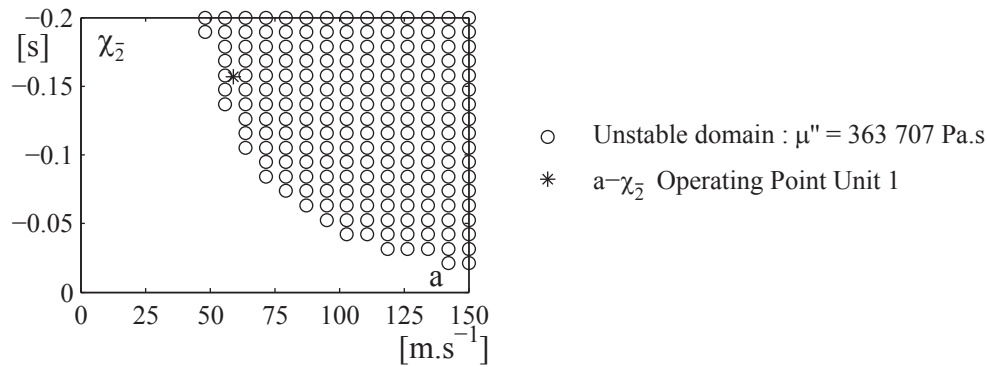


Figure 15.20: Stability diagram of the power plant

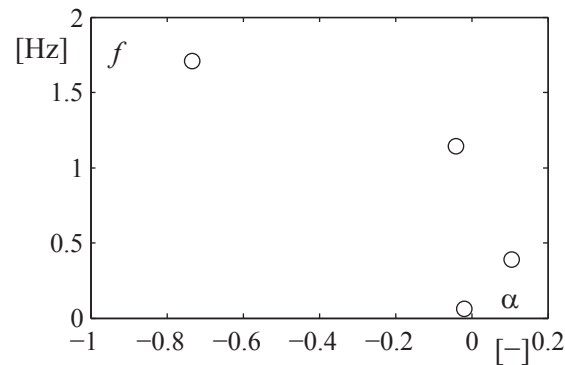


Figure 15.21: Eigenvalues in the complex plan of the prototype HA model

unstable. The corresponding first four eigenvalues are plotted in the complex plan in Figure 15.21. The unstable eigenmode corresponding to a positive modal damping has a frequency value of $f = 0.39$ Hz, compared to the measurements at $f = 0.46$ Hz.

The spatial shape of the pressure and flow rate fluctuations are plotted in Figure 15.22. The figure is subdivided into four parts which correspond to Unit 1, Unit 2, Unit 3 and Unit 4 branches respectively from the top to the bottom. The x axis is the length from the upstream to the downstream reservoirs; the surge shaft and the turbine being located respectively at $x/L = 0.11$ and $x/L = 0.81$. Pressure and flow rate fluctuations occur only on Unit 1 as observed experimentally. The standing wave, features large flow rate fluctuations between the turbine and the downstream water level due to the vortex rope's large compliance compared to the pipes.

The frequency of Mica Unit 1 full load instability, determined using the methodology is in general agreement with the prototype measurements. Although the computed instability frequency of 0.39 Hz is different from the experimental one of 0.46 Hz, the difference is not significant. This difference may be attributed to the following factors. First, the investigated operating point on the reduced scale model does not correspond accurately to the operating point of the surging scenario due to uncertainties of prototype gate openings, power output and Thoma number. Finally, the physics simplifications in the HA and the HD models also contribute to the difference in results.

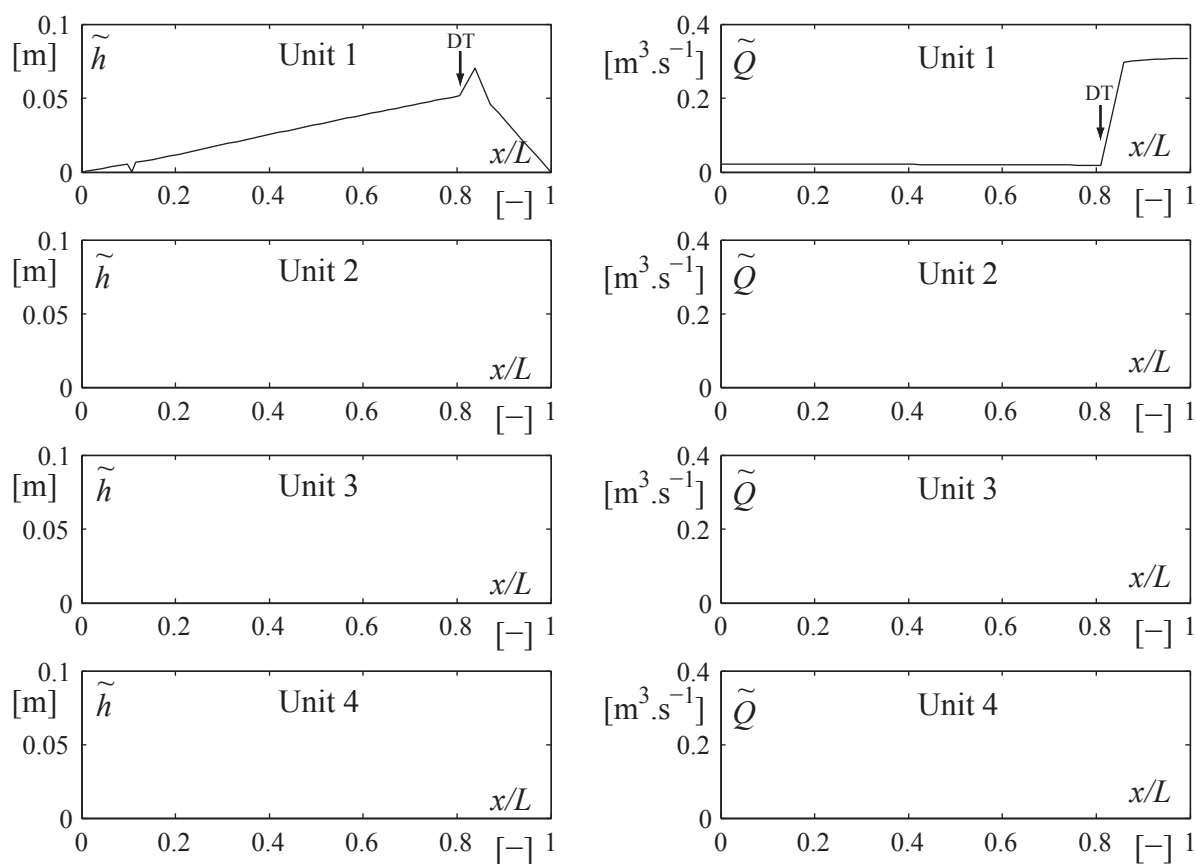


Figure 15.22: Unstable pressure (left) and flow rate (right) eigenmode

Part V

Conclusions and Perspectives

Chapter 16

Conclusions

A methodology to predict part load resonance and full load instability induced by the Francis turbine vortex rope excitation is proposed in this present work. The identification of the excitation sources induced by the cavitating vortex rope is performed with numerical simulations based on a three dimensional incompressible model, called hydrodynamic (HD) model. However, propagation of these sources in the hydraulic system connected to the Francis turbine is simulated with a one dimensional compressible model, called hydroacoustic (HA) model. The HA model covers the entire hydraulic system including the source region corresponding to the draft tube of the Francis turbine whereas the HD model covers only the source region. HA pressure and flow rate fluctuations influence strongly the amount of the cavitation volume in the vortex core which is a decisive parameter for the identification of the excitation sources. Hence a strong interaction exists between the HA field and the sources induced by the vortex rope. Two computing methodologies are used to take into account this HA feedback on the HD field in the draft tube component. The first methodology consists in modeling this HA feedback in the HA model through parameters. In that case, numerical simulation of the cavitating vortex rope with the HD model is performed as a first step where these feedback parameters are evaluated with the sources. Once feedback parameters and sources are determined, they are injected in the HA model to simulate the response of the hydraulic system. This method is called "one way simulation" and has been applied for both part load resonance simulation and full load instability simulation. The second methodology is to impose the feedback to the HD model. HD and HA simulations are performed simultaneously. At each time step, boundary conditions of the HD simulation are driven by the HA simulation results. Hence, computation of the sources in the HD model takes into account the HA feedback of the hydraulic system response. This computing methodology is called "two way simulation" and has been applied only for part load resonance simulation.

A specific HA draft tube model has been developed in the framework of this project. A momentum source modeling the forces induced by the flow acting on the draft tube wall is considered. Moreover, the fluctuating cavitation volume is considered as a mass source and finally, a thermodynamic damping is introduced to model energy dissipation during a phase change between liquid and gas.

In part load operating conditions, two phenomena have been simulated: the part load resonance and the upper part load resonance for which frequency of pressure fluctuations are experienced respectively near 0.3 and between 2 and 4 times the runner frequency. A preliminary evaluation of the identification of the HA feedback parameters and the

sources is performed with a one way simulation of the part load resonance phenomenon. The order of magnitudes of pressure fluctuations of the hydraulic system response are in good agreement with measurements found in the literature especially when HA parameters are derived from single phase simulations. Nonlinear HA feedback parameters depending on the pressure such as the wave speed in the draft tube improve the results of the one way simulation. Two phase flow simulations feature more unsteady behavior and thus provide more energy in a broad band range leading to higher pressure fluctuation amplitudes. However, this investigation needs a deeper validation by a direct comparison with measurements. Through these investigations, it is shown that the cavitation modeling in the HD model is necessary to find the vortex rope precession frequency which depends on the cavitation amount in the vortex core. However, the volume of vapor is underestimated and a correction factor on the Thoma number is necessary between experiments and simulations. Moreover it has been shown that the three dimensional flow in the elbow gives rise to HA sources able to excite the hydraulic system. Finally, the influence of a two way simulation on the HA draft tube model parameters is investigated at part load resonance conditions. Considering the hydraulic layout of the test case and the cavitation conditions investigated, high HA flow rate fluctuations combined with low HA pressure fluctuations inside the draft tube are experienced. It is found out that these fluctuations are not sufficient to influence the HA draft tube model parameters and therefore a one way simulation is sufficient. After this preliminary evaluation, simulation of the upper part load resonance phenomenon has been tackled. It has been found that the mechanism inducing this phenomenon is related to an undesirable fluctuation of the cavitation volume whose frequency can match with an eigenfrequency of the hydraulic system. However, this fluctuation is captured for a Thoma number much higher to the experimental one leading to a cavitation volume very small compared to the experiments.

The full load instability phenomenon has been investigated as well. Consideration of constant HA draft tube model parameters is useful to perform a stability analysis based on eigenvalues and eigenvectors computation. In that case, this linear method allows to identify the stability of the system and to find out unstable frequencies with mode shapes. However, time domain simulation with constant parameters is divergent without reaching a maximum called the "limit cycle". For this reason, nonlinearity of parameters is introduced. It is shown that the essential parameter which allows to reach the limit cycle is the thermodynamic damping. As for the nonlinearity of the wave speed, it allows to reproduce the typical pointed shape of the pressure fluctuations measured on the test rig. Moreover, an energy approach during the limit cycle showed the interaction process between the excitation mass source of the vortex rope and the system dissipation to reach an equilibrium. Indeed, it brings out that over one period, the dissipation can provide energy to the system whereas the mass source dissipates to ensure the equilibrium. Finally, a methodology has been set up to predict the instability of the prototype from the investigations on the reduced scale model. A combination of measurements, numerical simulations and computation of the eigenmodes of the reduced scale model installed on test rig, allows the accurate calibration of the HA draft tube model parameters at the model scale. Then, transposition of these parameters to the prototype according to similitude laws is applied for the stability analysis of the power plant. The unstable prototype frequency, determined using this methodology is in good agreement with the prototype measurements.

The innovative contributions of the present work can be summarized as follow:

- Development of numerical methodology to identify the momentum source induced by the cavitating swirling flow in the elbow draft tube. This identification, based on the computation of the fluid force acting on the draft tube wall, is much more accurate than the computation of the synchronous component of the wall pressure fluctuations experienced in the same cone cross section. This force is a global quantity easy to derive from numerical simulations and can be used for various engineering applications.
- Highlight of the influence of the elbow on the HA sources generation.
- Demonstration that the use of nonlinear HA draft tube model parameters depending on the pressure is required. As shown in previous works, the modeling of the HA pressure feedback on this mass source, through the cavitation compliance parameter, allows to predict the modification of the eigenmodes shapes and the corresponding frequencies. However, this research project went further by introducing nonlinearity of this parameter as function of the pressure allowing to simulate pressure fluctuations featuring a non-sinusoidal shape at resonance conditions. The use of nonlinear parameters has been extended to the thermodynamic damping parameter as well which has never been introduced in previous works. It has been shown that this new parameter is necessary to perform time domain simulations of full load instability and nonlinearity enabling to reach the "limit cycle". Regarding the mass flow gain factor parameter definition, the downstream flow rate to the cavitation volume has been chosen as reference to model the diffuser effect on the flow destabilization. However, nonlinearity of this parameter has not been investigated in the scope of the present study but could enhance the accuracy of the prediction and the simulation of the full load instability.
- Improvement of the understanding of the mechanism inducing upper part load resonance phenomenon. Unsteady two phase flow numerical simulations allowed to identify cavitation volume fluctuations at the high frequency component responsible to the resonance with a high order eigenmode of the hydraulic system.

Chapter 17

Perspectives

This present work allowed to solve some issues but rises other ones as well. The HA draft tube model and the flow numerical simulations with the HD model must be improved to enhance the accuracy of the resonance prediction. Hence, three research orientations are proposed:

- improvement of the cavitation model used in the HD model,
- experimental evidence of the thermodynamic damping parameter and development of an analytical model applied to the vortex rope,
- statement on the definition of the mass flow gain factor parameter in the full load HA draft tube model.

The improvement of the cavitation model used in the HD model is highlighted since it is necessary to find the vortex rope precession frequency which depends on the cavitation amount in the vortex core. However, the volume of vapor is underestimated and a correction factor on the Thoma number is necessary between experiments and simulations. The homogeneous cavitation model has been used but other models are available and must be tested such as the one based on equation of state making relation between pressure and density or the two fluid models. Despite of some differences between experiments and two phase simulations, it seems that fundamental phenomena are quite well captured but the onset is shifted with respect to measurements. For instance, the dependence of the vortex rope frequency to the cavitation volume, the unsteadiness of the helical vortex rope making nodes with its tail or the undesirable fluctuation of the cavitation volume experienced at upper part load conditions, are simulated even with the homogeneous model. Hence, efforts must be considered on this topic. Fundamental test case and corresponding numerical simulations must be carried out.

The experimental evidence of the thermodynamic damping parameter is quite difficult to tackle since this parameter is a quantity which is not directly measurable. The first proposition would be to set up an experiment on a test rig where part load resonance phenomenon occurs between the vortex rope precession frequency and the first eigenmode of the test rig. In this present work, the simulation of this phenomenon has shown that resulting pressure fluctuation amplitudes depend strongly on this thermodynamic damping parameter. By considering that the momentum sources and the cavitation compliance parameter are well computed from incompressible numerical simulations, the thermodynamic damping can be taken as a parameter and determined by comparing measurements

and HA one way simulation. Once order of magnitudes are found from this experiment, an analytical model applied to the vortex rope could be developed instead of the analytical formulation applied to a uniform bubbly flow which has been used in this present work. Physical systems without damping do not exist but the way to quantify it is still unknown.

The statement on the definition of the mass flow gain factor parameter is related to the instability phenomenon at full load conditions. Actually, two mass flow gain factors can be defined. They traduce respectively the influence of the upstream and the downstream flow rates to the cavitation volume on the mass source. The upstream definition aims to model the swirl effect whereas the downstream definition model the diffuser effect of the draft tube. In this present work, the downstream definition has been used by considering that the instability is due to the destabilization of the swirling flow due to the diffuser. Using this model formulation, stability of some operating points can be found but the accuracy of the prediction must be improved. Maybe the two formulations must be considered and some authors plan to introduce another parameter being a time delay of the swirl effect on the cavitation volume. Extensive experimental measurements are necessary to state on the physical process generating this cavitation volume instability: either inlet swirl effect or diffuser effect. Experimental investigations on reduced scale model should be performed in parallel with a simplified test case on the cavitation tunnel at the Laboratory for Hydraulic Machines. Modifications of the cavitation tunnel would be required to generate a swirling flow in a diffuser within the test section. The works on the reduced scale model will be used to create a data base for future validations of new HA draft tube models whereas investigations in the cavitation tunnel would have more a vocation to study the fundamental aspects of the cavitating flow instability by playing with the swirl intensity and the diffuser angle as parameter. In both cases, the cavitation volume, the upstream and downstream flow rate fluctuations must be measured and synchronized with pressure fluctuation measurements. Moreover, an excitation of the swirling flow should be considered to analyze the response which would allow to identify some parameters of the new HA models describing the dynamic behavior of the cavitation volume. Numerical investigations are planed as well by performing unsteady two phase flow simulations. The combination of these simulations with the experimental investigations will allow to deeper understand the instability phenomenon and to develop improved HA models.

This research project was aiming to simulate resonance phenomena with the hydraulic system connected to the Francis turbine. However, the understanding of the flow pattern in the elbow draft tube should be improved as well. Depending on the flow rate through the draft tube, the cavitating vortex rope features either helical or axi-symmetric shape. This observation is widely accepted by the community but the physical process explaining this major difference is still unknown. The use of the cavitation tunnel would be of interest to investigate these fundamental aspects dealing with the instability of the vortex flows.

References

References

- [1] ANGELICO, G., MUCIACCIA, F., AND ROSSI, G. Part load behaviour of a turbine: a study on a complete model of a hydraulic power plant. In *Proceedings of the 13th IAHR Symposium on Hydraulic Machinery and Systems, Beijing, China* (1986).
- [2] ARPE, J. *Analyse du champ de pression pariétale d'un diffuseur coudé de turbine francis*. PhD thesis, EPFL, N°2779, 2003.
- [3] ARPE, J., AND AVELLAN, F. Pressure wall measurements in the whole draft tube: steady and unsteady analysis. In *Proceedings of the 21st IAHR Symposium on Hydraulic Machinery and Systems, Lausanne, Switzerland* (2002), pp. 593–602.
- [4] ARPE, J., NICOLET, C., AND AVELLAN, F. Experimental evidence of hydroacoustic pressure waves in a francis turbine elbow draft tube for low discharge conditions. *Journal of Fluids Engineering* 131 (2009), pp. 081102 1–9.
- [5] AURÉGAN, Y., MAUREL, A., PAGNEUX, V., AND PINTON, J. *Sound-flow interactions*, vol. 586. 2002.
- [6] AVELLAN, F. Flow investigation in a francis draft tube: The flindt project. In *Proceedings of the 20th IAHR Symposium, Charlotte, North Carolina, USA* (2000).
- [7] BARTOLINI, P., AND SICCARDI, F. A proposal to evaluate the energy dissipation in an unsteady two phase bubbly flow with low gas-liquid ratio. *L'Energia Elettrica* (1975), pp. 387–392.
- [8] BENJAMIN, T. Theory of the vortex breakdown phenomenon. *Journal of Fluid Mechanics* 14, 4 (1962), pp. 593–629.
- [9] BOSSEL, H. Vortex breakdown flowfield. *Physics of Fluids* 12 (1969), pp. 498–508.
- [10] BRENNEN, C. Bubbly flow model for the dynamic characteristics of cavitating pumps. *Journal of Fluid Mechanics* 89, 2 (1978), pp. 223–240.
- [11] BRENNEN, C., AND ACOSTA, A. Theoretical, quasi-static analysis of cavitation compliance in turbopumps. *Journal of Spacecraft and Rockets* 10, 3 (1973), pp. 175–180.
- [12] BRENNEN, C., AND ACOSTA, A. The dynamic transfer function for a cavitating inducer. *Journal of fluids engineering* 98 (1976), pp. 182–191.
- [13] BRUCKER, C., AND ALTHAUS, W. Study of vortex breakdown by particle tracking velocimetry (ptv). *Experiments in fluids* 13, 5 (1992), pp. 339–349.

- [14] BUNTIC OGOR, I., DIETZE, S., AND RUPRECHT, A. Numerical simulation of the flow in turbine-99 draft tube. In *Proceedings of the 3rd IAHR/ERCOFAC workshop on draft tube flow, Porjus, Sweden* (2005).
- [15] CASSIDY, J., AND FALVEY, H. Observations of unsteady flow arising after vortex breakdown (helical vortex generation in rotating flow in straight tube having angular momentum flux sufficiently large relative to linear momentum flux. *Journal of Fluid Mechanics* 41 (1970), pp. 727–736.
- [16] CHEN, C., NICOLET, C., YONEZAWA, K., FARHAT, M., AVELLAN, F., MIYAGAWA, K., AND TSUJIMOTO, Y. Experimental study and numerical simulation of cavity oscillation in a conical diffuser. *International Journal of Fluid Machinery and Systems* 3 (2010), pp. 91–101.
- [17] CHEN, C., NICOLET, C., YONEZAWA, K., FARHAT, M., AVELLAN, F., MIYAGAWA, K., AND TSUJIMOTO, Y. Experimental study and numerical simulation of cavity oscillation in a diffuser with swirling flow. *International Journal of Fluid Machinery and Systems* 3 (2010), pp. 80–90.
- [18] CHEN, C., NICOLET, C., YONEZAWA, K., FARHAT, M., AVELLAN, F., AND TSUJIMOTO, Y. One-dimensional analysis of full load draft tube surge. *Journal of Fluids Engineering* 130 (2008), pp. 041106 1–6.
- [19] CHU, B. On the energy transfer to small disturbances in fluid flow (part i). *Acta Mechanica* 1, 3 (1965), pp. 215–234.
- [20] CIOCAN, G., AVELLAN, F., AND KUENY, J. Optical measurement techniques for experimental analysis of hydraulic turbines rotor-stator interaction. In *Proceedings of the ASME Fluids Engineering Division Summer Meeting, Boston, Massachusetts, USA* (2000), pp. 11–15.
- [21] CIOCAN, G., ILIESCU, M., STUDENT, D., VU, T., ENGINEER, S., NENNEMANN, B., AND AVELLAN, F. Experimental study and numerical simulation of the flint draft tube rotating vortex. *Journal of Fluids Engineering* 129 (2007), pp. 146–158.
- [22] COUSTON, M., AND PHILIBERT, R. Partial load modelling of gaseous francis turbine rope. *The international journal on Hydropower and Dams* 1 (1998), pp. 525–533.
- [23] DOWLING, A. Nonlinear self-excited oscillations of a ducted flame. *Journal of Fluid Mechanics* 346 (1997), pp. 271–290.
- [24] DÖRFLER, P. Modèle mathématique des oscillations excitées à charge partielle par la torche de cavitation dans les turbines francis. In *Bulletin Escher Wyss* (1980).
- [25] DÖRFLER, P. System dynamics of the francis turbine half load surge. In *Proceedings of Operating Problems of Pump Stations and Powerplants, Amstredam, Netherlands* (1982).
- [26] DÖRFLER, P. Francis turbine surge prediction and prevention. In *Proceedings of waterpower 85, Stirling, Scotland* (1984).

- [27] DÖRFLER, P. Observation of pressure pulsations on a francis model turbine with high specific speed. *The international journal on Hydropower and Dams 1* (1994), pp. 21–26.
- [28] DÖRFLER, P. Evaluating 1d models for vortex-induced pulsation in francis turbines. In *Proceedings of the 3rd International Meeting of the Workgroup on Cavitation and Dynamic Problems in Hydraulic Machinery and Systems, Brno, Czech Republic* (2009), vol. 2, pp. 315–324.
- [29] DÖRFLER, P., KELLER, M., AND BRAUN, O. Francis full-load surge mechanism identified by unsteady 2-phase cfd. In *Proceedings of the 25th IAHR Symposium on Hydraulic Machinery and Systems, Timisoara, Romania* (2010), vol. 12, IOP Publishing, p. 012026.
- [30] DUTTWEILER, M., AND BRENNEN, C. Surge instability on a cavitating propeller. *Journal of Fluid Mechanics 458* (2002), pp. 133–152.
- [31] EIA. International energy annual 2006 (june-december 2008), web site www.eia.doe.gov/iea. Tech. rep., Energy Information Administration (EIA), 2006.
- [32] EL-ASHRY, M. Renewables 2009 global status report. Tech. rep., REN21, Renewable Energy Policy Network for the 21st century, 2009.
- [33] ESCUDIER, M., BORNSTEIN, J., AND ZEHNDER, N. Observations and lda measurements of confined turbulent vortex flow. *Journal of Fluid Mechanics 98*, 1 (1980), pp. 49–63.
- [34] EWING, D. Allowing for free air in waterhammer analysis. In *Proceedings of the 3rd International Conference on Pressure Surges, Canterbury, UK* (1980), pp. 127–146.
- [35] FALER, J., AND LEIBOVICH, S. Disrupted states of vortex flow and vortex breakdown. *Physics of Fluids 20* (1977), pp. 1385.
- [36] FANELLI, M. The vortex rope in the draft tube of francis turbines operating at partial load: a proposal for a mathematical model. *Journal of Hydraulic Research 27*, 6 (1989), pp. 769–807.
- [37] FLEMMING, F., FOUST, J., KOUTNIK, J., AND FISHER, R. Overload surge investigation using cfd data. In *Proceedings of the 24th IAHR Symposium on Hydraulic Machinery and Systems, Foz Do Iguassu, Brazil* (2008).
- [38] FRANC, J., AVELLAN, F., BELAHADJI, B., BILLARD, J., BRIANÇON-MARJOLLET, L., FRÉCHOU, D., FRUMAN, D., KARIMI, A., KUENY, J., AND MICHEL, J. *La cavitation*. EDP Sciences, 1995.
- [39] FRITSCH, A., AND MARIA, D. Comportement dynamique d’une turbine francis à charge partielle. comparaison modèle-prototype. *La Houille Blanche 3-4*, 3-4 (1988), pp. 273–282.
- [40] GHAHREMANI, F. Turbo-pump cavitation compliance. Tech. Rep. TOR-0059(6531-01)-2, The aerospace corporation, 1970.

- [41] GHAHREMANI, F. Pump cavitation compliance. In *Proceedings of the Cavitation Forum, ASME, New York, USA* (1971), pp. 1–3.
- [42] HABAN, V., K. J., AND POCHYLÝ, F. 1d mathematical model of high frequency pressure oscillations induced by rsi including an influence of fluid second viscosity. In *Proceedings of the 21st IAHR Symposium on Hydraulic Machinery and Systems, Lausanne, Switzerland* (2002).
- [43] HABAN, V., RUDOLF, P., POCHYLÝ, F., KOUTNIK, J., AND KRUGER, K. Stability of infinitely long asymmetrical vortex rope. In *Proceedings of the 2nd IAHR International Meeting of the workgroup on Cavitation and Dynamic Problems in Hydraulic Machinery and Systems, Timisoara, Romania*. (2007), vol. 10, p. 13.
- [44] HALL, M. A new approach to vortex breakdown. In *Proceedings of the Heat Transactions and Fluid Mechanics Institute* (1967).
- [45] HARVEY, J. Some observations of the vortex breakdown phenomenon. *Journal of Fluid Mechanics* 14, 4 (1962), pp. 585–592.
- [46] HIMR, D., AND HABAN, V. Simulation of low pressure water hammer. In *Proceedings of the 25th IAHR Symposium on Hydraulic Machinery and Systems, Timisoara, Romania* (2010).
- [47] HOWE, M. *Theory of vortex sound*. Cambridge University Press, 2003.
- [48] ILIESCU, M., CIOCAN, G., AVELLAN, F., ET AL. Analysis of the cavitating draft tube vortex in a francis turbine using particle image velocimetry measurements in two-phase flow. *Journal of Fluids Engineering* 130 (2008), pp. 021105 1–10.
- [49] JACOB, T. *Evaluation sur modèle réduit et prédiction de la stabilité de fonctionnement des turbines francis*. PhD thesis, EPFL, N°1146, 1993.
- [50] JACOB, T., AND ANGELICO, G. Fonctionnement instable d’un modèle réduit de turbine francis a debit partiel: evaluation de l’intensité de l’excitation. In *Proceedings of the 17th Symposium on Hydraulic Machinery and Systems, Beijing, Chine* (1994).
- [51] JACOB, T., PRENAT, J., AND MARIA, D. Comportement dynamique d’une turbine francis à forte charge. comparaisons modèle-prototype. *La Houille Blanche* 3, 3-4 (1988), pp. 293–300.
- [52] JACOB, T., PRÉNAT, J., VULLIQUOD, G., AND LOPEZ ARAGUAS, B. Surging of 140mw francis turbines at high load , analysis and solution. In *Proceedings of the 16th IAHR Symposium on Hydraulic Machinery and Systems, Sao Paulo, Brazil* (1992).
- [53] JORDAN, D., AND SMITH, P. *Nonlinear ordinary differential equations: an introduction for scientists and engineers*. Oxford University Press, 2007.
- [54] KOUTNIK, J., FAIGLE, P., AND MOSER, W. Pressure fluctuations in francis turbines-theoretical prediction and impact on turbine. In *In proceedings of the 24th Symposium on Hydraulic machinery and Systems, Foz do Iguassu, Brazil* (2008).

- [55] KOUTNIK, J., KRÜGER, K., POCHLY, F., RUDOLF, P., AND HABAN, V. On cavitating vortex rope form stability during francis turbine part load operation. In *Proceedings of the International Meeting of Working Group on Cavitation and Dynamic Problems in Hydraulic Machinery and Systems IAHR, Barcelona, Spain* (2006).
- [56] KOUTNIK, J., NICOLET, C., SCHOHL, G., AND AVELLAN, F. Overload surge event in a pumped-storage power plant. In *Proceedings of the 23rd IAHR Symposium on Hydraulic Machinery and Systems, Yokohama, Japan* (2006).
- [57] KOUTNIK, J., AND PULPITEL, L. Modeling of the francis turbine full-load surge. In *Proceedings of Modeling, Testing and Monitoring for Hydro Power Plants* (1996).
- [58] KUIBIN, P., OKULOV, V., RESIGA, R. F., AND MUNTEAN, S. Validation of mathematical models for predicting the swirling flow and the vortex rope in a francis turbine operated at partial discharge. In *Proceedings of the 25th IAHR Symposium on Hydraulic Machinery and Systems, Timisoara, Romania* (2010).
- [59] KUNDUR, P., BALU, N., AND LAUBY, M. *Power system stability and control*. McGraw-Hill New York, 1994.
- [60] LANDA, P. *Nonlinear oscillations and waves in dynamical systems*. Springer, 1996.
- [61] LANDAU, L., AND LIFSHITZ, E. *Physique théorique. Vol 6 Mécanique des fluides*. 1989.
- [62] LIGHTHILL, M. On sound generated aerodynamically. i. general theory. *Proceedings of the Royal Society of London. Series A, Mathematical and Physical Sciences* 211, 1107 (1952), pp. 564–587.
- [63] MCMILLAN, A. A non-linear friction model for self-excited vibrations. *Journal of Sound and Vibration* 205, 3 (1997), pp. 323–335.
- [64] MENTER, F. Two-equation eddy-viscosity turbulence models for engineering applications. *AIAA journal* 32, 8 (1994), pp. 1598–1605.
- [65] MENTER, F., AND EGOROV, Y. A scale-adaptive simulation model using two-equation models. In *Proceedings of the 43rd AIAA Aerospace Sciences Meeting and Exhibit, Reno, USA* (2005).
- [66] MIYAGAWA, K., TSUJI, K., YAHARA, J., AND NOMBRA, Y. Flow instability in an elbow draft tube for a francis pump-turbine. In *Proceedings of the 21st IAHR Symposium on Hydraulic Machinery and Systems, Lausanne, Switzerland* (2002), pp. 277–286.
- [67] NICOLET, C. *Hydroacoustic modelling and numerical simulation of unsteady operation of hydroelectric systems*. PhD thesis, EPFL, N°3751, 2007.
- [68] NICOLET, C., ARPE, J., AND AVELLAN, F. Identification and modeling of pressure fluctuations of a francis turbine scale model at part load operation. In *Proceedings of the 22nd IAHR Symposium on Hydraulic Machinery and Systems, Stockholm, Sweden* (2004).

- [69] NICOLET, C., ZOBEIRI, A., MARUZEWSKI, P., AND AVELLAN, F. On the upper part load vortex rope in francis turbine: Experimental investigation. In *Proceedings of the 25th IAHR Symposium on Hydraulic Machinery and Systems, Timisoara, Romania* (2010), vol. 12, IOP Conference Series: Earth and Environmental Science, p. 012053.
- [70] NISHI, M., MATSUNAGA, S., KUBOTA, T., AND SENOO, Y. Flow regimes in an elbow-type draft tube. In *Proceedings of the 11th IAHR Symposium on Hydraulic Machinery and Systems, Amsterdam, Netherlands* (1982), vol. 38, pp. 1–13.
- [71] NISHI, M., MATSUNAGA, S., KUBOTA, T., AND SENOO, Y. Surging characteristics of conical and elbow type draft tubes. In *Proceedings of the 12th IAHR Symposium on Hydraulic Machinery and Systems, Stirling, Scotland* (Stirling, 1984), pp. 272–283.
- [72] NISHI, M., WANG, X., OKAMOTO, M., AND MATSUNAGA, S. Further investigation on the pressure fluctuations caused by cavitated vortex rope in an elbow draft tube. *Cavitation and gas-liquid flow in fluid machinery and devices 190* (1994), pp. 63–70.
- [73] PAIK, J., SOTIROPOULOS, F., SALE, M., ET AL. Numerical simulation of swirling flow in complex hydroturbine draft tube using unsteady statistical turbulence models. *Journal of Hydraulic Engineering 131* (2005), pp. 441.
- [74] PEZZINGA, G. Dissipazioni nei transitori di colpo d ariete in presenza e in assenza di cavitazione. In *Atti del XIV Congresso Nazionale AIMETA, Como, Italy* (1999).
- [75] PEZZINGA, G. Second viscosity in transient cavitating pipe flows. *Journal of Hydraulic Research 41*, 6 (2003), pp. 656–665.
- [76] PHILIBERT, R., AND COUSTON, M. Francis turbines at part load. matrix simulating the gaseous rope. In *Proceedings of the 19th IAHR Symposium on Hydraulic Machinery and Cavitation, Singapore* (1998), p. 441.
- [77] POCHYLY, F., CERMAK, L., RUDOLF, P., HABAN, V., AND KOUTNIK, J. Assessment of the steady swirling flow stability using amplitude frequency characteristic. In *Proceedings of the 3rd IAHR International Meeting of the Workgroup on Cavitation and Dynamic Problems in Hydraulic Machinery and Systems, Brno, Czech Republic* (2009).
- [78] POWELL, A. Theory of vortex sound. *The journal of the acoustical society of America 36* (1964), pp. 177.
- [79] RANDALL, J., AND LEIBOVICH, S. The critical state- a trapped wave model of vortex breakdown(trapped wave vortex breakdown model for long weakly nonlinear wave propagation on critical flows in tubes of variable cross sections). *Journal of Fluid Mechanics 58* (1973), pp. 495–515.
- [80] RATH, H. Unsteady pressure waves and shock waves in elastic tubes containing bubbly air-water mixtures. *Acta Mechanica 38*, 1 (1981), pp. 1–17.
- [81] RIBNER, H. The generation of sound by turbulent jets. *Advances in Applied Mechanics 8* (1964), pp. 103–182.

- [82] RUCHONNET, N. *Multi-Scale Computational Strategy Applied to Hydroacoustic Resonance in Cavitating Pipe Flow*. PhD thesis, EPFL, N°4778, 2010.
- [83] RUDOLF, P., AND SKOTAK, A. Unsteady flow in the draft tube with elbow, part b-numerical simulation. In *Proceedings of the Xth International Meeting of the Work Group on the behaviour of hydraulic machinery under steady oscillatory conditions IAHR, Trondheim, Norway* (2001).
- [84] RUPRECHT, A., HELMRICH, T., ASCHENBRENNER, T., AND SCHERER, T. Simulation of pressure surge in a hydro power plant caused by an elbow draft tube. In *Proceedings of the Xth International Meeting of the workgroup on the behaviour of hydraulic machinery under steady oscillatory conditions, Trondheim, Norway* (2001).
- [85] SARPKEYA, T. On stationary and travelling vortex breakdowns. *Journal of Fluid Mechanics* 45, 3 (1971), pp. 545–559.
- [86] SICK, M., DOERFLER, P., MICHLER, W., SALLABERGER, M., AND LOHMBERG, A. Investigation of the draft tube vortex in a pump-turbine. In *Proceedings of the 22nd IAHR Symposium on Hydraulic Machinery and Systems, Stockholm, Sweden* (2004).
- [87] SKOTAK, A., MIKULASEK, J., AND LHOTAKOVA, L. Effect of the inflow conditions on the unsteady draft tube flow. In *Proceedings of the 21st IAHR Symposium on Hydraulic Machinery and Systems, Lausanne, Switzerland* (2002), pp. 294–311.
- [88] STEIN, P., SICK, M., DOERFLER, P., WHITE, P., AND BRAUNE, A. Numerical simulation of the cavitating draft tube vortex in a francis turbine. In *Proceedings of the 23rd IAHR Symposium on Hydraulic Machinery and Systems, Yokohama, Japan* (2006).
- [89] SUSAN-RESIGA, R., CIOCAN, G., ANTON, I., AND AVELLAN, F. Analysis of the swirling flow downstream a francis turbine runner. *Journal of Fluids Engineering* 128 (2006), pp. 177.
- [90] TSUJIMOTO, Y., KAMIJO, K., AND YOSHIDA, Y. A theoretical analysis of rotating cavitation in inducers. *Journal of Fluids Engineering* 115, 1 (1993), pp. 135–141.
- [91] TSUJIMOTO, Y., WATANABE, S., KAMIJO, K., AND YOSHIDA, Y. A nonlinear calculation of rotating cavitation in inducers. *Journal of Fluids Engineering* 118 (1996), pp. 589.
- [92] WANG, Z., AND ZHOU, L. Simulations and measurements of pressure oscillations caused by vortex ropes. *Journal of Fluids Engineering* 128 (2006), pp. 649.
- [93] WATANABE, S., AND BRENNEN, C. Dynamics of a cavitating propeller in a water tunnel. *Journal of fluids engineering* 125, 2 (2003), pp. 283–292.
- [94] WYLIE, E., STREETER, V., AND SUO, L. *Fluid transients in systems*. Prentice Hall Englewood Cliffs, NJ, 1993.

- [95] ZIELKE, W., AND HACK, H. Resonance frequencies and associated mode shapes of pressurized piping systems. In *Proceedings of the International Conference Pressure Surges, Cranfield, UK (1972)*, vol. G1, pp. 1–13.
- [96] ZOBELI, A. *Investigations of time dependent phenomena in a turbine and a pump-turbine of Francis type: rotor-stator interactions and precessing vortex rope*. PhD thesis, EPFL, N°4272, 2009.

Curriculum Vitae

Sébastien Alligné

Avenue de la gare 29
1003 LAUSANNE
Suisse
+41 78 908 34 95
s.alligne@hotmail.com



Français
Né le 27 septembre 1978

FORMATION

2007-2011	Doctorat ès sciences techniques Ecole Polytechnique Fédérale de Lausanne (EPFL), Suisse
1999-2002	Master en Génie Mécanique ENSE3-INPG, France
1996-1999	Classes Préparatoires en Physique et Technologie Lycée Marie Curie (OISE-France)
1993-1996	Baccalauréat ès sciences Lycée Marie Curie (OISE-France)

EXPERIENCES PROFESSIONNELLES

2007-2011	Ecole Polytechnique Fédérale de Lausanne (EPFL), Suisse Laboratoire de Machines Hydrauliques (LMH) Activités de recherche: Prediction des fluctuations de pression au sein d'une installation hydroelectrique induites par une torche cavitante de turbines Francis à la fois en charge partielle et forte charge. Identification de la source d'excitation par simulation CFD de la torche cavitante et simulation de la propagation de cette source dans le système hydraulique représenté par un model compressible monodimensionnel. Comparaison avec des résultats de mesures. Développement et maintenance d'un logiciel de calcul transitoire: interaction avec différents partenaires industriels pour des développements de modèles spécifiques Activités d'enseignement: Encadrement de travaux pratiques de Masters
2004-2007	ASD-SIREM, Miribel, France Gestion de developpements produits allant de la rédaction du cahier des charges à l'industrialisation. Interface entre les différents intervenants du projet: bureaux d'études, fournisseurs, production, service achats, service qualité, laboratoire d'essais. Expertise hydraulique pour le développement de nouvelles pompes et nouveaux jets massants
2004 (7 months)	IPSIS en mission chez PSA Peugeot Citroën, Garenne Colombes, France Ingénieur consultant. Implementation et tests de fonctions de controle commande d'un double embrayage

- 2003 (10 months) **B2I en mission chez Renault, Lardy, France**
Ingénieur consultant. Résolution d'un problème de détérioration des pistons moteur.
Mise en place et pilotage d'essais avec les experts des différents métiers tels que
l'hydraulique du circuit d'injection, la mécanique moteur et les lois de contrôle
commande du calculateur d'injection. Identification du défaut et correction.
- 2002 (4 months) **B2I en mission chez PSA Peugeot Citroën, Sochaux, France**
Ingénieur consultant. Développement de gamme de tests automatiques pour valider
les logiciels de contrôle commande des moteurs diesel avant lancement série

COMPETENCES

Programmation: C,C++, Visual Basic, Fortran, Matlab, Delphi
CFD-CAO: ANSYS CFX, ICEM, SOLIDWORKS, IDEAS
Bureautique: MS-Office, Adobe Illustrator, Latex
Theorie: Ecoulements transitoires, Hydraulique, Machines hydrauliques, Mécanique vibratoire
Langues: Français (Langue maternelle), Anglais (Courant), Espagnol (Scolaire)

INTERETS

Sports: Kitesurf, Course à pied, Tennis
Loisirs: Voyage, Photographie

List of Publications

Journal papers

1. Alligné, S. and Nicolet, C. and Avellan, F., Identification of Francis Turbine Helical vortex rope Excitation by CFD simulation and Resonance Simulation with the Hydraulic System, *Journal of Fluid Engineerings*, Submitted for publication
2. Alligné, S. and Nicolet, C. and Avellan, F., Identification of the Mechanism Inducing Upper Part Load Resonance Phenomenon by CFD Simulation, *Journal of Fluid Engineerings*, Submitted for publication
3. Ruchonnet, N. and Alligné, S. and Nicolet, C. and Avellan, F., Cavitation Influence on Hydroacoustic Resonance in Pipe, *Journal of Fluids and Structures*, Submitted for publication
4. Alligné, S. and Nicolet, C. and Allenbach, P. and Kawkabani, B. and Simond, J.J. and Avellan, F., Influence of the Francis turbine location under vortex rope excitation on the hydraulic system stability, *International Journal of Fluid Machinery and Systems*, Vol 2, Issue 4, October-December 2009

Conference papers

1. Alligné, S. and Nicolet, C. and Avellan, F., Identification of the Mechanism Inducing Upper Part Load Resonance Phenomenon by CFD Simulation, *Proceedings of the 4th IAHR WG Meeting on Cavitation and Dynamic Problems in Hydraulic Machinery and Systems*, Belgrade, Serbia, October 2011
2. Nicolet, C. and Kaelbel, T. and Alligné, S. and Ruchonnet, N. and Allenbach, P. and Bergant, A. and Avellan F., Simulation of Water Hammer Induced Column Separation through Electrical Analogy, *Proceedings of the 4th IAHR WG Meeting on Cavitation and Dynamic Problems in Hydraulic Machinery and Systems*, Belgrade, Serbia, October 2011
3. Landry, C. and Alligné, S. and Hasmatuchi, V. and Roth, S. and Müller, A. and Avellan, F., Non-Linear Stability Analysis of a Reduced Scale Model Pump-Turbine at Off-Design Operation, *Proceedings of the 4th IAHR WG Meeting on Cavitation and Dynamic Problems in Hydraulic Machinery and Systems*, Belgrade, Serbia, October 2011
4. Müller, A. and Alligné, S. and Paraz, F. and Landry, C. and Avellan, F., Determination of Hydroacoustic Draft Tube Parameters by High Speed Visualization during Model Testing of a Francis Turbine, *Proceedings of the 4th IAHR WG Meeting on Cavitation and Dynamic Problems in Hydraulic Machinery and Systems*, Belgrade, Serbia, October 2011
5. Alligné, S. and Nicolet, C. and Avellan, F., Identification of Francis Turbine Helical vortex rope Excitation by CFD simulation and Resonance Simulation with the Hydraulic System, *Proceedings of the 7th International Symposium on Pumping Machinery*, Hamamatsu, Japan, July 2011
6. Alligné, S. and Maruzewski, P. and Dinh, T. and Wang, B. and Fedorov, A. and Iosfin, J. and Avellan, F., Prediction of a Francis turbine prototype full load instability from investigations on the reduced scale model, *Proceedings of the 25th IAHR Symposium on Hydraulic Machinery and Systems*, Timisoara, Romania, September 2010

7. Nicolet, C. and Ruchonnet, N. and Alligné, S. and Koutnik, J. and Avellan, F., Hydroacoustic Simulation of Rotor-Stator Interaction in Resonance Conditions in Francis Pump-Turbine, *Proceedings of the 25th IAHR Symposium on Hydraulic Machinery and Systems, Timisoara, Romania, September 2010*
8. Silva, P.C.O. and Kawkabani, B. and Alligné, S. and Nicolet, C. and Simond, J.-J. and Avellan, F., Stability Study of a Complete Hydroelectric Production Site by Eigenvalues Analysis Method Based on Phase Variables, *Proceedings of ICEM 2010 - XIX International Conference on Electrical Machines, Rome, Italy, September 2010*
9. Alligné, S. and Nicolet, C. and Ruchonnet, N. and Hasmatuchi, V. and Maruzewski, P. and Avellan, F., Numerical simulation of nonlinear self-oscillations of a full load vortex rope, *Proceedings of the 3rd Meeting IAHR Workgroup on Cavitation and Dynamic Problems in Hydraulic Machinery and Systems, Brno, Czech Republic, October 2009*
10. Ruchonnet, N. and Nicolet, C. and Alligné, S. and Avellan, F., Experimental investigation of Cavitation Influence on Hydroacoustic Resonance in Pipe, *Proceedings of the 3rd Meeting IAHR Workgroup on Cavitation and Dynamic Problems in Hydraulic Machinery and Systems, Brno, Czech Republic, October 2009*
11. Nicolet, C. and Alligné, S. and Kawkabani, B. and Koutnik, J. and Simond, J.-J. and Avellan, F., Stability Study of Francis Pump-Turbine at Runaway, *Proceedings of the 3rd Meeting IAHR Workgroup on Cavitation and Dynamic Problems in Hydraulic Machinery and Systems, Brno, Czech Republic, October 2009*
12. Alligné, S. and Nicolet, C. and Allenbach, P. and Kawkabani, B. and Simond, J.J. and Avellan, F., Influence of the vortex rope location of a Francis turbine on the hydraulic system stability, *Proceedings of the 24th IAHR Symposium on Hydraulic Machinery and Systems, Foz Do Iguassu, Brazil, October 2008*
13. Nicolet, C. and Alligné, S. and Kawkabani, B. and Simond, J.-J. and Avellan, F., Unstable Operation of Francis Pump-Turbine at Runaway: Rigid and Elastic Water Column Oscillation Modes, *Proceedings of the 24th IAHR Symposium on Hydraulic Machinery and Systems, Foz Do Iguassu, Brazil, October 2008*